SCIENCE CHINA
Chemistry

•REVIEWS•

February 2023 Vol.66 No.2: 324–366
https://doi.org/10.1007/s11426-022-1408-5

Structural and functional imaging of brains

Zhichao Liu[1†], Ying Zhu[2†], Liming Zhang[1†], Weiping Jiang[3†], Yawei Liu[4†], Qiaowei Tang[2], Xiaoqing Cai[2], Jiang Li[2], Lihua Wang[2], Changlu Tao[7], Xianzhen Yin[8], Xiaowei Li[9], Shangguo Hou[10], Dawei Jiang[11], Kai Liu[5], Xin Zhou[3*], Hongjie Zhang[4,5*], Maili Liu[3*], Chunhai Fan[6*] & Yang Tian[1*]

[1]*Shanghai Key Laboratory of Green Chemistry and Chemical Processes, School of Chemistry and Molecular Engineering, East China Normal University, Shanghai 200241, China;*
[2]*Interdisciplinary Research Center, Shanghai Synchrotron Radiation Facility, Zhangjiang Laboratory, Shanghai Advanced Research Institute, Chinese Academy of Sciences, University of Chinese Academy of Sciences, Shanghai 201210, China;*
[3]*State Key Laboratory of Magnetic Resonance and Atomic and Molecular Physics, Chinese Academy of Sciences, Wuhan National Laboratory for Optoelectronics, Wuhan 430071, China;*
[4]*State Key Laboratory of Rare Earth Resource Utilization, Changchun Institute of Applied Chemistry, Chinese Academy of Sciences, Changchun 130022, China;*
[5]*Department of Chemistry, Tsinghua University, Beijing 100084, China;*
[6]*School of Chemistry and Chemical Engineering, Frontiers Science Center for Transformative Molecules, Institute of Translational Medicine, Shanghai Jiao Tong University, Shanghai 200240, China;*
[7]*Interdisciplinary Center for Brain Information, Brain Cognition and Brain Disease Institute, Shenzhen-Hong Kong Institute of Brain Science-Shenzhen Fundamental Research Institutions, Faculty of Life and Health Sciences, Shenzhen Institute of Advanced Technology, Chinese Academy of Sciences, Shenzhen 518055, China;*
[8]*Lingang Laboratory, Shanghai 201602, China;*
[9]*School of Biomedical Engineering, Shanghai Jiao Tong University, Shanghai 200240, China;*
[10]*Institute of Systems and Physical Biology, Shenzhen Bay Laboratory, Shenzhen 518055, China;*
[11]*Department of Nuclear Medicine, Union Hospital, Tongji Medical College, Huazhong University of Science and Technology, Wuhan 430022, China*

Received July 27, 2022; accepted September 28, 2022; published online December 9, 2022

Analyzing the complex structures and functions of brain is the key issue to understanding the physiological and pathological processes. Although neuronal morphology and local distribution of neurons/blood vessels in the brain have been known, the subcellular structures of cells remain challenging, especially in the live brain. In addition, the complicated brain functions involve numerous functional molecules, but the concentrations, distributions and interactions of these molecules in the brain are still poorly understood. In this review, frontier techniques available for multiscale structure imaging from organelles to the whole brain are first overviewed, including magnetic resonance imaging (MRI), computed tomography (CT), positron emission tomography (PET), serial-section electron microscopy (ssEM), light microscopy (LM) and synchrotron-based X-ray microscopy (XRM). Specially, XRM for three-dimensional (3D) imaging of large-scale brain tissue with high resolution and fast imaging speed is highlighted. Additionally, the development of elegant methods for acquisition of brain functions from electrical/chemical signals in the brain is outlined. In particular, the new electrophysiology technologies for neural recordings at the single-neuron level and in the brain are also summarized. We also focus on the construction of electrochemical probes based on dual-recognition strategy and surface/interface chemistry for determination of chemical species in the brain with high selectivity and long-term stability, as well as electrochemophysiological microarray for simultaneously recording of electrochemical and electrophysiological signals in the

†These authors contributed equally to this work.
*Corresponding authors (email: xinzhou@wipm.ac.cn; hjzhang2019@mail.tsinghua.edu.cn; ml.liu@wipm.ac.cn; fanchunhai@sjtu.edu.cn; ytian@chem.ecnu.edu.cn)

brain. Moreover, the recent development of brain MRI probes with high contrast-to-noise ratio (CNR) and sensitivity based on hyperpolarized techniques and multi-nuclear chemistry is introduced. Furthermore, multiple optical probes and instruments, especially the optophysiological Raman probes and fiber Raman photometry, for imaging and biosensing in live brain are emphasized. Finally, a brief perspective on existing challenges and further research development is provided.

brain structure, brain function, brain chemistry, chemical signal, biosensing and bioimaging

Citation: Liu Z, Zhu Y, Zhang L, Jiang W, Liu Y, Tang Q, Cai X, Li J, Wang L, Tao C, Yin X, Li X, Hou S, Jiang D, Liu K, Zhou X, Zhang H, Liu M, Fan C, Tian Y. Structural and functional imaging of brains. *Sci China Chem*, 2023, 66: 324–366, https://doi.org/10.1007/s11426-022-1408-5

CONTENTS

1 Introduction

As the most important part of the central nervous system (CNS), the brain is extremely complex in structure and function [1–3]. The brain is the central organ of the nervous system, of which about 60% is fat and the remaining 40% is a combination of water, protein, carbohydrates and ions, and neurotransmitters [4]. At a high level, the brain can be divided into the cerebrum, brainstem, and cerebellum. Among them, the cerebrum is the largest part of the brain, which consists of multiple regions, such as the cortex, thalamus, amygdala, and hippocampus [5]. The cerebrum controls

most of the activities of body, including motor coordination, temperature control, sensory, emotion, learning, and memory [6]; the cerebellum regulates movement, posture and balance [7]; and the brainstem is closely linked to vital functions such as breathing, heart rate and blood pressure [8]. Due to the extreme complexity of the brain, the understanding of how it works is still in its infancy. Current research shows that brain activity is achieved by neurons connecting and responding to nerve impulses. Neurons connect to form neural pathways, neural circuits and complex network systems. The brain uses neurons to send, transmit and receive chemical and electrical signals. The generation and transmission of these signals contribute to different brain functions [9].

The brain structure spans multiple spatial scales, forming a large-scale network, resulting in the great complexity of brain functions [10–14]. Imaging the connections and organization of neurons at various scales, can help us understand not only the makeup of specific response and behavioral circuits, but also how these circuits integrate to produce an adaptive output with coherence and prioritization, and thus can help us fully and carefully understand the internal organization mode of the brain [15]. In addition, the changes in concentration, spatial distributions, and the interactions of different biological species form complex chemical signals in the brain, and the chemical signals between neurons, neuron clusters or brain regions, contribute to various signaling pathways and neural circuits in the brain, thereby producing diverse brain functions [16–19]. These biological species include neurotransmitters, metal ions, reactive oxygen species (ROS), amino acids, and proteins [20,21]. The homeostasis of these substances plays a key role in the physiological functions of the brain. For example, neurotransmitters (*e.g.*, dopamine, norepinephrine, serotonin) are closely related to physiological processes such as learning, memory, sleep, and mood, and metal ions (*e.g.*, K^+, Na^+, Ca^{2+}, Fe^{2+}, Cu^{2+}) play an important role in maintaining cell osmotic pressure, membrane potential, redox balance and so on [22,23]. However, disorders of these substances are closely related to many brain diseases. For example, the abnormal concentration of dopamine can lead to Schizophrenia and Parkinson's disease [24], and the decrease in serotonin levels can lead to depression and anxiety [25]. In addition, abnormal accumulation of transition metal ions (*e.g.*, copper, zinc, and iron) has been observed in brain tissue with neurodegenerative diseases [26]. Therefore, the development of analytical methods for structural and functional imaging and biosensing of chemical signals in the brain is critical for understanding the physiological and pathological processes of the brain.

Over the past decades, a large number of techniques have been used for imaging brain structure. In these frontier techniques, magnetic resonance imaging (MRI) is well established and definitively the contemporary standard for structural image analysis [27,28]. Meanwhile, elegant electron microscopy (EM) and optical microscopy have also been explored for brain structural imaging, including serial-section electron microscopy (ssEM), light microscopy (LM), and synchrotron-based X-ray microscopy (XRM) [29–32]. These electron or optical microscopies provided exceptional image quality for visualization and neuroanatomical classification of brain structure.

Besides, traditional electrophysiological techniques are widely used to study brain function by recording the electrical signals of neurons [33–36]. Actually, the observation of electrical signals arises from the changes of chemical species, such as metal ions, ROS and neurotransmitters. Functional MRI (fMRI) infers neural activity indirectly from blood flow changes [37,38], but it suffers from low spatiotemporal fidelity and is difficult to be applied to behaving animals. *In vivo* electrochemical analysis based on implantable microelectrodes has emerged as powerful tool for real-time monitoring of extracellular chemical signals in the brain, due to their high temporal and spatial resolutions [39–41]. In addition, optical imaging approaches based on molecular spectroscopy, have become powerful tools for biosensing of various chemical species in the brain [42–47]. For instance, fluorescence microscopies combined with chemical probes have revolutionized neuroscience by recording intracellular molecular signals in the living brain [48–50]. Raman spectroscopy provides an effective tool for simultaneously monitoring multiple substances in the brain due to the high spectral resolution of molecular fingerprint information [51–53]. Meanwhile, a variety of frontier methods have been widely used in the biosensing of chemical signals in the brain.

In this review, we firstly overviewed many techniques for brain structure imaging, which enable multiscale imaging of brain structures, from organelles to the entire brain, at resolutions ranging from nanometers to millimeters. Particularly, the new technology of synchrotron-based X-ray microscopy for three-dimensional (3D) imaging of large-scale brain tissue with high resolution and fast imaging speed was highlighted [54–56]. Furthermore, we focused on the development of elegant methods for recording electrical signals and/or biosensing of chemical signals in the brain [57–60]. Particularly, new electrophysiology technologies like the fabrication of flexible or multichannel electrophysiology electrodes for neural recordings at the single-neuron level and in the brain were summarized [57,61,62]. In addition, we concentrated on the construction of electrochemical probes with high selectivity and long-term stability based on dual-recognition strategy and surface/interface chemistry, for determination of chemical species in the brain [59,63–73]. The building electrochemophysiological microarray for simultaneous acquisition of electrochemical and electrophysiological signals in the live brain was also high-

lighted [74,75]. Moreover, the recent development of brain MRI probes with high contrast-to-noise ratio (CNR) and sensitivity based on hyperpolarized techniques and multi-nuclear chemistry was introduced [76–79]. Multiple fluorescent probes and instruments for brain imaging and biosensing of chemical species in the live brain were outlined. At the same time, the development of optophysiological Raman probes and the building of fiber Raman photometry for simultaneous biosensing of multiple chemical species in live brain was emphasized [51–53]. The last section provided the potential future directions in large-scale fast *in vivo* brain structure imaging with high-resolution as well as large-scale dynamically recording of neuronal signaling with chemical expression across the whole brain of freely moving mice.

2 Imaging of brain structure

2.1 Magnetic resonance imaging (MRI)

Since the 1970s, MRI has become an indispensable diagnostic tool in the medical world, especially for conditions of the brain and other soft tissues [80,81]. In an external magnetic field, MRI utilizes non-ionizing radiofrequency pulses and spatial field gradients to encode certain atom nuclei, typically those of hydrogen, and records the spatial information of atom nuclei [82]. Therefore, MRI is a non-invasive and radiation-free modality that provides high spatiotemporal resolution images (Figure 1). Its contrast between different tissues mainly depends on proton density (PD) and T_1/T_2 relaxation times [83].

T_1-weighted and T_2-weighted imaging are the two basic types of MRI sequences, which enable the characterization of different tissue by T_1 and T_2 relaxation times [82]. Brain tissues with shorter T_1 relaxation time appear brighter in T_1-weighted images. For example, white matter with T_1 value of 1,084 ms at 3 T appears white and gray matter appears gray with T_1 value of 1,820 ms [84]. Conversely, tissues with longer T_2 relaxation time appear brighter in T_2-weighted images. For example, cerebrospinal fluid (CSF) shows hyperintensity in T_2-weighted images with T_2 value of about 2 s [85]. Fluid attenuated inversion recovery (FLAIR) is similar to a T_2-weighted sequence, except that CSF signal is selectively attenuated [86].

To acquire multi-contrast MRI data within a clinically acceptable timeframe, synthetic MRI was proposed which allowed simultaneous measurement of all three parameters (T_1, T_2 and proton density) [87–90]. Using those parameters, arbitrary contrast-weighted images can be generated. The first concept of synthetic MRI can be traced back to 1980s when researchers attempted to generate multiple contrast-weighted images using obtained imaging parameters [91]. After that, a wide variety of synthetic MRI methods have been proposed. Dedicated MRI sequences, including inversion recovery true fast imaging with steady-state precession (IR-TrueFISP) [92–95], multi-dynamic multi-echo (MDME) [96–98] and multi-pathway multi-echo (MPME) [99,100], have been designed to simultaneously quantify T_1, T_2, and PD within minutes. MRI

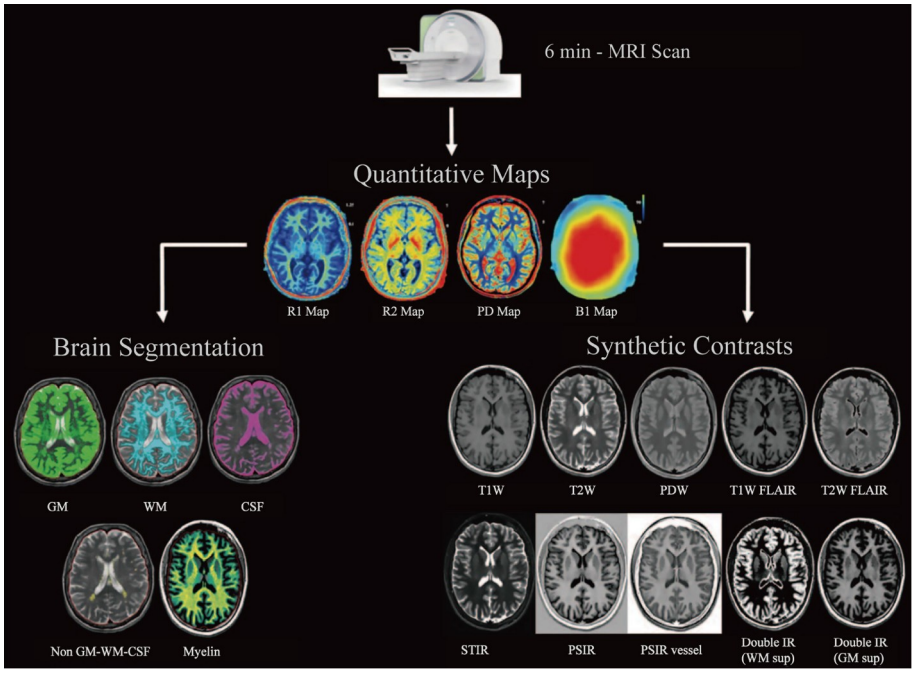

Figure 1 A representative diagram of synthetic MRI and its applications in brain segmentation and synthetic contrasts. R1 and R2 indicate the reciprocals of T_1 and T_2. IR, STIR, and PSIR represent inversion recovery, short T_1 inversion recovery, and phase-sensitive inversion recovery, respectively. Adapted with permission from Ref. [81], copyright by Wolters Kluwer Health, Inc. (2018) (color online).

signals produced by those sequences have specific functional relationships with sequence parameters such as flip angle, repetition time, and echo time. Thus, the relaxometry parameters can be calculated voxel by voxel. Magnetic resonance fingerprinting (MRF) proposed by Ma *et al*. [101] is another approach for synthetic MRI [101–103]. By varying acquisition parameters in a pseudo-random manner in MRF method, each voxel possesses a unique signal evolution, or "fingerprint". The relaxometric parameters are derived from MRF by matching the time evolution signal to numerical bloch simulations (or "dictionary"). MRF is nicely immune to undersampling artifacts due to the pseudo-random manner, and hence highly undersampled acquisition is commonly employed by which 3D volumetric MRF sequence can be scanned in a few minutes [104,105]. The diagnostic accuracy and reproducibility of synthetic MRI have been verified by comparing them with conventional MRI. Tanenbaum *et al*. [90] performed a prospective study in comparison of synthetic MRI to conventional MRI for routine neuroimaging, in which the overall diagnostic quality of MDME-based synthetic MR images was non-inferior to conventional images. Similar to MDME, MRF-based synthetic MRI demonstrated excellent repeatability and good reproducibility, especially in grey and white matter, in multiple centers at 1.5 and 3.0 T [106].

MRI volumetry is an important application based on relaxation-based MR images. Brain volume is an important determinant of brain disease progression [107]. For instance, annually loss of brain volume has been observed in patients with Alzheimer's disease (AD) and multiple sclerosis (MS), far beyond the limits of normal aging [108–111]. MRI brain volumetry is an automatic voxel-based method that allows the volumetric assessment of the whole brain, as well as other intracranial structures such as white matter, gray matter, and brainstem [112]. 3D T_1-weighted image is commonly used for brain volume estimation by registering it to the labeled atlas dataset [113], and thus establishes the spatial correspondence between T_1-weighted image and the atlas. The images modulated from the registration deformation field are then considered as the proportional scaling of brain volume [114]. There are several freely available software platforms, such as SPM [115,116], FMRIB Software Library (FSL) package [117], advanced normalization tools (ANTS) [118], and FreeSurfer [119] that can perform brain volume analysis. Besides, an online MRI brain volumetry system (volBrain) based on multi-atlas label fusion technology had also been developed for automatic volumetric brain analysis [120]. volBrain automatically segments the brain at different levels (intracranial cavity, brain macro-structures, and subcortical structures) robustly and efficiently. More recently, 3D neural networks have been proposed for efficient brain segmentation, giving good results for most brain regions [121–123]. MRI volumetry provides a unique perspective for the diagnosis of brain disorders and has become an emerging approach in recognizing pathogenesis, guiding therapy and evaluating prognosis. In the last decade, numerous studies have reported on the use of MRI volumetry to assess brain disorders, including neurodegenerative disease and many other neurological disorders. Risacher *et al*. [124] suggested that increased ratio of baseline hippocampal volume to cortical volume in AD brain was predictive of faster clinical decline. In a 6-year follow up study, Tsagkas *et al*. [125] found that spinal cord volume loss was a strong predictor of disease progression in MS. Loss of brain volume is also associated with the severity level of COVID-19 patients. A brain volumetry study revealed volume loss of brain nuclei in severe cases was more extensive than that in mild cases [126]. Combing brain MRI with lung MRI, Chen *et al*. [127] demonstrated that volume change in gray matter in COVID-19 patients was strongly related to the degree of pulmonary functional recovery.

2.2 Computed tomography (CT)

Computed tomography (CT) is a diagnostic imaging method, which is based on various types of tissues with different absorptions and transmittances when exposed to X-ray photon. Since the first commercial head-CT was designed and manufactured by Hounsfield in the early 1970s, CT techniques have gained great progress, providing high-resolution structure and anatomy information of organs, as well as achieving faster imaging speed and higher imaging safety. This makes CT imaging especially useful for the evaluation of brain tissue and the CNS. Currently, CT imaging is widely used in the research of brain structure and clinical examination of brain diseases, such as cerebral infarction, cerebral hemorrhage, cerebral ischemia, and tumor [128,129]. To better distinguish the target tissues/organs and surrounding tissues, CT contrast agents that have a high absorption of X-ray photon have been developed to enhance the contrast. The CT contrast agents in clinical use are mainly iodinated molecules, such as iobitridol, iopamidol, iohexol, iopromide, and iodixanol [130]. Computed tomography angiography (CTA) imaging, which combines the enhanced CT technique and image post-processing techniques, can be used for visualized imaging of cerebral vessels. CTA imaging has been applied for the diagnosis of vessel malformation and blood vessel diseases by observing the details of cerebral vessels [131]. Furthermore, the computed tomography perfusion (CTP) imaging method, which is functional imaging for providing hemodynamic parameter maps (HPMs), *i.e*., cerebral blood flow (CBF), cerebral blood volume (CBV),

and mean transit time (MTT), has been proposed [132]. However, CTP imaging involves multiple 3D scans, which will result in a high radiation dose. To improve the safety of CTP imaging, protocol-specific techniques and algorithm-specific techniques have been proposed to reduce the radiation dose [133,134]. With the ability of functional imaging, the CTP imaging method has been applied to many clinical applications. For example, CTP has been used to distinguish between ischemic penumbra (region with decreased CBF values and increased CBV values) and infarct core (region with severely reduced CBF and CBV values) [135].

2.3 Positron emission tomography (PET)

Positron emission tomography (PET) is based on the physical properties of radionuclides (such as ^{18}F and ^{11}C), which emit positrons when they decay [136]. When positron encounters electron, they annihilate, emitting a pair of photons with energy of 511 keV in the opposite direction. This pair of photons is captured by the high sensitive detector. After analysis and processing of different positrons, we can obtain a spatial distribution image of the radionuclide. To apply PET in the brain, radionuclide-labeled substance (such as glucose and amino acids) is first administrated into the subject, and reaches the brain through blood circulation. Each brain region has a different metabolic level. More labeled substances are consumed in the high metabolic region, which results in the accumulation of radioactive nuclei, and high signals in PET images. Therefore, PET is a high sensitive and high specificity imaging method that provides information of biomolecule metabolism, the activity of receptors and neurotransmitters. Currently, PET has been widely used in the brain and cerebral nervous system disease diagnosis, treatment evaluation and new drug development. PET using *O*-(2-[^{18}F]fluoroethyl)-*L*-tyrosine (^{18}F-FET) has been applied for response assessment in glioma patients following adjuvant temozolomide chemotherapy [137]. Two cycles of adjuvant temozolomide chemotherapy induced a reduction in [^{18}F]-FET metabolic tumor volume and maximum tumor to background ratio in 41 newly diagnosed and histomolecularly characterized glioma patients, which predicted a significantly longer progression-free survival and overall survival. And PET using ^{18}F-FET has also been shown to be a useful tool for distinguishing glioma progression and treatment-related changes [138]. Due to the small quantities of radionuclide-labeled substances that are administrated, the spatial resolution of PET is significantly lower than that of MRI and CT. Recently, PET/MRI and PET/CT methods, which combined the high sensitivity and specificity of PET and the high resolution of CT or MRI, have been developed to provide more information about the relationship between anatomical structure and physiological function. For example, Kim *et al*. [139] found that the median of the ratio of SUVmax of glioma to the SUVmean of the contralateral choroid plexus in IDH1 wild-type tumors was significantly higher than that in IDH1-mutant tumors using 11C-acetate PET/CT.

2.4 Light microscopy (LM)

2.4.1 Micro-optical sectioning tomography (MOST)

A high-resolution atlas of the brain-wide neuroanatomical architecture should fundamentally advance our understanding of the organization and function of animal nervous systems. To meet the demands of brain-wide imaging, micro-optical sectioning tomography (MOST) system was developed to provide micrometer-scale tomography of a centimeter-sized whole mouse brain [140]. MOST can be used for visualizing the brain-wide neuroanatomical structures of the mouse. The MOST system performs imaging and sectioning simultaneously (Figure 2a). The surface of the specimen was sliced in ribbons under the control of an ultra-precision positioning stage. Once glided across the rake face of the diamond knife, the ribbons were imaged immediately. Due to the special engineering design, the MOST system can ensure automation stability and high resolution during time-consuming data acquisition. Some studies have sought to develop the available preprocessing methods to improve image quality by removing the artefacts that affect the volume rendering or segmentation. For example, a set of automatic artefact removal methods was designed for image preprocessing [141], which was extensively utilized among MOST users.

Golgi staining and Nissl staining, two classical histological staining techniques, had shaped our basic understanding of the brain. These two staining techniques [140,142] were also modified to be suitable for the MOST imaging. Combining the MOST technique, the whole-brain Golgi staining allowed the 3D imaging of neurons and neuronal processes [140], and the whole-brain Nissl staining enabled labeling of the somata and blood vessels simultaneously in an entire mouse brain [142]. The crucial step of the whole-brain Nissl-staining to show the blood vessels is a longer period of cardiac perfusion with phosphate-buffered saline followed by 4% paraformaldehyde (PFA) to ensure that blood vessels are empty [143]. The hollow blood vessels could not be dyed by Nissl-staining solution, while the surrounding somata and parenchyma would be bound in different shades (Figure 2b). Therefore, the hollow blood vessels were displayed with a high grey-scale level compared with the surrounding somata and parenchyma. Based on the whole-brain Nissl staining, the vascular atlas of both arteries and veins of the whole mouse brain was reconstructed and annotated for the first time, which revealed that the vascular distributing patterns of

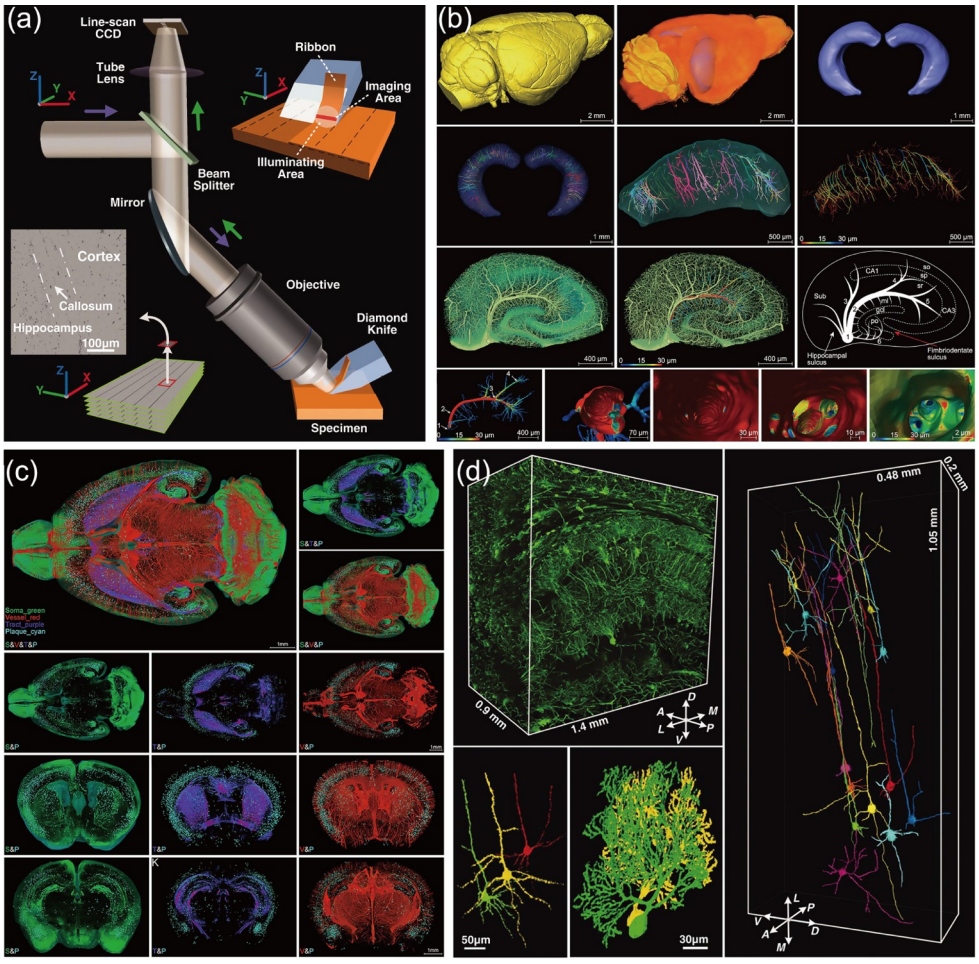

Figure 2 MOST system for brain structure imaging. (a) Schematic representation of the MOST system. Adapted with permission from Ref. [140], copyright by Nature Publishing Group (2010). (b) Segmented hippocampus for high-resolution vasculature analysis in a C57BL/6 mouse. Adapted with permission from Ref. [143], copyright by Oxford University Press (2019). (c) Simultaneous whole-brain visualization of Aβ plaques, somata, nerve tracts, and blood vessels in the 5×FAD mice. Adapted with permission from Ref. [145], copyright by EPFL Press (1982). (d) A large volumetric reconstruction of a partial hippocampus of the mouse brain. Adapted with permission from Ref. [140], copyright by Nature Publishing Group (2010) (color online).

the brain regions and even individual vessels were different from each other [144].

Actually, the Nissl-staining dataset not only presents the signals of somata and vessels (Figure 2c), but also shows multiple discernible signals of different structures such as β-amyloid plaque, nerve processes and tracts [145]. It was noteworthy that gelatin-Indian ink vessel perfusion was also employed to combine with MOST imaging to acquire the vessel network of an entire mouse brain [146]. But the cardiac perfusion of gelatin-Indian ink could only highlight the blood vessels, and other objects such as neurons could not be labeled. Besides, conventional hematoxylin and eosin (HE) staining is mainstay of histology that provide pathologic diagnostic information. However, it is difficult to stain the entire brain with hematoxylin and eosin. A modified HE staining method [147], in which delipidation and ultrasound waves were applied to enhance tissue permeability and accelerate dye diffusion, was combined with MOST for 3D volume imaging.

The detailed interpretation of the basic cerebral anatomical structures and their pathological changes are the basis of understanding brain function and diseases. Using the MOST technique and whole-brain Nissl staining, the systematic comparative study on the precise brain vasculature of wild-type and AD model mice was performed, which generated a cross-scale whole-brain 3D vascular atlas of AD mice [143]. The capability of clear visualization and quantification of the smallest capillaries offers new avenues for research on vascular distribution and regional microcirculation over the whole brain. Employing the same method, the researchers developed a customized image processing workflow to extract and reconstruct multiple structures based on differences in gray values and morphologies in the Nissl-staining dataset [145]. With this technique route, the Aβ plaques, nerve tracts, and nerve processes, somata, and blood vessels were visualized simultaneously in the whole brain of AD mice for the first time, without any specific labeling. The study provided a novel approach to present various structural in-

formations in a whole mouse brain simultaneously.

The MOST system adopted the reflected bright field imaging to generate terabyte-sized data. The processing method for the high-throughput bright-field images is more demanding than that in the fluorescence case. The bright-field images exhibited more heterogeneous gray levels and lower contrast than the fluorescent images, which makes it considerably challenging to perform 3D visualization of the structures of interest (Figure 2d). Thus, the difficulties in the 3D reconstruction of bright-field image datasets, such as HE-staining data and Nissl-staining data, are the principal technical obstacles to the more extensive application of MOST. More comprehensive applications to take full advantage of the powerful performance of the MOST system should be extended and carried out soon.

2.4.2 Light-sheet fluorescence microscopy (LSFM)

The true optical sectioning capability, low photobleaching and high imaging speed render light sheet fluorescence microscopy (LSFM) more advantageous than other microscopic approaches for acquiring brain-wide structural information at the mesoscale, including the spatial distribution of cells, their molecular features and their connectivity, which provide the structural foundation for deciphering the systems-level functional mechanisms of the brain. An LSFM consists of two optical trains, the illumination and the detection train, which are arranged perpendicular to each other. A collimated laser is transformed by the illumination train into a thin light sheet, which can be either static [148] or scanned [149], to excite fluorophores within a slice of the specimen. The emitted fluorescence is collected by the detection train whose focal volume is aligned with the light sheet. The selective illumination optical scheme empowers LSFM with the capability of optical sectioning that is necessary for 3D fluorescence imaging with much-reduced light irradiation than confocal microscopy (three to five orders of magnitude less), resulting in significantly less photobleaching and phototoxicity [150]. The detection train of LSFM is similar to a wide-field epifluorescence microscope equipped with either a charge-coupled device or scientific complementary metal-oxide-semiconductor camera, enabling the fluorescent signal within the focal volume to be recorded simultaneously with much higher recording speed (tens or hundreds of million pixels per second), compared with conventional point-scanning microscopy (typically a million pixels per second) as in confocal or two-photon microscopy. The LSFM has a moderate spatial resolution, both lateral (~1 μm) and axial (~3–5 μm), as the two objective optical geometry prevents the use of objectives with high numerical aperture [151]. Furthermore, a high axial resolution in a Gaussian beam-based light sheet microscope is achieved at the expense of a smaller field of view. However, the spatial resolution can be significantly improved by using a propagation-invariant beam such as a Bessel beam [152] or optical lattice light sheet [153] for illumination, which has enabled, for example, brain imaging at sub-cellular resolution.

The fluorescently labeled intact brain, using either an endogenous fluorescent protein, immuno-fluorescent staining, or viral labeling tools, can indeed be imaged in toto by translating the sample through the light sheet and acquiring a stack of 2D images at an optimized spatial interval for reconstructing the 3D image. However, the light absorption and scattering by the inhomogeneous refractive index inside a brain can severely degrade the light sheet, and therefore, the imaging quality is reduced, as the imaging depth increases. Therefore, the application of LSFM in brain imaging has been mainly focused on naturally transparent specimens or small organisms such as zebrafish or Drosophila, at least until the recent development of tissue clearing techniques [48,154]. Tissue clearing techniques can non-destructively transform an intact brain into an optically transparent form, enabling optical imaging of a whole-mount brain at cellular or sub-cellular resolution [155]. In recent years, many new tissue clearing methods have been developed for whole-mount brain imaging with improved tissue transparency, endogenous fluorescence preservation and tissue integrity. These methods can be categorized into three major groups based on their main chemical characteristics: hydrophobic, hydrophilic and hydrogel-based. Despite the differences in tissue processing protocols among these approaches, they were based on the same physical principle of minimizing absorption and scattering of light within the tissue by removing pigments (decolorization), lipids (delipidation) and matching the refractive index of the brain with surrounding media (refractive index matching) using carefully chosen chemical compounds. The state-of-the-art tissue-clearing methods can render the whole rodent brain, and even a human brain [156], transparent for whole-mount optical imaging.

The first demonstration of LSFM imaging of a cleared brain was achieved in 2007 by Dodt *et al*. [157], who used a custom-built LSFM with two-sided illumination to visualize the entire network of a cleared GFP-labeled mouse brain at single neuron resolution. Since then, the combination of LSFM with tissue clearing methods has become a powerful tool for directly profiling neuronal cells and mapping neuronal circuits that span the brain. For instance, the combination of LSFM with CUBIC-X, a hydrophilic tissue clearing method with tissue expansion capability, allowed the development of a 3D mouse brain atlas with single-cell resolution containing ~10^8 of an entire brain [158]. The molecular features associated with these brain cells can also be characterized since the tissue clearing methods are compatible with conventional molecular labeling techniques such as immunostaining and fluorescence *in situ* hybridization. A

good example is the whole-brain identification of neurons expressing immediate early genes (IEGs), a marker of activated neurons, using LSFM and iDISCO$^+$, an immuno-enabled hydrophobic tissue clearing method, to delineate neural circuits engaged by parenting behaviors [159]. The LSFM imaging of the whole cleared brain is particularly useful for mapping the brain-wide long-range connectivity when combined with genetic labeling techniques for selective neuron labeling. For example, the whole-mount imaging of cleared mouse brains using SHIELD, a hydrogel-based tissue clearing approach, enabled the mapping of brain-wide project patterns of parvalbumin-positive globus pallidus external neurons and the identification of their downstream target regions [160].

In addition, LSFM imaging of the brain can also be applied to acquire the local cellular connectivity when combined with the recently developed tissue expansion techniques, such as expansion microscopy (ExM) [161] and magnified analysis of proteome (MAP) [162]. These tissue expansion approaches can physically expand hydrogel-tissue hybridization by amplifying the swelling tendency of hydrogel in aqueous solutions, such as water. For example, ExM can achieve 4- to 20-fold linear expansion of the original tissue, allowing for super-resolution imaging of the tissue using a diffraction-limited fluorescent microscope, such as LSFM. Indeed, LSFM was combined with ExM for achieving nanometer scale resolution (~60 nm) to enable the tracing of long-range projections in an entire Drosophila brain [163].

Finally, larger volume LSFM imaging, such as imaging of the whole murine CNS including the brain and spinal cord, has recently been reported using an axially swept light-sheet microscopy (ASLM) to achieve larger fields-of-view [164]. However, LSFM imaging of a whole-mount primate or human brain remains challenging due to the difficulty of rendering these brains highly transparent and the lack of a microscope objective with a sufficiently long working distance [156]. In addition, larger-scale datasets of whole-mount brain images (which can involve ~100 GB to 30 TB per single mouse brain) require the development of new computational tools to extract biological meaning. Machine learning approaches may play a crucial role in this regard [165]. In the future, the mesoscale information acquired by LSFM can be fused with structural information acquired using other modalities, such as EM and MRI, to construct cross-scale views of the whole brain to finally understand complex physiological or pathological processes which is very little known at present.

2.4.3 Two-photon light-sheet microscopy (2PLSM)

Light-sheet fluorescence microscopy (LSFM) has the merits of high imaging speed and low photodamage, which make the LSFM a widely used tool in neuroscience [166]. However, the penetration depth of LSFM in thick tissues is still limited owing to the light scattering, which prevents the further application of LSFM. Two-photon excitation fluorescence microscopy (2PEM) is another widely used microscopic imaging method in neuroscience [167]. 2PEM has a large penetration depth owing to the use of near-infrared laser. The nonlinear excitation of fluorophores provides 2PEM decent axial resolution and background suppression. To combines the advantage of LSFM and 2PEM, several research groups developed two-photon light-sheet microscopy (2PLSM) [49,168–173]. 2PLSM utilizes near-infrared laser pulses to produce a nonlinear excitation light sheet and detects fluorescence with another orthogonally oriented objective. The scattering of near-infrared light in thick tissues is reduced compared with visible light, leading to better preservation of the light-sheet thickness. Moreover, the tissue autofluorescence of 2PLSM also is reduced since the rare two-photon absorption in unlabeled tissues. With these properties, 2PLSM can achieve high imaging depth, large field of view, high imaging speed, high axial resolution, and low photodamage.

Several 2PLSM methods with different optical configurations were reported. Truong *et al*. [168] developed the first two-photon scanned light-sheet microscopy. In their setup, a 940 nm femtosecond-pulsed near-infrared laser is used for two-photon excitation and an orthogonal position objective was used to collect the fluorescence. The light-sheet was created by laser beam scanning in one direction. This 2PLSM can image 400 voxels × 900 voxels × 200 voxels (x, y and z, respectively) with a volume time resolution of 45 s. Live fruit fly and zebrafish embryos were imaged to demonstrate the performance of 2PLSM. Wolf *et al*. [169] further applied this 2PSLM to whole-brain visual studies and demonstrated that the 2PSLM is suitable for 3D brain-wide functional imaging at cellular resolution. Compared with the one-photon LSFM, which uses visible light for excitation, 2PSLM can effectively avoid the visual stimulation *in situ* brain function imaging when studying a visually driven process.

To extend the field of view, Zong *et al*. [170] developed a novel two-photon three-axis digital scanned light-sheet microscope (2P3A-DSLM). In 2P3A-DSLM, a tunable acoustic gradient (TAG) index lens was used to change the laser focus on the x-axis with a frequency of ~450 kHz. By combining TAG lens and galvo scanning mirror, an ultra-thin scanned 2P light sheet can be generated within one millisecond. The size of light-sheet can be tuned by the amplitude of TAG lens and galvo scanning mirror in the x and y directions. To test its performance, the 2P3A-DSLM was used to image the time-lapse dynamics of mitochondria, chromosomal segregation during cell division, and mt-cpYFP transgenic *C. elegans*.

To increase the fluorescence signal in 2PLSM, de Vito *et al*. [173] used double-sided alternative illumination for excitation. The alternative illumination laser can maximize

the peak power of excitation in double-sided excitation 2PLSM. Owing to the quadratic dependence on the excitation light intensity of two-photon-excited fluorescence, this arrangement can result in 2-fold increase of the fluorescent signal compared to simultaneously illuminating both sides with half peak power. This signal-increased 2PLSM was used for fast whole-brain imaging of seizures in zebrafish larvae.

Takanezawa *et al*. [172] utilized lens-axicon triplet to generate long extent Bessel beam light-sheet and achieved 600–1000 μm field of view (FOV) with ~2–3-μm axial resolution when using a 10× illumination lens. The Bessel beam created with lens-axicon triplet was thinner than Gaussian beam and therefore less phototoxic is produced in this 2PLSM. Moreover, using these lens-based optics to create a non-diffracting Bessel beam suffers less energy loss, which means that more fluorescence signals can be obtained. The lens-axicon triplet-based Bessel beam 2PLSM was used for whole-body imaging of medaka juveniles with a cellular resolution. The axicon can also be positioned in the detection path to extend the depth of field (DOF) of 2PLSM as reported by Chen's lab [171]. The DOF showed 20-fold improvement with this configuration. This 2PLSM was used to image beating heart and blood cells of larval zebrafish with volume acquisition rates up to 30 Hz.

Similar to 2PEM, the main limitation of 2PSLM is the high cost of ultrafast laser for two-photon excitation and the multicolor imaging capability due to the limited spectrum although three-color TP-SLM imaging was achieved by mixed-wavelength excitation [49]. Another limitation of 2PLSM is the signal-noise ratio (SNR) due to the poor 2P excitation efficiency. This can be improved by using longer integration times [174].

To date, all the reported 2PLSM used orthogonally positioned objectives for two-photon excitation and fluorescence detection. However, the complex multi-objective configuration requires complicated sample mounting. Recently, several single objective LSFM methods were developed [175–179], which provided more flexibility and versatility for wide range of multi-scale imaging applications across the life sciences. Therefore, we can envision that the single-objective 2PLSM will permit a more versatile way in imaging brain structure and function with large imaging depth. It is also possible to extend the 2PLSM to other nonlinear optical imaging, such as second-harmonic generation (SHG) imaging and up-conversion imaging [180,181]. In recent years developed tissue-clearing methods can greatly reduce optical scattering and background fluorescence in thick sample imaging [182]. Combining 2PLSM with tissue-clearing will allow brain structure imaging with an improved high resolution and contrast [155]. Moreover, adaptive optics and deep learning offer more pathways for improving the imaging quality of 2PLSM imaging [183–185].

2.5 Serial-section electron microscopy (ssEM)

EM, as the cellular imaging technique with high-resolution ability, has always been an important tool widely used for neuroscience research for more than 70 years. Remarkably, in the 1950s, as in the earliest days of EM applicated in biology, the direct observation of synaptic junction structure between two neurons with EM, finally ended the controversy between Cajal and Golgi about the structure of the nervous system [186–188]. In the past decades, with the development of different biological EM methods, neuronal morphology and anatomy have been explored, leading to our understanding of the structural basis for neural transmission and plasticity. Recent progress in physics, biology, and other disciplines has enabled EM to achieve higher resolution, throughput, and multiple spatial scales.

2.5.1 Solving the near-atomic structure of neuronal macromolecules by cryo-electron microscopy (cryo-EM)

Proteins and macromolecular complexes are the executors of biological functions, as such solving the structure and function of bio-macromolecules is the key to cracking the mystery of life. Mainly benefiting from the new imaging detection technique and new 3D reconstruction computational techniques, cryo-EM has become one of the predominant tools to solve the near-atomic structures of biological macromolecules, especially for challenging protein complexes. Taking these technique advantages, in 2013, the structure of the transient receptor potential channel (TRPV1, the receptor for capsaicin) was solved [189], indicating that cryo-EM comes of age for structural biology. The 2017 Nobel Prize in Chemistry was awarded to Jacques Dubochet, Joachim Frank, and Richard Henderson for "developing cryo-EM for the high-resolution structure determination of biomolecules in solution". In the past years, the structures of various neuronal protein complexes, such as neurotransmitter receptors w/o antagonist or agonist bounding (Figure 3a), and the Tau filaments purified from AD brain, have been solved [190,194]. As a landmark, the inhibitory neurotransmitter receptor (GABAA receptor homopentamer) was solved at atomic resolution (1.7 Å) [195]. The solving of atomic structures of various neural protein complexes leads to molecular mechanistic insights into their function/dysfunction in the brain.

2.5.2 Revealing the in-situ structure and organization of macromolecules inside neurons with cryo-electron tomography (cryo-ET) and correlative approaches

In one aspect, the advanced high-resolution cryo-EM could determine biological macromolecules routinely at near-atomic resolution; in the other aspect, neuroscientists want to precisely map each protein complex in their native cellular contexts, which are essential for revealing the molecular

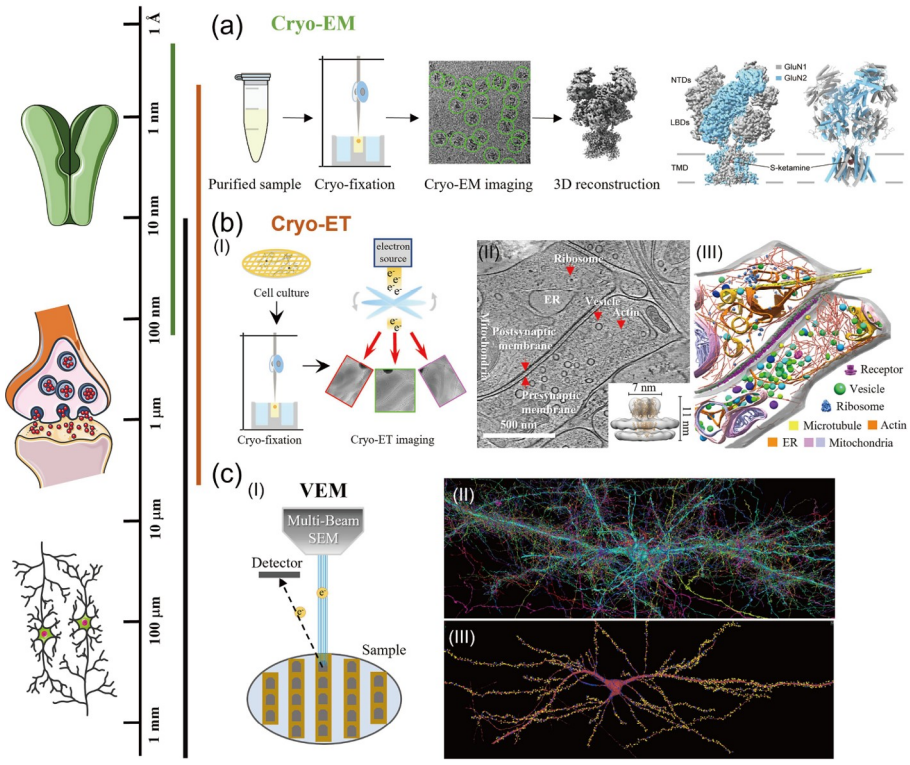

Figure 3 Brain imaging at multiple scales from individual protein complex to neural circuit using advanced electron microscopy. (a) Single particle cryo-EM solved the atomic structure of neuronal proteins at near atomic resolution. Adapted with permission from Ref. [190], copyright by Nature Publishing Group (2021). (b) Unveiling the molecular architectures of neuronal synapses in near native state with cryo-ET. (I) The principle and pipeline of studying synapses in cultured neurons with cryo-ET. (II) A tomographic slice of a hippocampal GABAergic synapse. Inset: the *in-situ* structure of GABAA receptor. (III) 3D rendering of the molecular architecture of the same synapse shown in (II). Adapted with permission from Refs. [191,192], copyright by Elsevier (2019) and Nature Publishing Group (2020). (c) Mapping the brain connectome with volume EM. (I) Schematics showing one of the advanced volume EM techniques: imaging serial sections of brain tissue prepared with automated tape-collecting ultramicrotome by multiple beam scanning electron microscopy (SEM). (II) A neuronal connectome of human cerebral cortex revealed by multibeam SEM. (III) A fully segmented neuron with all its incoming excitatory (yellow dots) and inhibitory (blue dote) synapses. Adapted with permission from Ref. [193], copyright by Nature Publishing Group (2021) (color online).

principles governing neural transmission and plasticity, and also for understanding the mechanisms of related neural diseases. Cryo-ET is an increasingly powerful tool that can dissect the molecular sociology of intact cells, including neuronal cells. In one type of major application, dissociated neurons are grown on gold cryo-EM grids. After plunge freezing, the cultured neurons on grids can be directly imaged by cryo-ET. Many discoveries have been made through this approach, including the characterization of neurotoxic protein aggregations in disease models [196,197], and the determination of the structure and organization of receptors and organelles [192,196–200]. For example, Liu *et al*. [192] have developed a novel *in-situ* cryo-ET data process strategy based on over-sampling and template-free classification, enabling to determine the *in-situ* structure of the GABAA receptor in the inhibitory synaptic postsynaptic membrane for the first time. Meanwhile, an unparalleled benefit that is unique to cryo-ET is the ability to count and map proteins of interest in their native cellular environments. As such, GABAA receptors were identified and mapped on the postsynaptic membrane for each synapse (Figure 3b), permitting further revealed mesophases organization of GABAA receptors on the inhibitory postsynaptic membranes.

While cryo-ET offered a way to visualize molecular organization in the native cellular context, optical imaging techniques benefit from their high specificity, the ability to image live cells, and high throughput. Correlative optical approaches and cryo-ET have become the tool of choice to study the structural and molecular basis of specific or dynamic cellular events [197,199,201]. Limited by sample thickness, cryo-ET is predominantly used for solving the structure of neurons with the culture neurons or isolated neuronal cellular fractions. Cryo-focused ion beam (cryo-FIB) milling is an emerging technique used to thin vitrified specimens. Cryo-FIB uses a focused ion beam to mill frozen-hydrated specimens to lamellae of ~200 nm without sample deformation [202]. This method allows thicker areas of cultured neurons to be routinely imaged [196,197]. Cryo-ET, optimized cryo-sectioning/milling techniques for tissue/cell samples, and new computational methods such as sub-tomogram averaging and deep-learning-based data process, will enable resolving the atomic details of the brain.

2.5.3 *Mapping brain connectome with volume EM*

With the launch of brain mapping initiatives in different countries, large-scale and high throughput EM technique is high demand. Volume EM, with faster imaging and data processing ability, allows for high throughput mapping of brain connectomes and other biological structures (Figure 3c). For volume EM, the brain tissue or whole brain of small animals was embedded in resin. The resin-embedded sample either can be sectioned in series sections for imaging with either transmission EM (TEM) or scanning EM (SEM), or can be directly imaged with serial block-face-SEM techniques, which is the equipment by integrated focused ion beam or diamond knife inside the SEM. This strategy enables to image and reconstruct brain samples at millimeter scale, and is capable of resolving synapse anatomy (*e.g.*, synaptic vesicle, organelles, postsynaptic density). As early as 1986, White *et al*. [203] revealed the complete set of synaptic connections of all the 302 neurons in the nervous system of Caenorhabditis elegans for the first time. Remarkably, Jeff Litchman's laboratory worked with researchers from Google company and reconstructed a 1 mm^3 human brain with volume EM [204]. However, what we can learn from such huge static image data is a big challenge. To well interpret the structure information beyond the connectome, the combining of behavior experiments or disease models is very necessary. For example, Scholl *et al*. [205] combined the *in vivo* two-photon optical imaging and volume EM to investigate the neural structure related to the special synaptic activity in the identified neurons.

2.6 Synchrotron-based X-ray microscopy (XRM)

The generation of synchrotron radiation is typically achieved by accelerating charges in large magnetic fields [206]. Compared with LM, MRI and EM, SR-XRM has inimitable superiorities: (1) Isotropic resolution, which improves the *Z* axis resolution without reducing the thickness of slices. The resolution of X-ray micro-CT in *X*, *Y* and *Z* axis can reach sub-micron, and that of nano-CT can reach 20 nm [207]. (2) High penetration, which enables rapid three-dimensional imaging of mm-thick samples with simple sample preparation without transparentizing and thin-sectioning, and preserves tissue integrity [208]. (3) No photobleaching, for which samples can be imaged for a long time. (4) Cross-scale imaging, which spans multiple scales rangeing from macro to micro [209].

2.6.1 *X-ray computed tomography (X-CT)*

X-rays are ionizing radiation produced by bombarding metal targets with accelerated electrons. Due to their short wavelength, high energy, and excellent penetration, X-rays can be used as invisible light for non-destructive imaging to obtain structural information on various samples from several meters to a few nanometers in size [210]. X-ray computed tomography (X-CT or CT), developed in the early 1970s, collects attenuated X-ray signals from different angles around the object being scanned and generates a 3D grayscale tomogram with the help of computed reconstruction algorithms [211]. As such, sources of X-ray, their energy spectrum, and mathematical reconstruction methods work together to regulate the process of image generation and dictate the final sensitivity and resolution of obtained X-CT images.

X-ray energy defines the penetrating power of the beam, thus determining their potential biological applications. High energy X-rays (energy > 5 keV), or "hard" X-rays, can pass through 300 μm tissue sections; while "soft" X-rays (energy < 1 keV) have a sub-100 μm penetration depth [211]. Two types of X-ray sources are often used, including X-ray tubes and synchrotron storage rings. X-ray tubes are more accessible and inexpensive, leading to their wide application in research labs and clinical CT scanners. They can produce X-ray beams with energy in the range of 25–150 keV, which is strong enough to penetrate human organs and tissues for clinical imaging. This is especially useful for brain structure research since the generated CT images may allow for quantitative examination of brain alterations from any direction in 3D space. Moreover, we can digitally color-code, transparentize, and highlight any specific cerebral structure for image presentation and analysis. Non-invasive and non-destructive nature of CT imaging is crucial when investigating delicate objects such as the brain, where its structural integrity is of the highest priority and whose tissue sections are difficult to obtain or manipulate. In 1988, Andreasen compared various brain imaging techniques for the assessment of cerebral structure and function and concluded that CT, among other medical imaging modalities (MRI, single photon emission computed tomography, and positron emission tomography), provided the fastest and most accessible diagnostic tool for daily clinical practice [212]. Not only can CT be used for diagnosis of physical brain damage such as stroke and hemorrhage, correlations between CT imaging-revealed cerebral structural changes and cognitive disorders (schizophrenia, epilepsy, Parkinson's disease (PD), and AD) are also established to help with clinical diagnosis (Figure 4a) [213].

While high energy X-ray beams are widely used for medical practice, their penetrating power is far too strong for cells and *ex vivo* biological samples. Synchrotron produces relatively "soft" X-rays with energy in the 0.1–1 keV range and fits better for cell and tissue-level research [54,214]. Unlike most electron or fluorophore-based microscopic imaging methods, synchrotron-based XRM can be used to image cellular and sub-cellular architectures without complex staining or risk of sample damage [215]. By fine-tuning the energy applied, heavy atoms and specific molecules in

the sample can be highlighted and their spatial distribution mapped. Collingwood and co-workers [216] successfully employed soft X-ray spectromicroscopy at 287.4 eV to visualize neuromelanin distribution in brain tissues, especially substantia nigra, for PD and related disease diagnoses. Label-free procedure and 3D mapping of XRM technique have also been used to trace iron aggregates and amyloid plaques in the brain samples of AD patients (Figure 4b, c). This has further led to longitudinal studies on the monitoring of brain subcellular structural alterations and interactive cellular events before and after intervention, to collect more evidence for drug development and treatment monitoring. Other than imaging high-atomic-number atoms such as Fe and Au, synchrotron-based X-ray techniques can also identify specific molecules in biological samples by the addition of contrast agents. Fan, Zhu and co-workers [217] successfully imaged local-polymerized diaminobenzidine (DAB) at the presence of ascorbate peroxidase (APEX2) for protein mapping. By using DAB as the contrast agent at 525 eV, a variety of molecules and sub-cellular structures with APEX2 tag can be visualized at a spatial resolution of ~30 nm (Figure 4d). Further modification of this tagging system, with the addition of neuronal promoters, may generate a series of synchrotron X-ray sensitive probes for differentiation of specific neurons and damaged brain cells producing pathogenic proteins such as Tau or amyloid.

Recently, another X-CT technique named spectral photon-counting CT (SPCCT) offers new opportunities for brain structure research [218]. By using two or more X-ray beams, SPCCT imaging collects energy characteristics of each photon and divides them into different energy bins for analysis [219]. This generates one conventional CT image and an extra material-specific mapping (K-edge mapping) at the designated energy. For example, K-edge energy of Gd (E_k =50.2 keV) mapping can be performed with X-ray beams of 40–120 keV. Similarly, iodine and Au can serve as probes for brain structural evaluation.

Taken together, X-CT imaging techniques using synchrotron-produced "soft" X-ray and tube-generated "hard" X-ray beams offered a versatile toolbox for brain structure visualization on the cellular, tissue, and whole-body levels in preclinical and clinical settings, building up a panoramic picture of the brain structural framework.

2.6.2 *X-ray phase contrast imaging (X-PCI)*

The phase information of the biological tissue is two to three orders of magnitude higher in response to X-ray than the absorption information, and the imaging using the phase contrast has higher contrast than the absorption contrast. Especially, more information can be obtained at the boundary of samples. X-PCI enables label-free imaging of biological tissue samples, significantly reducing sample preparation time.

Using X-PCI technology, Fratini *et al.* [220] carried out pioneering work in the field of brain imaging of model animals. In 2015, they performed submicron-resolution three-dimensional distribution imaging of the micro-vascular network and the neuronal system in the mouse spinal cord, which

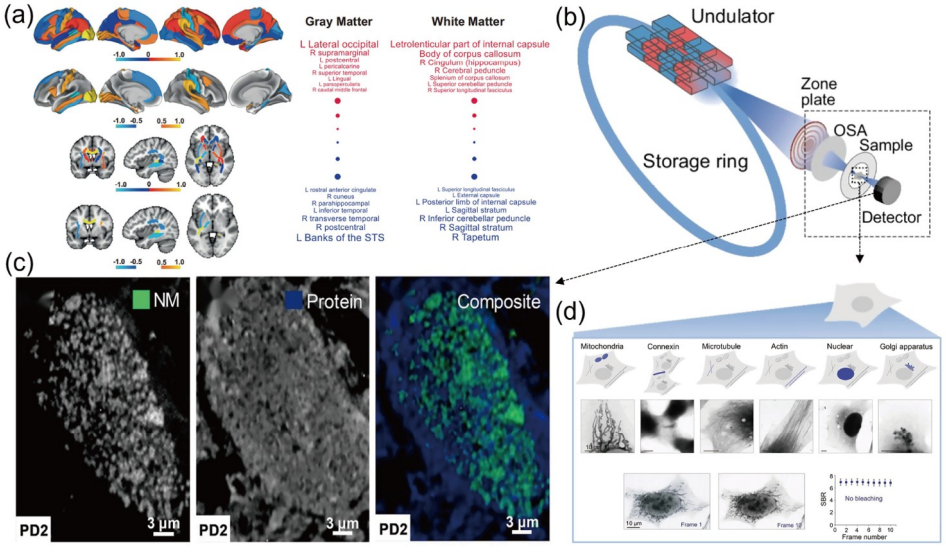

Figure 4 Synchrotron-based X-CT for brain structure imaging. (a) By using high-energy X-ray beams, clinical CT imaging establishes correlations between brain structural alterations with cognitive disorders such as schizophrenia. Adapted with permission from Ref. [213], copyright by Nature Publishing Group (2021). (b) Schematics showing imaging system of the synchrotron-based X-CT. Adapted with permission from Ref. [217], copyright by Oxford University Press (2020). (c) X-CT imaging of post-mortem brain tissues from a PD patient for spatial mapping of neuromelanin (NM), protein, and their merged image (green: NM; blue: proteins). Adapted with permission from Ref. [216], copyright by Wiley-VCH GmbH (2020). (d) A promising enzyme-tagging system that may work with synchrotron X-ray imaging for the identification of specific neurons and pathogenic cells in the brain. Scale bars: 10 μm. Adapted with permission from Ref. [217], copyright by Oxford University Press (2020) (color online).

can be distinguished without labeling and sectioning. Similarly, Hu *et al*. [221] imaged the internal microstructure of vessels and nerve fibers in rat spinal cord using X-PCI. Subsequently, Cedola *et al*. [222] used X-PCI to simultaneously image blood vessels and neuronal networks, revealing experimental autoimmune encephalomyelitis (EAE)-mediated alterations down to the capillary network and finding early vascular changes and neuronal loss in an MS model of mouse. They also performed 3D quantitative research on the neuronal network of the mouse spinal cord model and compared the obtained results with the mouse model of MS. This work paved the way for the creation of a "database" for the characterization of the neuronal network's main features for a comparative investigation of neurodegenerative diseases and therapies [223]. These results showed that the contrast ratio of the images obtained by X-PCI as a non-invasive imaging method is good, and the problem of simultaneous imaging of neurons and blood vessels can be well solved. Additionally, the neural probe was a common tool in neuroscience. Whether the implantable micro devices can maintain functional stability over time and whether the probe implantation causes changes in the surrounding tissues are issues of great concern to researchers. Böhm *et al*. [224] performed 3D imaging with an isotropic resolution of 1 μm on the implanted probe area of rat brain using X-PCI, by which the positions of the probe and the electrodes on cells and blood vessels can be distinguished, and established a research method for simultaneous three-dimensional investigation of brain tissue with implanted probe.

X-PCI also played an important role in the field of human brain imaging. In 2018, Khimchenko *et al*. [225] proposed integration of a symmetrical X-ray double-grating interferometer (XDGI) into the laboratory μCT system. The following year, they realized X-ray double-grating interferometry on Diamond Manchester Imaging Branch Line (I13-2 Diamond Light Source, Didcot, UK), conducted quantitative research on paraffin-embedded human cerebellum and made the quantitative comparison with conventional synchrotron radiation-based computed tomography. In this work, they discussed the relative merits of phase and absorption modalities for virtual histology of soft tissue, and emphasized the importance of optimization procedures for the two complementary modes and the trade-off between spatial and density resolution [226]. Furthermore, Salditt *et al*. [208] modified the optical path of P10 beamline at Deutsches Elektronen-Synchrotron (Hamburg) to image the paraffin-embedded unlabeled human cerebellum, and identified the cells in the molecular layer and granular layer using Hough transform and gray-value-based region growing algorithm. Moreover, they successfully extracted Purkinje cells from the data set, and found a strong short-range order and local clustering of granular layer cells.

In summary, synchrotron-based X-PCI is label-free, and simplifies the processing protocol of brain tissue samples, thus being an imaging method for the researches on neuronal cell body distribution with great application prospects. In the future, it can be applied to the imaging of other structures in brain such as axons or dendrites through the improvement of optical paths and optical devices.

2.6.3 X-ray nano holotomography (XNH)

XNH utilizes changes in the subtle phase shifts of the beam caused by the sample to image, in combination with holographic and tomographic reconstruction [227]. The resolution of XNH is up to tens of nanometers, and, like X-PCI, it is label-free. Moreover, the imaging speed of XNH is fast. For example, it can image drosophila whole-brain in 12 h at a resolution of 50 nm.

XNH has a good ability to image the subcellular structure of neurons. In 2018, Khimchenko *et al*. [228] used XNH to image unlabeled human cerebellar and cortical samples with an isotropic resolution of 25 nm. Compared with traditional optical tissue sections stained with hematoxylin and eosin, XNH could image subcellular structures such as the nuclear envelope and the nuclear pores at higher resolutions. Results also showed the rapid hierarchical neuroimaging and automatic rebuilding of the neuronal architecture at the level of a single cell nucleolus. In addition to high resolution of tens of nanometers, XNH allows imaging of mm-thick brain tissue slices due to the high penetration of hard X-ray. For example, a complete mouse brain only needs to be cut into ten slices, instead of 25,000 slices with optical microscopy (calculated based on the *Z* axis resolution of 0.3 μm), thus greatly saving imaging time and ensuring tissue integrity to the greatest extent. Similarly, they applied this technique to image cerebellar Purkinje cells at an isotropic resolution of 50 nm and extracted the sub-nuclear structure by semi-automatic segmentation with a success rate of 97% [229].

The deep penetration of XNH, combined with its large FOV-to-resolution ratio, makes XNH suitable for tracking the long axons of neurons. Kuan *et al*. [230] from Harvard university applied it to image the legs of adult drosophila melanogaster at an isotropic resolution of 25 nm combined with Mosaic imaging strategy. They trained a convolutional neural network to quickly segment neurons from the data set, and realized the reconstruction and tracking of a single motor axon from the drosophila muscle to the CNS. XNH is also applicable to the mouse brain. Using this technology, they reconstructed hundreds of pyramidal cells in the cortex and found more superficial cells receive stronger synaptic inhibition on their apical dendrites. Since the integrity of the tissues was preserved, they were able to perform higher resolution EM imaging of the brain tissue [230]. Collectively, XNH played an important role in the imaging of fine structures of the brain tissues with its high resolution of tens of nanometers, no labeling and fast imaging ability.

3 Electrophysiology techniques for recording ion channel activity in the brain

3.1 New electrophysiology technologies for neural recordings

Electrophysiology technologies for neural recordings have revolutionized neuroscience by recording neuronal activity *via* the local field potential (LFP) and action potentials (AP) of a single cell. However, conventional technologies for electrophysiology generally suffer from several limitations, including low spatiotemporal resolution, incompatible with biological tissues, which might cause chronic immune responses and poor stability during long-term determination. What's more, the low complexity of conventional recording technology fails to deeply reveal the complex relationship of neural circuits in behaving animals. Driven by the encouraging progress of novel neural recording technologies, recording neural activity with a great spatiotemporal resolution, low tissue damage and multi-functionality is becoming possible and attractive.

3.1.1 Electrode technologies for neural recordings with great spatiotemporal span

Electrodes are the first critical interface to the neural tissues. The recording electrode implantable into the deep neural tissues can output electrical activity signal, which can provide valuable insights into the function and organization of the nervous system. The earliest neural recording electrode was proposed by Edgar Adrian in 1928 [231]. They successfully recorded the discharge of nerve fibers using a Lippmann electrometer in which electrodes were taken as the fundamental part of the neural recording system, and the corresponding electrical activity signals in neural tissue were acquired. Since then, the research on the electrodes for nerve tissue has gradually becoming a hot field. In 1959, Hubel *et al*. [232] used tungsten electrodes to record single neurons and realized mapping visual cortex of cat. In 1981, Hamill *et al*. [233] used patch clamp to measure single ion channel current followed by nm-level and ms-level spatiotemporal resolution. Unfortunately, limited by the number of electrodes, it is still difficult to achieve the measurement of large-scale neural network communication using patch clamp technique. To date, the biggest challenge of neural recording is to measure multiple brain regions or even the whole brain to deeply understand the complex neural networks and neural activity of interest. With the development of micro-nano processing technology, the electrode fabrication technology has made revolutionary progress. The emergence of CMOS technology has made it possible to fabricate electrodes with smaller sizes and higher densities. Together with various new electrode technologies, the microelectrode arrays with high density enable the acquisition of neural data with high spatiotemporal resolution, opening a new chapter in the field of neural recording.

An important parameter for electrodes used in neural recording is low impedance at the interface to increase sensitivity and provide high signal-to-noise ratio (SNR). Therefore, inorganic metal materials like platinum black [234] and iridium oxide [235] are often used to fabricate neural electrodes. Abbott *et al*. [61] developed a nanoelectrode array for acquiring intracellular signals from thousands of connected mammalian neurons *in vitro* (Figure 5a). This array consisted of 4,096 platinum black electrodes with nanoscale roughness, in which the application of platinum black greatly reduced the impedance. Then, the entire array was integrated on a silicon chip with the flexibility to switch between voltage-clamp or current-clamp, successfully mapping over 300 excitatory and inhibitory synaptic connections from more than 1,700 neurons. A large size of metal electrode can reduce impedance, but electrode with micro/nano size provides higher spatial resolution. To solve this trade-off, the geometric area of the electrode-tissue interface is needed to be increased while the diameter of electrode is decreased. Several metal nanostructures, such as nanopillars [236] and nanoflakes [237], were developed. Lin *et al*. [58] developed an iridium oxide nanotube electrodes array for recording intracellular action potentials with sensitivity and stability (Figure 5b). Nanotube-shaped electrodes enhance the coupling between cells and electrodes, providing larger signal compared with solid-state nanoelectrodes, and is less invasive to afford continuous measurements for up to 8 days.

Moreover, the non-biological properties of metal materials cause stress on neural tissue, leading to poor biocompatibility and stability of metal electrode-tissue interface. The emergence of conductive polymers [238,239] and carbon materials [240,241] provides new possibilities for the transistor developing neural electrodes with excellent biocompatibility and stability. Conductive polymers, such as poly(3,4-ethylenedioxythiophene) (PEDOT), poly(pyrrole), and poly(aniline), were widely utilized to fabricate neural electrodes owing to their good electrical conductivity and biocompatibility. A large-scale, multi-site neural recording platform with 1,024 recording channels was developed by Chung *et al*. [242], benefitting from the flexibility and stability of conductive polymer electrodes, and can realize months-long recordings from hundreds of well-isolated units across multiple brain regions (Figure 5c). Dipalo *et al*. [243] made a graphene-decorated microelectrode platform to investigate the effect of drugs on the intracellular action potential of cardiac cells (Figure 5d). This platform consisted of 3D fuzzy graphene grown out of the plane, and the system was noninvasive without affecting spontaneous electrical activity of cells, displaying high mechanical flexibility for *in vivo* applications, high biocompatibility for long-term experiments.

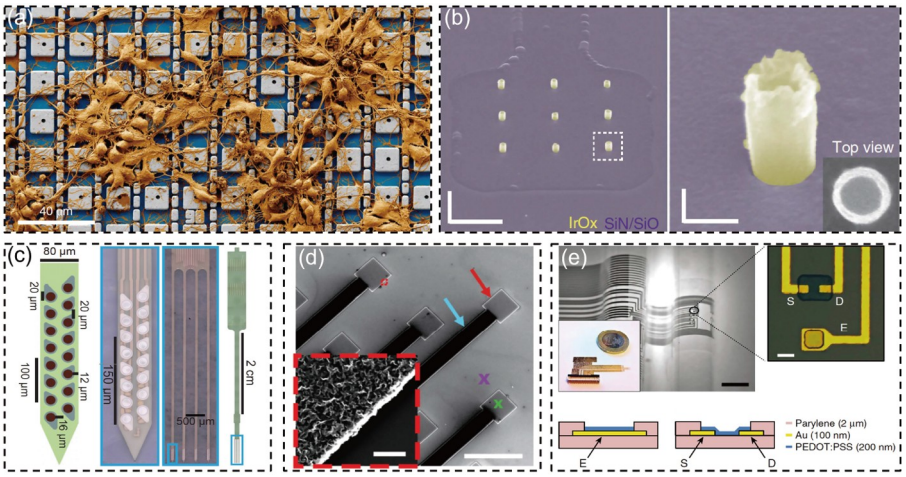

Figure 5 Electrode technologies for neural recordings with great spatiotemporal span. (a) False colored SEM image of neurons cultured on top of the platinum black electrode array. Adapted with permission from Ref. [61], copyright by Nature Publishing Group (2020). (b) SEM images of IrOx nanotube array on a square Pt pad insulated with Si_3N_4/SiO_2, in which the top view shows the hollow center of the nanotube. Scale bars: left 2 mm, right 200 nm. Adapted with permission from Ref. [58], copyright by Nature Publishing Group (2014). (c) Illustration of polymer electrode array. Left: schematic of 16-channel shank of polymer array; middle left: image of 16-channel shank; middle right: 4-shank with 250 mm edge-to-edge spacing; right: full polymer array with bonding pads at top of array. Adapted with permission from Ref. [242], copyright by Elsevier (2019). (d) SEM images of 50 μm graphene micro-electrodes. Red and Cyan arrows indicate passivated and exposed electrode area, respectively. Scale bar: 100 μm. The inset represents expanded view of the red dashed box showing of the three-dimensional fuzzy graphene geometry. Scale bar: 500 nm. Adapted with permission from Ref. [243], copyright by American Association for the Advancement of Science (2021). (e) Left: optical image of the probe conforming onto a curvilinear surface. Scale bar: 1 mm. The inset shows an image of the whole probe. Scale bar: 10 mm. Down: layouts of the surface electrode and channel, respectively. Adapted with permission from Ref. [244], copyright by Nature Publishing Group (2013) (color online).

In addition, the electrical signal generated by nerve tissues is very small in amplitude. Conventional electrodes will introduce noise while recording neural activity, leading to the difficulty to separate neural signals from noise. Transistors as neural electrodes may achieve high signal-to-noise readout, providing abundant electric information. For instance, Khodagholy *et al*. [244] prepared an organic transistor electrode for recording cortical activity *in vivo* through adopting parylene film as electrode substrate. PEDOT:poly-(4-styrenesulfonate) (PSS) was used as the transistor channel and Au served as source and drain electrodes (Figure 5e). Compared with ordinary penetrating electrodes, the device demonstrated a high SNR and flexibility, which is able to reveal brain activities with low-amplitude.

3.1.2 Flexible and transparent microprobe array

Silicon-based and noble metal-based materials such as Au and Pt have much higher elastic modulus than brain tissue. Therefore, electrodes made with these rigid materials lack long-term stability for chronic recording after being implanted into tissues because of tissue damage and inflammation [245]. Flexible electrodes can form adaptive interfaces with neural tissues due to their stretchability and structural softness, and neural electrodes made by flexible materials can maintain chronic recording [246]. In addition, low modulus of flexible electrodes causes less damage to the nerve tissue. Therefore, they are very suitable for implantation *in vivo*. There are mainly three types of flexible electrodes, filament-like probe, sheet-like probe and open mesh-like probe.

The filament-like structures facilitate insertion and exhibit good compliance with surrounding biological tissues due to their ultra-thin geometry and low bending stiffness. Musk [247] fabricated a Neurallink array composed by 96 separate soft filaments with 3,072 sensing sites. A tungsten-rhenium wire facilitates the insertion of each probe into neural tissues (Figure 6a). Coating with PEDOT:PSS and iridium oxide on each filament lowers the interfacial impedance. These filaments were suitable for chronic recording for minimizing cellular damage and glial scar formation at the electrode-brain interface. Sheet-like probes provided interfaces across multiple brain regions to record neural signals in a non-penetrating manner, referred to as electrocorticography arrays. Khodagholy *et al*. [248] developed an organic material-based, biocompatible, conformable neural electrode array named 'NeuroGrid' to record both action potentials and LFPs from cortical neurons without penetrating the brain. They used PEDOT:PSS as the interface material for sensing electrodes to decrease electrochemical impedance and provide flexibility. This device resulted in high stability of electrode to record for more than 1 week.

Transforming the planar sheet-like structure into an open 3D mesh-like structure further enhances the recording performance, enabling to record across multiple brain regions in different depth with superior flexibility and bio-

compatibility. Fu *et al*. [249] developed a macroporous flexible-mesh electronic system consisting of 16 recording or stimulating electrodes for chronic recording *in vivo* (Figure 6b). The width (20 μm) and thickness (800 nm) of the mesh elements yield a low bending stiffness, which was comparable to the stiffness of neural tissue and resulted in a low immune response. The system was highly stable for LFP recordings in mice brain for at least 8 months without probe moving. Moreover, flexible devices with optically transparent materials provided an alternative to combine various optical techniques with neural recording devices, allowing simultaneous electrical recording and optical stimulation or imaging [250]. Combination of a high temporal resolution of electrical recording and high spatial resolution of optical imaging makes unprecedented neuroscience discoveries. Metal nanowires, such as indium tin oxide (ITO) [251], conductive polymers [252] and carbon materials including carbon nanotubes and graphene, are ever utilized to prepare transparent neural recording electrodes. Qiang *et al*. [57] established a transparent 32-channel microelectrode array for simultaneous electrophysiology recording and two-photon imaging in mouse brain (Figure 6c). The microelectrodes arrays consisted of a nano-mesh bilayer of 25 nm-thick Au and an 85 nm-thick PEDOT:PSS, in which Au nanomesh served as interconnects and SU-8 layer as encapsulation. This system exhibited great compatibility and excellent optical transparency, allowing (*in vivo*) two-photon imaging of single neurons in awake mice, along with simultaneous electrical recording of visually evoked activity.

3.1.3 *Electrophysiology electrode with multi-functionality*

To reveal the connectivity of neurons in neural networks and the relationship among neural activity patterns, brain function and animal behavior is particularly significant to understand the molecular mechanism of the brain. However, simply and lonely recording the neural activity is too limited to figure out complex neural circuits. In order to solve this problem, electrophysiology electrodes combined with multiplex functionality, such as electrical stimulation, light regulation, chemical and biology regulation, have emerged and rapidly attracted extensive attention. Multifunctional electrodes have great potential to clarify the connections and dynamic communication processes in neurons and neural circuits. At present, scientists have combined electrophysiological recording electrodes with multiple functional modules, including electrical stimulation, photo stimulation, and microfluidics. Zhang *et al*. [253] reported a twining device for peripheral nerve electrostimulation and recording (Figure 6d). The device consisted of mesh Au electrodes onto a flexible shape memory substrate which can transform 2D planar structures into 3D with elastic modulus from 100 MPa to 300 kPa. The device can wrap onto peripheral nerves after exposure to physiological conditions, and stimulate the right vagus nerve with 0.4 mA current to modulate heart rates of rabbit during recording action potential of the sciatic nerve.

Optogenetic methods can mark and stimulate specific neuron subtypes to modulate neural circuits. Furthermore, optical methods are compatible with electrical recording and optical stimulation, and are less interference compared with

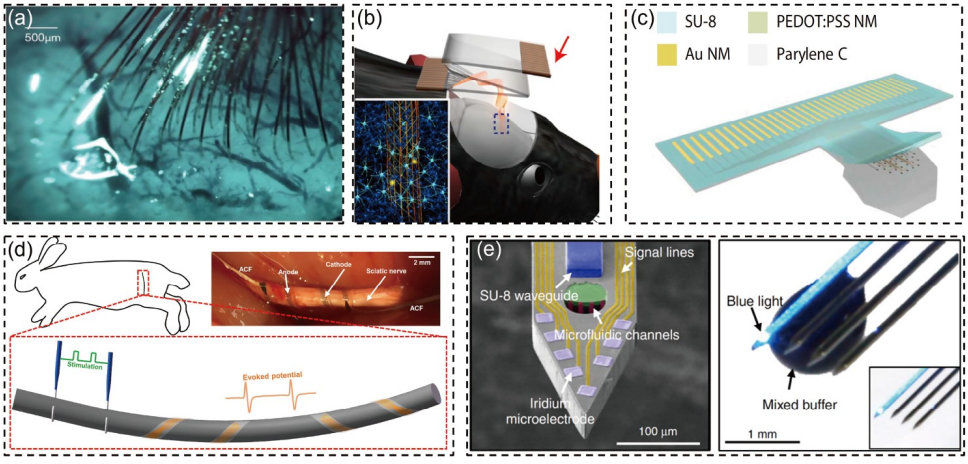

Figure 6 Flexible and transparent microprobe array. (a) An image of the filament-like 'Neurallink' array implanted to the cortical surface with minimal bleeding. Adapted with permission from Ref. [247], copyright by Elon Musk, Neuralink (1979). (b) Schematic showing a mouse implanted with mesh electronics printed to a flexible flat cable (red arrow), which is folded afterward to minimize its profile. Adapted with permission from Ref. [249], copyright by Nature Publishing Group (2016). (c) Structure of the 32-channel Au/PEDOT:PSS nanomesh transparent microelectrodes array. Adapted with permission from Ref. [57], copyright by American Association for the Advancement of Science (2018). (d) Illustration of the bipolar twining electrodes integrated on the sciatic nerve for stimulation and recording. Adapted with permission from Ref. [253], copyright by American Association for the Advancement of Science (2019). (e) Left: image of shank tip with the optical stimulation site and the outlet of the microfluidic channel. Right: a magnified image of the four-shank array showing transmitted blue light through the SU-8 waveguide and the mixed liquid delivered through microfluidic channels. Adapted with permission from Ref. [255], copyright by Nature Publishing Group (2019) (color online).

electrical stimulation while recording neural activity. Therefore, rational integration of the advantages of electrophysiology and optical method can provide a promising tool to monitor neural network activity on large scale with ultra-high spatiotemporal resolution. For example, Wu *et al*. [254] fabricated the silicon neural probes by integrating them with neuron-size microscopic light-emitting diodes (μLEDs), which were successfully used for high-resolution optogenetic studies in behaving animals. The four-shank probes, each integrated with 12 μLEDs and 32 recording sites, provided confined emission and highly localized optogenetic modulation with electrodes recording electrophysiology signal simultaneously *in vivo*. Integrated with microfluidic channels into neural probes researchers established a platform to deliver chemical and biological agents into local neurons, realizing modulation of neural activity even in deep brain regions. A soft and transparent neural implant electrode integrated with a compliant fluidic microchannel was developed by Minev *et al*. [255], which consisted of four parts including a transparent silicone substrate, stretchable gold interconnects, soft electrodes coated with a platinum-silicone composite and a small fluidic channel (50 μm by 100 μm in cross-section). The device can realize chemical neuromodulation by local drug application and simultaneously recording neuronal activity in high-resolution. Next, Shin *et al*. [256] reported a multi-functional neural probe for both recording and modulating long-range neural circuits *in vivo* (Figure 6e). The platform is integrated with an optical waveguide for optical stimulation, a microfluidic channel for drug delivery and microelectrode arrays for recording neural activity signals at the cellular level from different regions. Based on this useful electrode, they successfully modulated and confirmed the functional connectivity between the hippocampal CA3 and CA1 regions *in vivo*.

3.2 Electrophysiological recording at the single-neuron level

Cells maintain a polarized state under normal physiological conditions. The maintenance of this polarized state is closely related to the opening and closing of ion channels on the cell membrane, which generate resting potentials. When excitable cells receive a certain stimulus, they will generate nerve impulses, so-called action potentials. In 1939, Hodgkin and Huxley [257] used their homemade microelectrodes (a wire inserted into a very sharp capillary tube and filled with saline) to record the action potentials of the giant axons of the squid for the first time, which is the earliest record of intracellular electrophysiological signals. However, due to the lack of advanced technology at that time, the ionic mechanism involved has not been explored. The Voltage Patch Clamp was first invented by Kenneth Cole and Howard Curtis in 1949. The principle of this technology uses electronic feedback technology to clamp the axonal membrane potential and measure the compensation current, that is, the transmembrane current [258–260]. Subsequently, Hodgkin and Huxley successfully analyzed the components of the transmembrane ion flux during membrane excitation by using the voltage clamp technique in 1952, that is, the ascending branch of the action potential is mediated by Na^+ influx, while the subsequent descending branch is caused by K^+ efflux. At the same time, the famous Hodgkin-Huxley model was proposed [261]. Hodgkin and Huxley also won the 1963 Nobel Prize in Medicine and Physiology for this work. In 1976, German scientists Neher and Sakmann [262] poured an electrolyte solution containing acetylcholine analogs into a glass electrode, lightly pressed it on the surface of the isolated frog skeletal muscle fibers, and separated a membrane with an area of only 1–10 square microns to record a single-channel current. It was found that the background noise was significantly reduced (Figure 7a). This historical event marked the advent of Patch Clamp. The birth of patch clamp technology marks the era of electrophysiological research from the single-cell level to the single-channel level, which is an important milestone in the history of electrophysiological research [262]. The invention of patch clamp technology provided a very powerful tool for ion channel research, and it has become the “gold standard” for ion channel research. Using the patch clamp, Peier *et al*. [263] identified a TRP channel that senses cold stimuli and menthol. Noma [264] reported that application of the patch-clamp technique to CN-treated mammalian heart cells reveals specific K^+ channels which are depressed by intracellular ATP (ATPi) at levels greater than 1 mM. Nowak *et al*. [265] found the voltage dependence of the NMDA receptor-linked conductance is the consequence of the voltage dependence of the Mg^{2+} block. Although the patch clamp has provided us with information with high accuracy and high temporal resolution, this tool has limitations in practice, including invasiveness to cells, difficulty in multiplexing parallelization, and lower spatial resolution. Therefore, with the development of nanotechnology, new electrophysiological platforms based on nanotechnology are proposed to overcome the above shortcomings. The application of nanotechnology provided a powerful, non-invasive intracellular recording system such as nanoelectrodes, nanotransistors, and nanowire arrays. Lin *et al*. [58] designed a novel nanotube electrode that could prolong the recording duration of intracellular signals and the signal quality (Figure 7b–f). Zhao *et al*. [62] combined deterministic shape-controlled nanowire transfer with spatially defined semiconductor-to-metal transformation to realize scalable nanowire field-effect transistor probe arrays with controllable tip geometry and sensor size, which enabled the recording of up to 100 mV intracellular action potentials from primary neurons (Figure 7g–i).

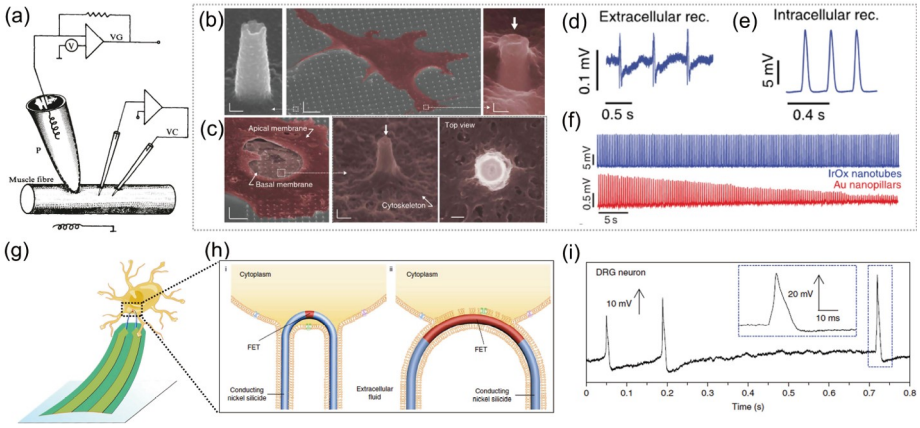

Figure 7 Electrophysiological recording at the single-neuron level. (a) Schematic circuit diagram for current recording from a patch of membrane with an extracellular pipette. Adapted with permission from Ref. [262], copyright by Nature Publishing Group (1976). (b) SEM images of a cardiomyocyte growing on top of a large IrOx nanotube array show that the cell engulfs the nanotubes. Scale bars, left of panel 100 nm, the centre of panel 5 μm, right of panel 100 nm. Adapted with permission from Ref. [58], copyright by Nature Publishing Group (2014). (c) SEM image of an unroofed cell with part of the top plasma membrane, the nucleus and the cytosol removed. Scale bars: left panel of 5 μm, the centre panel of 200 nm, right panel of 100 nm. Adapted with permission from Ref. [58], copyright by Nature Publishing Group (2014). (d) IrOx nanotube electrodes measured extracellular action potentials in HL-1 cardiomyocytes. Adapted with permission from Ref. [58], copyright by Nature Publishing Group (2014). (e) Immediately after local electroporation, IrOx nanotube achieved intracellular recording of action potentials. Adapted with permission from Ref. [58], copyright by Nature Publishing Group (2014). (f) Intracellular recording of HL-1 action potentials by IrOx nanotube and Au nanopillar electrodes for the first 60 s after electroporation. Adapted with permission from Ref. [58], copyright by Nature Publishing Group (2014). (g) Ultrasmall U-NWFET probe as a new approach for electrophysiology. Adapted with permission from Ref. [62], copyright by Nature Publishing Group (2019). (h) Schematics of two possible probe-cell interfaces. Adapted with permission from Ref. [62], copyright by Nature Publishing Group (2019). (i) Intracellular/intracellular-like recording from a DRG neuron by a ~50 nm FET channel length probe with 1 μm ROC. Inset, magnified views of selected action potentials. Adapted with permission from Ref. [62], copyright by Nature Publishing Group (2019) (color online).

Nanoelectrodes reduce cell damage due to smaller electrode tips. But smaller electrode sizes usually give rise to higher resistance, which in turn leads to reduced sensitivity. To solve this problem, recently, the developed nano field-effect transistors (nanoFETs) free from the limitation of impedance, have exhibited outstanding advantages in long-term recording and parallelization. However, this type of device is complex and expensive to manufacture, resulting in limited application in the reagent delivery, and stimulation activation functions. To date, the 3D structural design of nanoelectrode arrays has attracted extensive attention because these devices could be rationally designed to fulfill the requirements of easier implantation in nerves, good compatibility for the nervous system, and avoid immune reactions to the greatest extent [266].

3.3 *In vivo* electrophysiological recording in brain mapping

Neuronal activity generated in the brain can be obtained by measuring transmembrane currents in the extracellular medium. The main sources of extracellular electrical signals include synaptic activity, Ca^{2+} spikes and other voltage-dependent intrinsic events, as well as action potentials and spike afterpotentials [267]. Techniques for recording extracellular electrophysiological signals can be divided into non-invasive and invasive *in vivo*. Non-invasive techniques include electroencephalography (EEG), magnetoencephalography (MEG), and invasive techniques include electrocorticography (ECoG), and LFP.

As the most widely used non-invasive method for recording electrophysiological signals, EEG records rhythmic and non-rhythmic bioelectrical activities in the cerebral cortex by placing electrodes on the scalp of humans or animals. After the signal passes through a certain amplification recording system, it depicts a bioelectric signal with a certain waveform, amplitude, frequency and phase [268]. EEG technology has high temporal resolution and can monitor events that occur on the millisecond time scale. The earliest EEG recording system was invented in 1913, which consisted of a pair of sensors mounted on the head to monitor changes in electrophysiological signals throughout the brain [269,270]. Unfortunately, it was soon discovered that EEG varied substantially over the scalp [271,272], which instigated simultaneous recordings from several EEG sensors and resulted in the standardized "10–20" electrode placement system of 21 scalp electrodes (electrode separation > 6 cm) adopted half a century ago [273,274]. Although this system is still widely used by clinicians, high-density (64–256 sensors, electrode separation > 2 cm) EEG systems, which appeared three decades ago [275] quickly became a popular choice for EEG scientists and have since made their way into some clinics. Given the advances in amplifier miniaturization and wireless data transmission, EEG systems

with up to 1,000 sensors are well within reach of modern technology, which enables the acquisition of electrophysiological data with a higher SNR.

Another commonly used non-invasive electrophysiological recording technique is MEG. MEG uses superconducting quantum interference devices (SQUIDs) to monitor weak magnetic field changes outside the skull (usually in the 10–1,000 fT range) generated by the electrical activity of neurons in the brain. The temporal resolution of MEG is less than 1 ms, and the spatial resolution is about 2–3 mm [276]. The electrical activity of the brain originates from ions flowing in and out of the selective ionic membrane of neurons. EEG/MEG signals recorded on the scalp represent the underlying activation of synchronized neuronal populations that encode brain function or disease-related dysfunction [277].

The advantage of MEG over EEG is that the magnetic signal is less dependent on the conductance of the extracellular space. Part of the reason for this difference may be that the capacitive properties of extracellular media (*e.g.*, skin and scalp muscles) distort EEG signals, but not magnetoencephalogram signals [278]. MEG and EEG originate from the same type of physiological sources, described as primary currents. Major contributions to the primary currents come from postsynaptic dendritic currents in cortical pyramidal cells. The spatial sensitivity patterns to the primary currents are different for MEG and EEG, which allows MEG and EEG to provide complementary information about the same type of sources [279]. Clinically, MEG combined with EEG and structural MRI has been maturely applied to the localization of focal epilepsy, providing a powerful tool for the treatment and diagnosis of neurological diseases [280].

By contrast, ECoG is often used in clinical surgery as an invasive technique. ECoG is gradually developed based on in-depth EEG research. ECoG was first proposed in the 1950s by neurosurgeons Wilder Penfield and Herbert Jasper of the Montreal Neurological Institute [281], and was used to locate lesions in the clinical treatment of epilepsy [282]. ECoG is generally used in clinical research to monitor the electrical activity of the cerebral cortex. It uses iridium or stainless-steel electrodes under the brain dura to directly record electrical signals on the surface of the cerebral cortex, without the need to transmit signals through the skull and scalp, so its spatial resolution (<5 mm^2) is significantly better than that of EEG [267,283].

However, the low spatial resolution of EEG, MEG, and ECoG limit these techniques to only monitor electrical signals occurring in the superficial layer of the cerebral cortex (Figure 8). LFP technology is a method allowance to directly implant microelectrodes into the target brain area to monitor electrical signals with higher spatial resolution [267]. The extracellular broadband neural signals recorded by the electrodes can be processed into signals of different frequency bands by the Fourier transform. Depending on the frequency band these signals can be divided into at least two different types: the slow-varying LFPs and action potentials (AP) (typically <100 Hz for LFPs and >250 Hz for single-unit action potentials). LFP represents the collective transmembrane current of multiple neurons, and AP represents the millisecond-level response from a single neuron or single unit [284]. Furthermore, oversampling recording electrodes such as tetrodes and high-density Michigan-type silicon probes further facilitate spike separation and assignment to individual neurons, and the corresponding single unit signals generated by different neurons can be temporally resolved [285]. Although LFP has high temporal and spatial resolution, the trauma and immune response during surgery are greater than that of EEG, MEG and ECoG because of its invasiveness. As a result, LFP is currently mainly used in

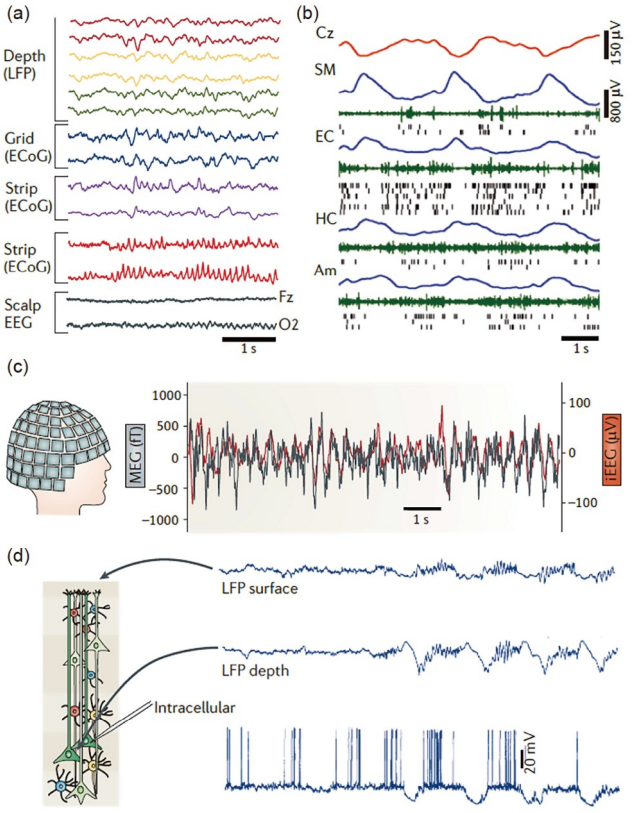

Figure 8 Extracellular traces using different recording methods are fundamentally similar. Adapted with permission from Ref. [267], copyright by Nature Publishing Group (2012). (a) Simultaneous recordings from three depth electrodes (two selected sites each) in the left amygdala and hippocampus (measuring the LFP). (b) A 6 s epoch of slow waves recorded by scalp EEG (Cz, red), and LFP (blue) recorded by depth electrodes placed in the deep layers of the supplementary motor area (SM) and entorhinal cortex (EC), hippocampus (HC) and amygdala (Am). Also shown are multiple-unit activity (green) and spikes of isolated neurons (black ticks). (c) Simultaneously recorded magnetoencephalogram (MEG; black) and anterior hippocampus depth EEG (red) from a patient with drug-resistant epilepsy. (d) Simultaneously recorded LFP traces from the superficial ("surface") and deep ("depth") layers of the motor cortex in an anesthetized cat and an intracellular trace from a layer 5 pyramidal neuron (color online).

laboratory research and is seldom applied in detection in humans.

4 Electrochemical method for determination of chemical species in the brain

4.1 Development of highly selective electrochemical probes based on dual-recognition strategy

The brain's electrical signals are generally generated by chemical species for instance ions, and neurotransmitters. Development of accurate quantification approaches for electrical signal originating from chemicals in brain is significant to analyze the molecular mechanism of brain functions. However, the living environment is complex with lots of interferences, and is distinct from detection environment for *in vitro* calibration. Therefore, the establishment of a highly selective and accurate analytical methods *in vivo* is the main scientific problem for understanding the physiological and pathological processes in the brain. To solve this problem, dual-recognition strategy-based electrochemical probes were proposed for *in vivo* measurement, in which the chemical recognition of specific ligands towards target analytes and the redox-activity of chemicals were synergistically used to enhance the selectivity of detection. Based on this strategy, a series of electrochemical probes based on dual-recognition strategy have been synthesized for *in vivo* determination of metal ions, amine acids, reactive oxygen species (ROS), and sulfides [63,66,69,71]. A Cu-free derivative of bovine erythrocyte copper-zinc superoxide dismutase (SOD-E_2Zn_2SOD) was firstly prepared for the chemical recognition of Cu^{2+} ions owing to the specific interaction between E_2Zn_2SOD and Cu^{2+}. Meanwhile, the faradic current response generated by Cu^{2+} captured by E_2Zn_2SOD was taken as the response signal. Moreover, 6-(ferrocenyl) hexanethiol (FcHT) was employed as a reference element and combined with E_2Zn_2SOD to construct a two-channel ratiometric electrochemical biosensor for the first time. This sensor showed a high sensitivity of 30.2 mA M^{-1} cm^{-2} and a low detection limit of 3 nM and was finally integrated with the carbon fiber microelectrode (CFME) to achieve selectively sensing Cu^{2+} ions in a rat brain followed by cerebral ischemia (Figure 9a–c).

Reduced Cu^{+} and oxidized Cu^{2+} are a pair of important redox active substances in the living system. The imbalance of Cu^{+} and Cu^{2+} is closely related to AD and other brain diseases. In order to investigate the roles of Cu^{+} involved in brain, Tian *et al.* [66] further designed and synthesized a series of *N*,*N*-bis(2-[2-(ethylthiol) ethyl])-based derivatives as the Cu^{+} recognition ligands (Figure 9d). After system-

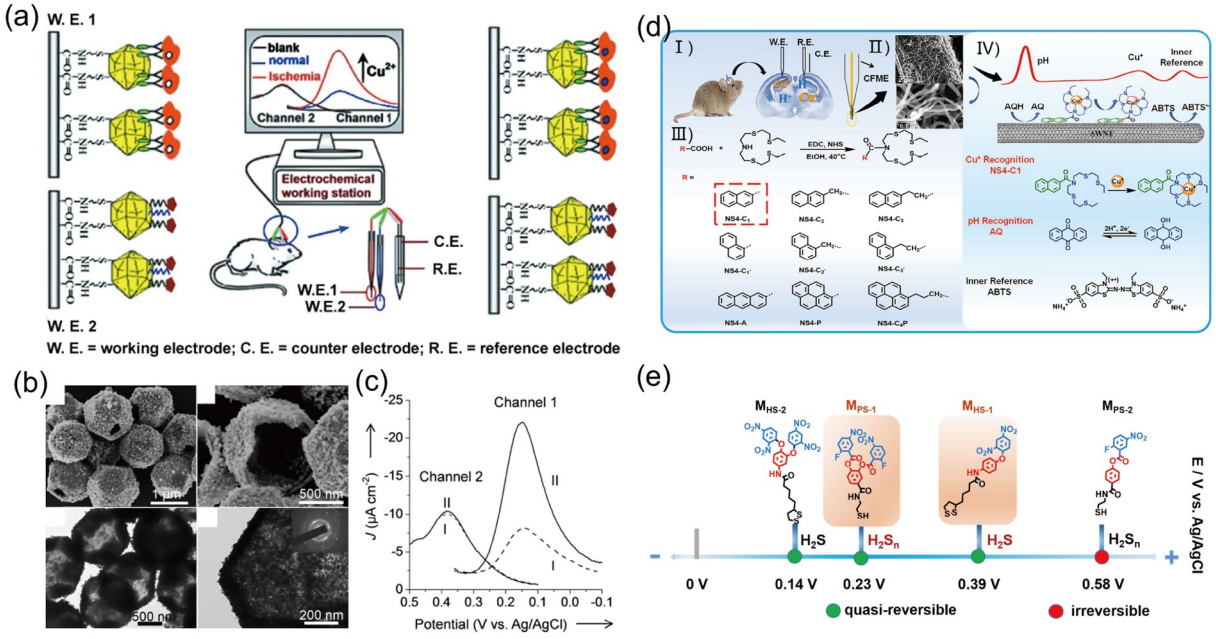

Figure 9 Development of highly selective electrochemical probes based on dual-recognition strategy. (a) The present two-channel biosensor for *in vivo* monitoring of Cu^{2+} in a rat brain. Adapted with permission from Ref. [63], copyright by Wiley-VCH GmbH (2013). (b) SEM and TEM images of the Au microcages. Adapted with permission from Ref. [63], copyright by Wiley-VCH GmbH (2013). (c) Differential pulse voltammetry (DPV) responses obtained using the two-channel ratiometric biosensor for the determination of Cu^{2+} in (I) a normal rat brain and (II) a rat brain following cerebral ischemia. Adapted with permission from Ref. [63], copyright by Wiley-VCH GmbH (2013). (d) (I) The developed ratiometric single biosensor for the simultaneous evaluation of the levels of Cu^{+} and pH in a live mouse brain. (II) SEM images of CFME/SWNT and the enlarged image of the SWNTs. (III) The general synthesis of NS4s and the corresponding molecular structures. (IV) Preparation procedures for the functionalized electrodes. Adapted with permission from Ref. [66], copyright by Wiley-VCH GmbH (2017). (e) Probes designed in the proposed sensing strategy. Adapted with permission from Ref. [64], copyright by Wiley-VCH GmbH (2019) (color online).

atically evaluating the electrochemical parameters of Cu^+ oxidation by tuning alkyl chain length, polyaromatic structure, and substitute group site of NS4, NS4-C1 was finally optimized for Cu^+ detection as it showed the most negative potential and the largest current density. Meanwhile, 9,10-anthraquinone was designed as a selective pH recognition, while 2,2′-azino-bis(3-ethylbenzthiazoline-6-sulfonic acid) was employed as an inner reference. This single biosensor with both current and potential signal outputs can simultaneously determine Cu^+ concentrations from 0.5 to 9.5 μM, as well as pH values ranging from 6.0 to 8.0. Eventually, the efficient biosensor contributed to simultaneous detection of Cu^+ and pH in the live brain with AD and found that the amount of Cu^+ was 1.8 times in rat brains with AD model than that of normal brain.

In fact, many non-redox active molecules play critical roles in brain functions. These species are difficult to be detected directly according to their faradic signal due to main two reasons: their redox potential beyond the potential window of water decomposition and their overpotential which is too large to be observed in the normal polarized window. To solve this problem, Tian *et al.* [63,66,69,71] proposed an alternative double-recognition sensing strategy through rational transferring specific chemical interaction into selective faradic current signal. A typical electroactive molecule is the polysulfide (H_2S_n). In recent years, the roles of hydrogen sulfide (H_2S) and its oxidizing forms (H_2S_n) in the physiological and pathological processes in the brain remain controversial [286–288]. Although H_2S has been demonstrated to be a signaling molecule in the past, recent studies suggest that H_2S_n is a true regulator in signal transduction [289–291]. However, the lack of an effective strategy to simultaneously determine H_2S and H_2S_n is the main barrier to understanding the physiological roles of H_2S and H_2S_n playing in the brain. Therefore, designing an efficient strategy for simultaneous detection of H_2S and H_2S_n without crosstalk and contamination is still a great challenge. Motivated by the above challenges, Tian *et al.* [64] rationally designed and synthesized the specific recognition molecules for H_2S_n and H_2S, 3,4-bis((2-fluoro-5-nitrobenzoyl) oxy)-benzoic acid (M_{PS-1}) and *N*-(4-(2,5-dinitro-phenoxy) phenyl)-5-(1,2-dithiolan-3-yl) pentanamide (M_{HS-1}) (Figure 9e). Once M_{PS-1} and M_{HS-1} have interacted with targets, the quinone derivative was generated by a specific chemical reaction, resulting in two well-separated anodic peaks. By assembling the two probes, M_{PS-1} and M_{HS-1}, on a mesoporous gold membrane decorated CFME, the microsensor exhibited high selectivity, and good resistance to biological contamination for assaying H_2S and H_2S_n in the brain. Using this electrochemical sensor, the variation of H_2S_n and H_2S in mouse brains under ischemia and AD was successfully observed. More interestingly, H_2S_n was found to exhibit a stronger ability to activate TRPA1 channel rather than H_2S. This study not only is helpful to understand the molecular mechanism of H_2S and H_2S_n, but also provides a way to design a single sensor for identifying multiple species that are closely related to physiological and pathological events in the brain.

4.2 Construction of electrochemical probes with long-term stability based on surface/interface chemistry

Stable molecular assembly at electrode surface is critical for electrochemical sensors to acquire the reliable and long-term measurements in practical brain systems. As the most popular model of molecular assembly, thiol-functionalized gold interfaces have been widely reported in electrochemical sensors [64,67,72]. However, the main shortcoming for thiol ligands is that thiol can be replaced by rich biological mercaptans such as glutathione [292,293], leading to detection distortion and unstable assembly of molecular probes on gold surface. In order to solve this problem, Tian *et al.* [68] systematically compared the analytical performance of electrochemical sensors based on Au–S, Au–Se and Au–C≡C bonds in terms of formal potential, peak current density and electron transfer rate constant, respectively (Figure 10a).

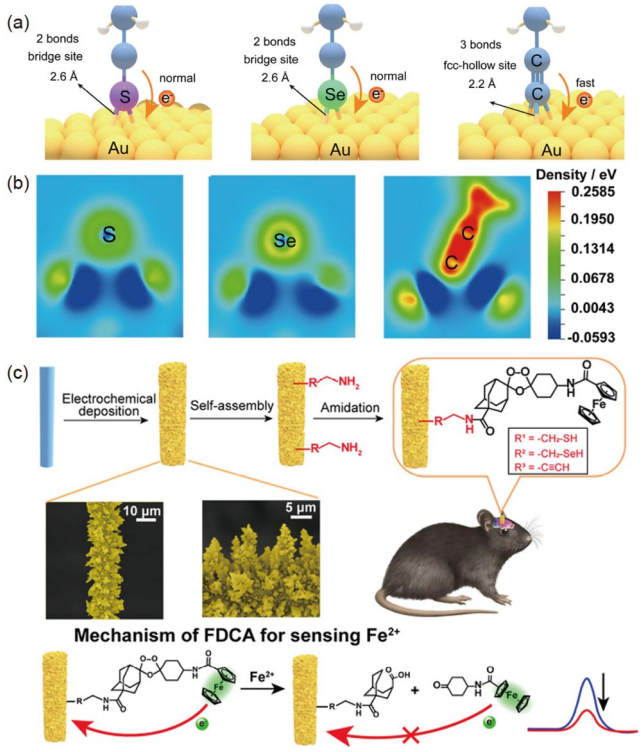

Figure 10 Electrochemical probes with long-term stability based on surface/interface chemistry. Adapted with permission from Ref. [68], copyright by Wiley-VCH GmbH (2020). (a) The synthetic route for FDCA molecule; (b) assembly of the FDCA molecules onto CFME through three strategies to form CFME/Au/AT/FDCA, CFME/Au/AS/FDCA, and CFME/Au/PA/FDCA electrodes; (c) represent SEM images of CFME/Au electrode and enlarged Au nanoparticles onto CFME and the working principle of the developed sensor for determination of Fe^{2+} (color online).

The results showed that the surface based on Au–C≡C bond had the highest bond energy, the lowest Gibbs free energy, the highest surface adsorption, and the shortest bond length, resulting in the highest stability and the best electrochemical performance (Figure 10b). Based on this discovery, the authors used Fe^{2+} as the typical model to design a ferrocenyl endoperoxide carboxylic acid (FDCA) for specific recognition of Fe^{2+}. Then, FDCA was assembled on the electrode surface by three strategies of Au–S, Au–Se and Au–C≡C bonds (Figure 10c). One part of FDCA molecules specifically reacted with Fe^{2+} through an irreversible 1,2,4-trioxolane ring-opening reaction, resulting in the loss of ferrocene group from FDCA molecule (Figure 10c). The results showed that the surface based on Au–C≡C bond indicated the best performance and the highest stability under physiological conditions. By constructing microelectrode arrays consisting of 6 channels for sensing Fe^{2+} in the brain, it has been found that extracellular Fe^{2+} entered brain neurons primarily through *N*-methyl-*D* receptor (NMDAR)-associated Ca^{2+} ion channels in hippocampus that are glutamate-mediated. In cortex and striatum, Fe^{2+} mainly enters neurons through the cAMP-regulated cAMP response element-binding protein pathway. This work provides conclusive evidence that electrochemical surfaces based on the Au–C≡C assembly strategy provide superior electrochemical performance and high stability in biological conditions and should be widely used in electrochemical biological systems and electronic devices.

4.3 Electrochemophysiological microarray for simultaneous acquisition of electrochemical and electrophysiological signals in the brain

Besides lots of coexisting interferences in complicated brain environments, many proteins are existing in the brain. Most of the proteins are electrochemical inert, and easy to be adsorbed on the electrode surface *via* nonspecific adsorption, leading to great signal loss [294,295]. As a consequence, it is still challenging to long-term monitor chemical signals in the brain. In the past few decades, sensors based on repulsion between the many hydrophilic materials and protein hydration layer have been developed to resist protein adsorption [296]. Unfortunately, electrode surfaces that are fully protected by antimicrobial materials have difficulty being modified by functional recognition molecules at the active sites. To solve these problems, Tian *et al*. [74] recently designed and developed a novel biofilm-resistant microfiber array that can real-time track extracellular Ca^{2+} changes with high reversibility and selectivity (Figure 11a). CFME modified with gold particles was alternately coated with graphene oxide microstrips (Figure 11b, c). Exposed gold particles provided active sites for modification of recognition molecules.

The developed electrodes with good anti-pollution performance were used to monitor the chemical signals of Ca^{2+} in the brain of free-moving mice (Figure 11d). The sensitivity of the electrodes remained about 92% after they were implanted in a living brain and measured continuously over 60 days. In addition, three Ca^{2+} ligands (METH, M18C6, and MBAPTA) with different recognition affinity were designed and assembled on the microelectrode (Figure 11e). Methyl has the best selectivity and reversibility for Ca^{2+}. Finally, seven microelectrodes were constructed into microfiber arrays and implanted into seven brain regions of mice respectively to monitor the reversible changes of extracellular Ca^{2+} during cerebral ischemia-reperfusion (Figure 11f). At the same time, the local electric field potential was recorded by using nickel-titanium wire electrode. The initial change time and decreasing rate of Ca^{2+} in each brain area were found to be different upon ischemia. Ca^{2+} was progressively recovered with a deceleration rate from deep to superficial brain areas after reperfusion. To further analyze the relationship between ROS and Ca^{2+} overload and neuronal death, GSH was injected into the mice at different doses before MCAO surgery. The results demonstrated that the injection of GSH can effectively inhibit the abnormal changes of Ca^{2+} after cerebral ischemia. This further confirms the direct connection between Ca^{2+} influx and cerebral hemorrhage injury. Cerebral hemorrhage is a common subtype of stroke. The microelectrode array was also used to continuously monitor extracellular concentration of Ca^{2+} in the hippocampus of mice after basal ganglia hemorrhage. The diuretics were found to quickly restore the extracellular concentration of Ca^{2+} but weakened the activity of neurons. Ca^{2+} blocker-flunarizine and reduced glutathione could both restore the Ca^{2+} concentration and promote neuronal recovery. The results suggest that the scavenger of ROS and GSH can play as a potential drug for treating cerebral hemorrhage. The work provides a method for constructing long-term stable, reversible, and selective molecular probes that can be used to study neurons in the brain by real time-tracking and accurately quantifying the concentration, distribution, and rate of change of chemicals in the brain. As indicated above, the electrochemical method is an efficient way for real-time monitoring chemical signals in the live brain [65,70,297]. Nevertheless, extra potentials or currents applied in the existing measurements may have an influence on brain microenvironments including neuron discharges [65].

To overcome the difficulty, Tian *et al*. [75] created an electrochemophysiological microarray (ECPM) to real-time measure K^+, Ca^{2+}, Na^+, and pH in rat brains by open circuit potentiometric method. Specific ion-carriers for recognition of K^+, Ca^{2+}, H^+ and Na^+ were designed and synthesized (Figure 12a), and were then modified onto tungsten microelectrode and formed ion-selective microelectrode ar-

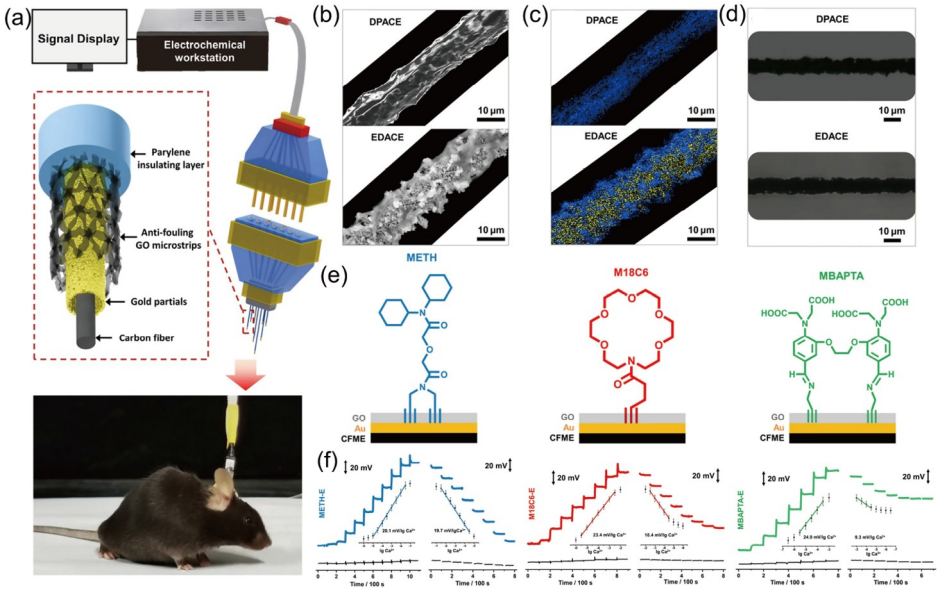

Figure 11 Electrochemophysiological microarray for simultaneous acquisition of electrochemical and electrophysiological signals in the brain. Adapted with permission from Ref. [74], copyright by Wiley-VCH GmbH (2021). (a) Illustration for multi-fiber microarray and measurements in the mouse brain; (b) SEM images of DPACE (top) and EDACE (bottom); (c) EDX analysis of the selected areas of Au (yellow) and GO (blue) on DPACE (top) and EDACE (bottom); (d) fluorescence images of DPACE and EDACE after immersed in 20 mg mL^{-1} FITC-BSA solution for 2 h; (e) molecular structures of METH (left), M18C6 (middle), and MBAPTA (right) and modification of three ligands onto electrode surfaces; (f) the potential changes obtained at METH-E (left), M18C6-E (middle), and MBAPTA-E (right) with continuously increasing concentration of Ca^{2+} and decreasing concentration of Ca^{2+} in aCSF (color online).

rays with polyvinyl chloride (PVC) (Figure 12b–e). The internal reference electrode provides built-in correction by coating PVC film on the bare tungsten microelectrode for improved accuracy. Finally, using potential measurements without additional current, the developed ECPM with high selectivity, accuracy and long-term stability was successfully applied to real-time sensing of K^+, Ca^{2+}, Na^+ and pH, and to record LFP in the brain of free-moving rats with epilepsy (Figure 12c). These observations have found that a small increase in extracellular K^+ plays a very important role in epileptic seizures. At the same time, the occurrence, development and termination of epileptic seizures are closely related to ion changes. In addition, it was found that extracellular K^+ accumulation and Ca^{2+} reduction promote membrane depolarization, leading to the loss of action potential. Furthermore, detailed dynamic information during antiepileptic drug therapy and electrical stimulation of seizures was obtained by real-time recording of the starting point, dynamic rate, changes in K^+, Na^+, Ca^{2+} and pH value.

5 Magnetic resonance imaging for brain function imaging

5.1 The development of chemical probes for brain MRI

MRI has been used to achieve multi-dimensional metabolic and functional information in addition to providing anatomical and structural information. Chemical probes are widely used in brain MRI studies and examinations to achieve high contrast-to-noise ratio (CNR) MRI images. In order to improve the CNR contrast, researchers have proposed different chemical probes including: (1) high relativity probes such as gadolinium-based contrast agents [298–300], iron-oxide nanoparticles [301,302] and gadolinium-free contrast agents [303,304]; (2) high target sensitive probes like biomarker-targeted probes [305,306], local physiological parameters or metabolites-response probes [307–310]; (3) high SNR probes involving ^{13}C-labeled cell substrates and ^{129}Xe-loaded probes based on the signal enhancement using dynamic nuclear polarization (DNP) and spin exchange optical pumping (SEOP) techniques respectively [311–315], ^{19}F-based probes with low *in vivo* background signal due to the low natural abundance of the element in human and animals [316,317], endogenous and exogenous chemical exchange saturation transfer (CEST) agents with more than 1,000-fold detection sensitivity improvement through indirect detection of water signal [318,319]. The further development of probes needs to improve the specificity and biocompatibility or safety, so as to promote the innovative development of molecular MRI in the brain.

5.2 MRI for molecular metabolic imaging and cellular activity imaging in the brain

5.2.1 Magnetic resonance spectroscopy (MRS)/spectroscopy imaging (MRSI)

Magnetic resonance spectroscopy (MRS) is widely used for

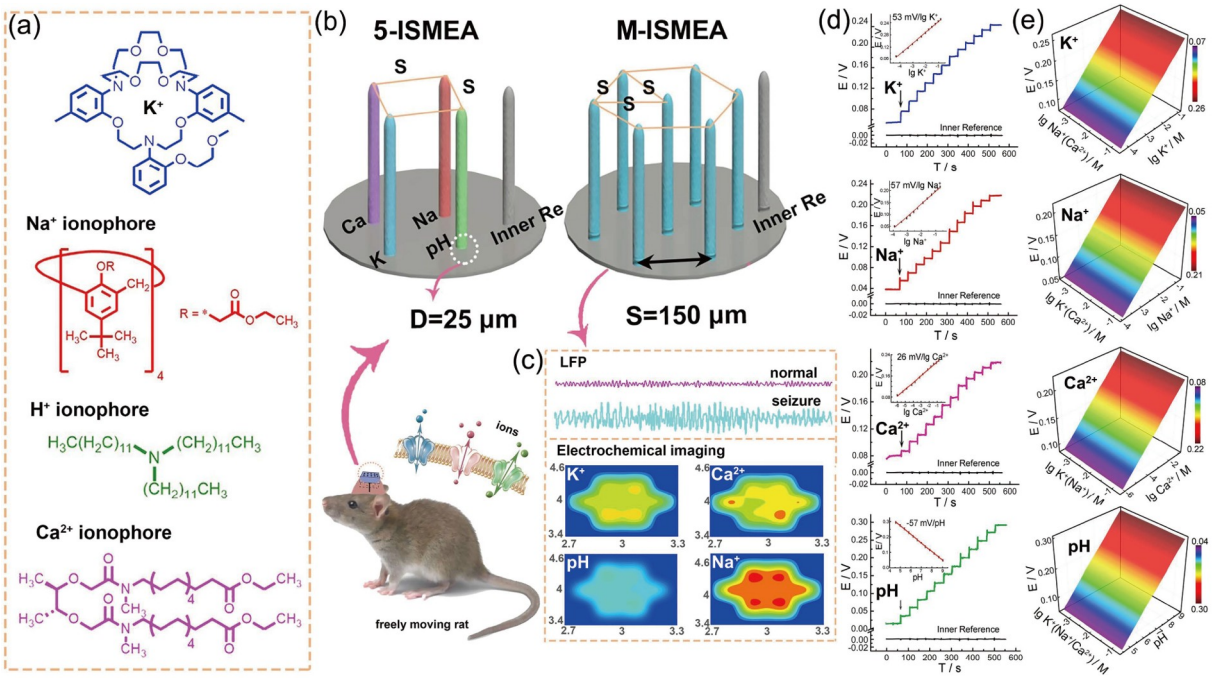

Figure 12 Electrochemophysiological microarray for simultaneous acquisition of electrochemical and electrophysiological signals in the brain. Adapted with permission from Ref. [75], copyright by Wiley-VCH GmbH (2020). (a) Specific recognition molecules for K^+, Na^+, pH, and Ca^{2+}; (b) schematic structures of 5-channel ion-selective microelectrode arrays (5-ISMEA) and 8-channel M-ISMEA (K-ISMEA, Ca-ISMEA, Na-ISMEA or H-ISMEA); (c) LFP signals that were recorded in a live rat brain upon seizure, and the developed ECPM for real-time mapping and simultaneous quantification of multi-ions in the brain of freely moving rats; (d) potential responses of 5-ISMEA toward KCl, NaCl, $CaCl_2$, and HCl in 0.1 M Tris-buffer; (e) 3D surface plots of potential separation (ΔE_{ISE}) or K^+, Na^+, Ca^{2+}, pH responses of K-ISME, Na-ISME, Ca-ISME, and H-ISME as a function of one kind of ion and the other three ions (color online).

non-invasive measurement of the concentration levels of different metabolites in the brain. In addition to the determination of common metabolites (*e.g.*, *N*-acetyl-aspartate (NAA), choline (Cho), creatine (Cr), glutamate (Glu), glutamine (Gln), gamma-amino-butyricacid (GABA)) (Figure 13a), ^{1}H MRS has been applied to detect 2-hydroxyglutarate (2-HG) and cysthathine recently [322–325]. 2-HG and cystathine are biomarkers of glioma isocitrate dehydrognase (IDH) mutation and 1p/19q codeletion respectively, so their quantitative detection is helpful for the diagnosis and treatment of glioma, opening up the possibility for accurate presurgical molecular classification of tumor. Endogenous phosphorous metabolites including adenosine-triphosphate (ATP), freep phosphate (Pi), phosphocreatine (PCr) and phophorylcholine (PC) can be detected by ^{31}P MRS, which provides important information for brain tissue energy metabolism [326]. Several studies of energy metabolism in brain diseases such as AD, PD and brain tumors using ^{31}P MRS have been reported [327–329]. MRS is known to determine metabolite concentration, while the study of metabolic processes depends on the infused substrate. With the signal enhancement benefiting from DNP technique, ^{13}C-labeled cell substrates and their downstream products could be detected by ^{13}C MRS [330]. The longitudinal relaxation time T_1 and the polarization level of different substrates (*e.g.*, [1-^{13}C]pyruvate, [1-^{13}C]lactate, [1-^{13}C]alanine, [1-^{13}C]α-ketoglutarate, [1-^{13}C]glutamine, [1-^{13}C]glutamate) have been explored, in which [1-^{13}C]pyruvate is the most widely substrate with polarization level larger than 60% and 40 s longitudinal relaxation time at 9.4 T [331]. Pyruvate is metabolized to lactate, alanine, and bicarbonate in a matter of seconds, and each of these metabolites could be quantitatively measured because of the chemical shift differences (Figure 13b). Miloushev *et al.* [332] obtained the first dynamically human brain hyperpolarized ^{13}C metabolic spectra and metabolite maps in brain tumor patients, and suggested that hyperpolarized ^{13}C pyruvate-lactate conversion is a metabolic biomarker for assessing tumor response. The rate of [1-^{13}C] pyruvate conversion to lactate and bicarbonate has been further explored [333–335]. Finding and manufacturing appropriate ^{13}C-labeled substrates will further promote its application in brain. Moreover, the low background signal in brain, high gyromagnetic ratio and 100% natural abundance of ^{19}F make it suitable for brain MRS/MRI. Fluorine-based contrast agent can be engineered as nanoemulsions or nanoparticles to label cells *in vivo* [336,337]. ^{19}F MRS has also been used to measure the concentration and distribution of fluorinated pharmaceuticals (*e.g.*, fluvoxamine and fluoxetine), and determine the pharmacokinetics of novel fluorine-based drugs

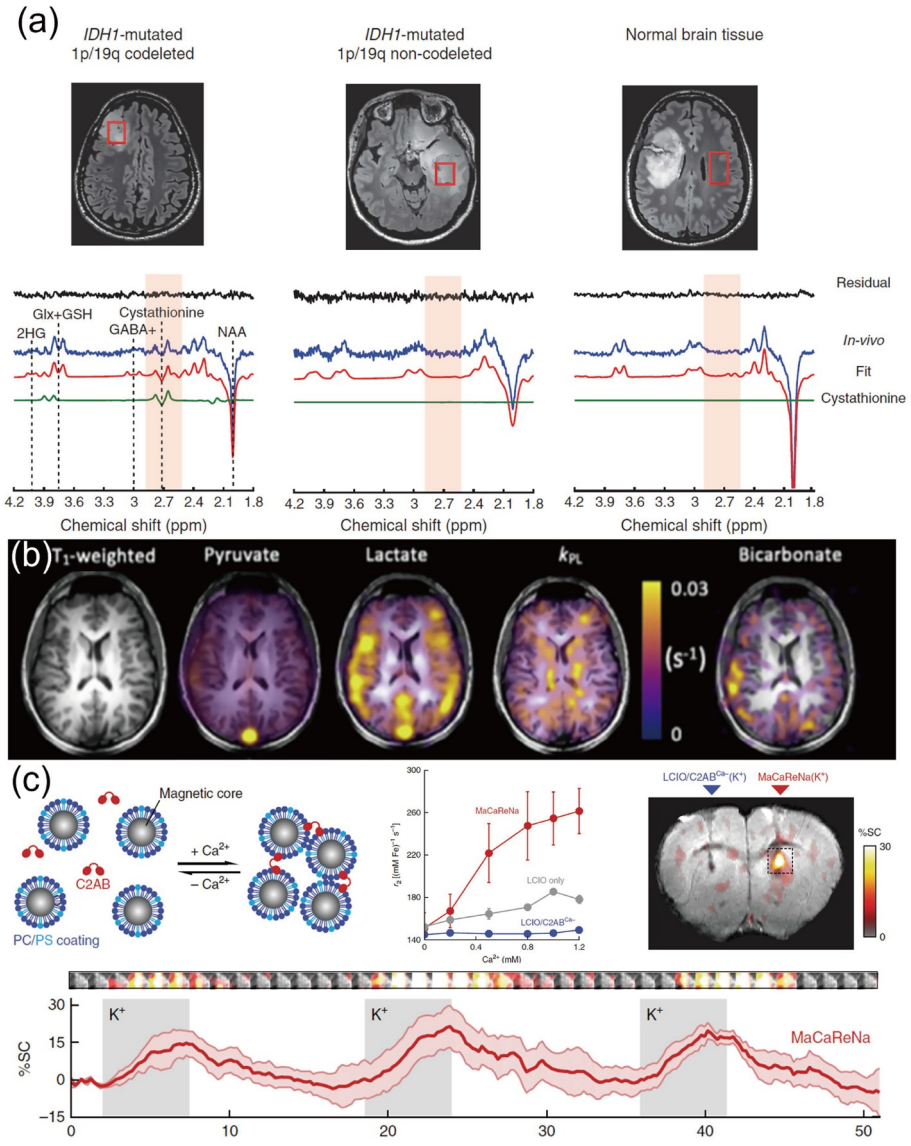

Figure 13 Metabolites detection using MRS/MRI. (a) Localized ^{1}H MRS of an IDH1-mutated 1p/19q codeleted glioma, an IDH1-mutated non-codeleted glioma and normal brain tissue. The 2-HG signal (~4.0 ppm) is visible in IDH1-mutated glioma, and the cystathionine (~2.7 ppm) is only visible in IDH1-mutated 1p/19q codeleted glioma. Adapted with permission from Ref. [320], copyright by Oxford University Press (2019). (b) ^{13}C imaging demonstrates metabolite distribution in the healthy human brain following injection of hyperpolarized [1-^{13}C] pyruvate. Adapted with permission from Ref. [311], copyright by Elsevier (1969). (c) The design schematic and characterization of magnetic Ca^{2+} responsive nanoparticles, which shows dynamic response to multiple cycles of K^{+} stimulation. Adapted with permission from Ref. [321], copyright by Nature Publishing Group (2018) (color online).

(*e.g.*, BAY1436032 and teriflunomide) in brain tissue [338–340].

5.2.2 Blood oxygenation level dependent (BOLD)-based functional MRI (fMRI)

Since Kwong *et al*. [341] and Ogawa *et al*. [342] imaged the hemodynamic changes associated with brain nerve activity using blood-oxygenation-level-dependent (BOLD) MRI technique. BOLD functional MRI (fMRI) has been proposed and widely used in cognitive science and neuroscience [343]. BOLD fMRI is based on the local magnetic field property change caused by the mismatch of local oxygen consumption and cerebral blood flow affected by nerve activity. The designed probes should be able to improve the relaxation contrast or have a specific targeting ability. Transverse relaxation (T_2) contrast agents (*e.g.*, superparamagnetic iron oxide (SPIO) nanoparticle) have been used to improve detection sensitivity and spatial specificity [301,344,345]. The ultrasmall SPIO nanoparticle ferumoxytol, which was approved for use as an intravenous iron replacement therapy in anemic patients, has been shown to enhance task-based fMRI signals (cerebral blood volume fMRI) by a factor of 2.5 at 3 T compared with the BOLD effect [301]. Specific designed probes targeting neurotransmitters (*e.g.*, dopamine, glutamate, acetylcholine) or ions (*e.g.*, Ca^{2+}, Zn^{2+}) particles have been reported [346–350]. Taking a Ca^{2+}-sensitive probe as an

example, Angelovski *et al*. [349] proposed a gadolinium-based Ca^{2+}-sensitive T_1 probe for early detection of cerebral ischemia. Okada *et al*. [321] designed a lipid-coated magnetic nanoparticle and synaptotagmin protein sensor for extracellular Ca^{2+} detection, which showed a dynamic response to multiple cycles of K^+ stimulation (Figure 13c). They recently proposed a genetic probe named NOSTIC, which will produce nitric oxide in response to Ca^{2+} associated with nerve activity when expressed in neurons, thereby generating a visible BOLD fMRI signal [351].

5.2.3 Other MRI methods

Chemical probes have also been fabricated for other MRI methods. Xu *et al*. [352] recently reported an engineered adeno-associated virus probe that contains aquaporin reporter gene and fluorescent, and the astrocytes have been detected by both fluorescent imaging and diffusion-weighted MRI. CEST imaging brought more than 3 orders of magnitude detection sensitivity enhancement, and a series of endogenous and exogenous CEST agents has been reported [353–356]. Some CEST agents (*e.g*., glucose, iopamidol) are known molecules that are currently used in human clinical trials. In addition, the ^{129}Xe signal can be enhanced more than 10,000-fold than that of thermal polarization by SEOP techniques, thereby enabling ^{129}Xe MRI/MRS in brain [76,77,357]. In order to improve the specificity, researchers have designed a series of probes targeting different substances (*e.g*., biothiol) based on cage-like probe molecules such as cryptophane, cucurbit [6]uril, pillar[5]arene, gas vesicle, and metal-organic frameworks [358–364]. And the further application of ^{129}Xe in brain needs to improve the specificity and water solubility of probe.

6 The development of multiple chemical fluorescent and Raman methods for brain imaging

6.1 Fluorescent probes for brain imaging

Fluorescence imaging has fascinated increasing regard in the field of brain imaging due to its advantages of non-radiotoxicity, non-invasiveness, high spatiotemporal resolution, rapid detection and high sensitivity [365–369]. With the mastery of the synthesis of fluorescent reagents and the vigorous expansion of optical technologies, fluorescence imaging technology has developed dramatically, realizing the identification and detection of brain regions [370–374]. The imaging resolution can reach single nanometer level, and the imaging depth in several millimeters can even be achieved. Thus, fluorescence brain imaging can be realized without craniotomy, bone window and craniotomy procedures, which greatly reduces irreversible damage to the brain and broadens the scope of brain imaging. The fluorescent probes used for brain imaging mainly include organic fluorescent probe, inorganic quantum dot fluorescent probe, fluorescent protein probes and lanthanide-based fluorescent probes, and these probes are summarized and described in detail.

6.1.1 Organic fluorescent probe

Organic small molecules possess clear structures that can be finely designed and adjusted based on physical and optical properties [375]. Moreover, their high biocompatibility and rapid excretion ability make them to be widely applied for biological imaging. Zhang *et al*. [376] developed a small molecule LZ-1105 for *in vivo* NIR-II fluorescence imaging. The LZ-1105 dye consisting of four sulfonic groups displayed the highest fluorescence intensity, achieving a high imaging penetration depth of 1.31 mm and a better SNR of ~5.0 during brain imaging. Following intravenous injection of LZ-1105 dye, the vasculature in the brain through the intact scalp and skull was observed by NIR-II fluorescence imaging. Moreover, the LZ-1105 dye displayed good *in vivo* stability, conferring long-term cerebrovascular imaging within 4 h. Importantly, the LZ-1105 dye could also be used for dynamical tracking of the temporal opening and restoration of the blood-brain-barrier (BBB) through fluorescence imaging (Figure 14a). They also designed another small molecule organic dye, FD-1080, through four linear synthetic steps. By introducing sulphonic and cyclohexene groups, FD-1080 dye possessed good water solubility and stability. This dye could emit NIR-II emission of 1,080 nm under 1,064 nm excitation. When it was further integrated with fetal bovine serum, the obtained fluorescent nanoparticles displayed a high quantum yield (QY) of 5.94%, which enabled non-invasive *in vivo* brain imaging. The blood vessel of mouse brain could be imaged obviously through the scalp and skull by using this FD-1080 dye. Qian *et al*. [377] developed a novel fluorophore CAQ to selectively monitor Aβ aggregates in mouse brain. CAQ contained a curcumin scaffold, a 4-(dimethylamino) donor group, and a quinolone-functional fluorophore. The donor group was introduced to alter the fluorescent signal upon binding to the targeted proteins, and a quinolone functional group was added to improve the penetration of BBB and biocompatibility. Owing to the specific intramolecular rotation effects in CAQ, CAQ could be used for tracking Aβ aggregates *in vivo* through fluorescence imaging, providing a toolbox for studying and understanding the pathological processes of AD.

Despite the versatility of small organic molecules in brain imaging, it is undeniable that smallest organic molecules have relatively low QYs. Particularly, their inherent hydrophobicity always leads to a diminished or annihilated fluorescence when they aggregate together, termed aggregation-caused quenching effect (ACQ). In contrast, another class of organic molecules barely fluoresces when

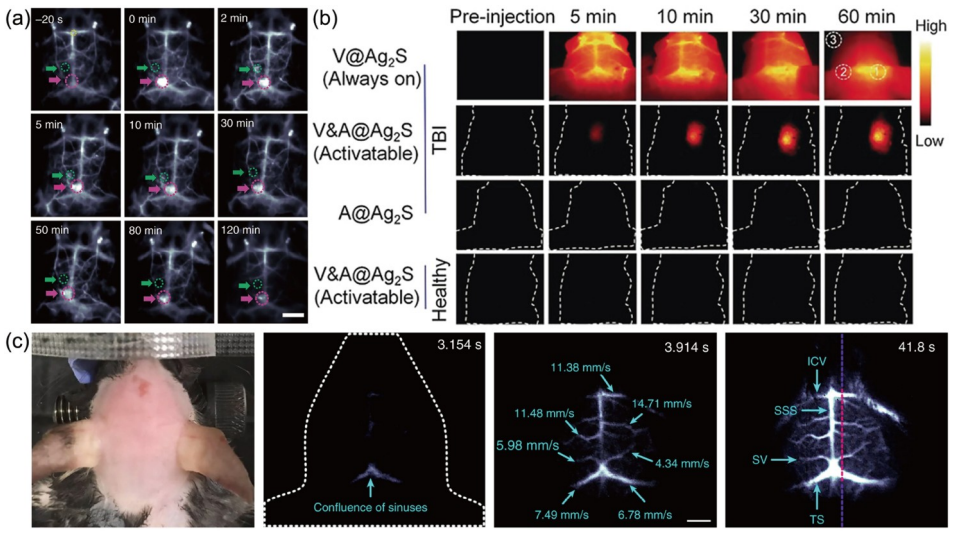

Figure 14 The *in vivo* brain imaging by using different fluorescent probes. (a) LZ-1105 dye for dynamical tracking of the temporal opening and restoration of the BBB. Adapted with permission from Ref. [376], copyright by Nature Publishing Group (2020). (b) V&A@Ag_2S nanoprobes for activatable *in vivo* fluorescence imaging of functional brain regions. Adapted with permission from Ref. [61], copyright by Wiley-VCH GmbH (2020). (c) Lanthanide-based nanocrystals for tracking the arterial blood flow in the mouse brain (color online).

monodispersed in solution, but fluoresce brightly when they aggregate. This anomalous phenomenon is called aggregation-induced emission (AIE). AIE properties can be used to design organic fluorescent probes with both bright luminescence and high QYs, enabling high-contrast and high-resolution brain imaging. Based on the molecular design concept of AIE, Tang *et al*. [378] modified the photothermal contrast agent 2TT-*m*C6B through the combining processes of backbone distortion and rotor twisting to weaken the intermolecular interaction. The resulted 2TT-*oc*6b showed typical AIE properties, displaying high fluorescence in aggregates. 2TT-*oc*6b emitted at 1,030 nm with a high quantum yield of 11%, showing great potential for deep brain imaging. Furthermore, in order to target inflammation tissue in the brain and penetrate the BBB, neutrophils were applied to carry 2TT-*oc*6b. The achieved AIE@NE nanoparticles possessed a high SNR fluorescence imaging of 30.6 through intact scalp and skull, enabling non-invasive identification of the inflammatory sites in mouse brain.

Qu *et al*. [379] chose the acrylonitrile with aggregation-induced luminescence properties as the skeleton to produce AIE-active fluorescent probe. Appropriate conjugated donor and acceptor functional groups were judiciously designed to adjust the fluorescence performance. In addition, pluronic F-127 was further applied to encapsulate AIE-active fluorescent dye and formed water-dispersible nanoparticles. Synthetic AIETP NPs displayed the highest fluorescence emission under the excitation of 1,040 nm, enabling *in vivo* dual-photo imaging with a penetration depth of 800 μm on craniotomy-based mouse brains. By using AIETP NPs, a high SNR values of >5 and a very high spatial resolution of 1.92 μm were finally achieved. Moreover, 2D and 3D images of the cerebral vasculature were also realized.

Semiconducting polymers possess delocalized π-conjugated backbones and modifiable side chains, which endow them with excellent photophysical properties. Their large extinction coefficients, outstanding photostability, excellent water dispersibility, and biocompatibility make them ideal for bioimaging fluorophores. The absorption and emission of semiconducting polymers are determined by the band gap, so the fluorescence properties can be adjusted by changing the molecular structure of the polymer. Wu *et al*. [380] developed two sets of semiconducting polymers for quantitative brain imaging. Benzdithiophene (BDT) was used as donors and triazole[4,5-*g*]-quinoxaline (TQ) as acceptors. Furthermore, a fluorination strategy was employed to reduce radiative relaxations and enhance the NIR-II fluorescence. As a result, high fluorescence quantum yields ranging from ~6.6% to ~9.5% were finally achieved, displaying great potential for NIR-II fluorescence imaging. After that, the semiconducting polymer further interacted with PS-PEG-COOH to form colloidally stabilized semiconducting polymers dots (Pdots). By injecting the brightest Pdots through the tail vein, the whole body of the mouse was imaged under the excitation of 808 nm laser. The though-scalp and skull imaging of mouse brain also showed that Pdots displayed a long blood circulation time, conferring high-resolution brain imaging over 2 h. This team also fabricated nine Pdots through a molecular engineering strategy for NIR-II fluorescence brain imaging. Phenothiazine chromophores with AIE characteristics were chosen as the donor. Benzothiazoles and their derivatives with different structures were applied as acceptors in Pdots. By establishing the relationships between the structure of Pdots and their fluorescence performances,

the dual fluorescence enhancement mechanism was validated. As a result, NIR-II Pdots with high QYs of ~1.7% in aqueous solution were developed. By intravenous injection of Pdots, fluorescence imaging of the mouse brain was achieved by excitation of 808 nm with a low power density of 70 mW cm^{-2}. A 1,319 nm long-pass filter was further applied to facilitate clear observation of cerebrovascular structures by through-skull and through-scalp NIR-II fluorescence imaging. More importantly, this high SNR brain imaging was stable within 180 min, offering great potential for clinical *in vivo* brain fluorescence imaging [381].

Since membrane potential is closely related to neural activity in the brain, several voltage-sensitive organic molecules were used for imaging cell membrane potential [382]. Loew *et al*. [383] introduced a palette of fluorinated styryl dyes that show improved photostability. In addition to spanning wavelengths ranging from 440 to 670 nm, the dyes have varying degrees of voltage sensitivity, from 10% to 22% per 100 mV. Importantly, they showed improved efficacy under two-photon illumination and enabled voltage imaging in intact heart and brain slices. Bezanilla *et al*. [384] reported the use of indocyanine green (ICG) as a voltage-sensitive dye. ICG shows a modest 2% decrease in fluorescence intensity upon 100 mV depolarization, but it has sufficient signal-to-noise to track action potentials in frog oocytes expressing sodium channels and in rat dorsal root ganglia neurons. In rat brain slices, ICG could monitor field-evoked stimuli. Importantly, because ICG is FDA-approved for use in humans and has long-wavelength excitation and emission profiles, this opens up the possibility to use ICG in humans or deep tissue contexts.

6.1.2 Inorganic quantum dot fluorescent probe

Quantum dots (QDs) are promising fluorescent probes and are widely used in brain imaging due to their high quantum yields, small size, broad absorption spectrum, tunable emission spectrum, and weak photobleaching. In order to achieve highly efficient luminescent QDs for brain imaging, Qian *et al*. [385] implemented a dual-layer coating method to realize surface-functionalized PbS@CdS QDs. Silica and the amphiphilic polymer Pluronic F-127 were applied to impart water dispersibility, biocompatibility and chemical stability to PbS@CdS QDs. The obtained complex QDs displayed a high quantum yield of 5.79% at the emission wavelength of 1,155 nm, enabling *in vivo* NIR-II fluorescence imaging of mouse brain. By imaging complex QDs under 785 nm laser excitation, the cerebrovascular structures of the mouse brain at different vertical depths up to 950 μm could be observed clearly. In addition, 3D reconstructed image, overlay image, and 4D fluorescence videos of mouse brain were captured, showing great potential for high-contrast and deep-tissue cerebral angiography. Furthermore, Wang *et al*. [386] developed a novel "turn-on" activatable nanoprobe named V&A@Ag_2S for early diagnosis and real-time feedback of traumatic brain injury. This nanoprobe consisted of an $ONOO^-$ responsive A1094 chromophore and 1,050 nm-emitted Ag_2S QDs. Since the absorption spectrum of A1094 and the emission spectrum of Ag_2S overlap, efficient fluorescence resonance energy transfer occurred between Ag_2S and A1094 chromophore, leading to a "turn-off" strategy in common environments. However, the fluorescence of Ag_2S quantum dots could "turn on" by bleaching of A1094 in the presence of $ONOO^-$, which could be used for early real-time diagnosis of traumatic brain injury. The *in vivo* experiment results showed that by intravenously injecting V&A@Ag_2S nanoprobes into a traumatic brain injury mouse model, rapid and specific fluorescent signals were observed in the region of traumatic brain injury. In addition, superior targeted-to-normal tissue signal ratio and stable fluorescence signal were detected by using V&A@Ag_2S nanoprobes, providing an activatable *in vivo* turn-on strategy for the fluorescence imaging of functional brain regions (Figure 14b).

Benefiting from the advantages of QDs mentioned above, Wang *et al*. [387] synthesized glutathione-capped CdSe@ZnS quantum dots (CdSe@ZnS-GSH QDs) with a size of 2.5 nm and an emission peak at 520 nm, for plasma membrane labeling and membrane potential imaging. The as-synthesized CdSe@ZnS-GSH QDs can effectively label cell membrane at neutral pH within 30 min and exhibit excellent optical stability in continuous imaging for up to 60 min. Meanwhile, CdSe@ZnS-GSH QDs show high biocompatibility to cells and do not affect cell proliferation, disturb cell membrane integrity or cause apoptosis and necrosis of cells. The study offered a facile strategy for labeling plasma membrane and monitoring the membrane potential of cells and will hold great potential in the research of signaling within intact neuronal circuits.

6.1.3 Fluorescent protein probe

Fluorescent protein probes are effective toolboxes for non-invasive labeling and imaging. Unlike other fluorescent probes, fluorescent proteins are usually encoded in plasmid and expressed by microorganisms and mammalian cells. They have good biocompatibility, rational design ability and easy construction procedures [388]. Fluorescent proteins are often imaged by transfecting relevant genes and expressing them into living cells and tissues. However, the limited transfection efficiency and low fluorescence intensity of fluorescent protein probes greatly restrict their practical applications. In order to overcome the shortcomings of unimpressive brightness and slow expression of fluorescent proteins in brain tissue, Campbell *et al*. [389] developed a novel bright monomeric fluorescent protein mGreenLantern by rationally introducing a folding-enhanced mutation of avFP into a GFP template. MGreenLantern displayed high fluorescence intensity, which was 6-fold brighter than that of

enhanced green fluorescent protein (EGFP) in cells. In addition, mGreenLantern displayed high transfection efficiency for neurons, enabling neuronal tracing measurements in live mouse brain. Long-range projections of neurons in the brain were detected clearly under both 488 and 514 nm excitation. By implanting a cranial window over the brain, mGreenLantern rapidly filling neuronal process *in vivo* was detected through 2P microscope imaging. Furthermore, wide-field microscopy imaging also revealed that mGreenLantern-stained neurons in the brain were more easily detected *in vivo* than EGFP-stained neurons. Campbell *et al*. [390] inserted (CaM)-RS20 into mIFP and developed a genetically encoded fluorescent calcium ion indicator (NIR-GECO1). In the indicator, CaM-RS20 handled the ability to modulate the environment of the biliverdin chromophore by binding with Ca^{2+} ions, thereby tuning the fluorescence intensity of the indicator. It was linked to mIFP *via* N- and C-terminal linkers through a genetically encoded process. The achieved NIR-GECO1 showed a maximum emission of ~704 nm under 678 nm excitation. In order to verify the activation of NIR-GECO1 in the brain, the NIR-CECO1 gene carried by adeno-associated virus was injected into the sensorimotor cortex of mice. The results displayed that NIR-CECO1 was deficient for *in vivo* imaging of neuronal activity, but it could serve as the preferred Ca^{2+} indicator to image Ca^{2+} transients in brain tissue with high sensitivity.

In addition to being widely used for Ca^{2+} imaging, fluorescent protein probes were also used for membrane potential imaging. Knöpfel *et al*. [391] reported that genetically encoded voltage-sensitive fluorescent proteins (VSFPs) provide an optical voltage report from targeted neurons in culture, acute brain slices and living mice. By expressing VSFPs in pyramidal cells of mouse somatosensory cortex, these probes reported cortical electrical responses to single sensory stimuli *in vivo*. These protein-based voltage probes will facilitate the analysis of cortical circuits in genetically defined cell populations and are hence a valuable addition to the optogenetic toolbox. Pieribone *et al*. [392] reported a fluorescent protein voltage sensor, named ArcLight. The probe responded to a 100 mV depolarization with signals more than five times larger than those of previously reported Ciona intestinalis voltage sensor (CiVS)-based FP voltage sensors. ArcLight and its derivatives represent a very substantial improvement in the signal size of a fluorescent protein voltage sensor, providing a protein-based method to monitor action potentials and subthreshold depolarization in neurons and potentially other cells and organelles.

6.1.4 Lanthanide-based fluorescent probe

Lanthanide-based materials with special 4f electronic structures display great optical advantages, including tunable emission, long lifetime, non-blinking, excellent photostability, and high SNR. Their unique upconversion process can provide a broad range of emission *via* NIR irradiation activation. In addition, they can also emit near-infrared (NIR) light that effectively penetrates deep tissue and skull through the down-conversion process. These optical characters allow lanthanide-based materials to be used for upconversion luminescence (UCL) and NIR imaging of the brain, providing great advantages and application prospects for brain imaging.

By exploiting the upconversion fluorescence of lanthanide-based materials, Liu *et al*. [393] developed a kind of dye-sensitized lanthanide-doped upconversion nanoparticles for high-contrast *in vivo* brain imaging. The nanocrystals of $NaYF_4$:20%Yb, 2%Er@$NaYF_4$:20%Nd were synthesized as fluorescent centers. Three NIR dyes, Car-Cl, Alk-Cl and Alk-pi, were developed to sensitize the upconversion fluorescence of lanthanide-doped nanoparticles. They optimized the coordination interaction between dyes and the lanthanide-doped nanocrystals by delicately modulating the structure of the dye. Taking advantage of the large absorption cross-section of organic dyes, upconversion luminescence of lanthanide-doped nanocrystals was improved extremely through an energy-transfer cascade of dyes→Nd^{3+}→Yb^{3+}→Er^{3+}. As a result, the obtained Alk-pi sensitized nanocrystals achieved a 600-fold upconversion fluorescence enhancement in the aqueous phase under 808 nm excitation, displaying a strong upconversion fluorescence signal in the mouse brain without craniotomy or skull thinning. Finally, the 3D-reconstructed morphology of the cerebral blood vessels was established, and the 3D reconstruction was observed through Z-scanning by using laser-scanning confocal microscopy.

In addition to upconversion fluorescence imaging, downconversion fluorescence imaging at the NIR-II region of 1,000–1,700 nm provides an alternative approach for *in vivo* brain imaging. The photon scattering and photon absorption at the NIR-II region are greatly suppressed. Thus, NIR-II fluorescence imaging possessed diminished autofluorescence, high SNR, deep-tissue penetration and low tissue thermal damage, which affords the *in vivo* brain imaging with high spatial resolution. Zhong *et al*. [394] synthesized a bright downconverting fluorescent nanoprobe with the NIR-II emission of 1,550 nm. This nanoprobe consisted of a 2% Er and 2% Ce co-doped $NaYbF_4$ core and an inert $NaYF_4$ shell. Ce^{3+} was doped into the core to promote the downconversion emission of Er^{3+} ions. The inert $NaYF_4$ shell with a thickness of ~7 nm was applied to shield the aqueous quenching effect, resulting in a ~9-fold increase in the brightness of the 1,550 nm emission. Furthermore, amphiphilic PMH and mPEG-NH_2 were further capped on the surface of the nanocrystals to improve the dispersibility and biocompatibility. By intravenous injection of these modified lanthanide-based nanocrystals, *in vivo* cerebral vascular imaging was realized by detecting the NIR-II

fluorescence of 1,550 nm under the exaction of 980 nm. Moreover, benefiting from the bright emission of the nanoprobes, fast *in vivo* dynamical imaging with a short exposure time of 20 ms was performed for tracking the arterial blood flow in the mouse brain (Figure 14c). Owing to this short temporal resolution, a spatially resolved map of blood-flow in the brain was obtained, which facilitated real-time monitoring and tracking of cerebrovascular-related diseases.

In order to further improve the fluorescence intensity of the probes and achieve better brain imaging, Zhang *et al*. [395] designed an eribium (III)-bacteriochlorin composites (EB766)-based fluorophore system for NIR-II brain imaging. In this bacteriochlorin-sensitized NIR probe, bacteriochlorin acted as the antenna ligand to directly populated the photons at the $^4I_{13/2}$ levels of Er (III), displaying efficient light harvesting and sensitization efficiency. EB766 excited at 760 nm and emitted around 1,530 nm, which was beneficial for deep tissue imaging. The EB766 enabled fluorescence imaging of cerebral vessels underneath the intact scalp and skull with a high SNR value of ~8.65 to 12.95, which was much higher than that of other NIR-II fluorophores (~2.0–7.3). Furthermore, the cell-tracking probe CT1530 was further prepared through the interaction of EB76, BSA and cell-penetrating peptide HIV-TAT. The implemented CT1530 could be used to label cancer cells to simulate brain metastases and support high single-cell resolution imaging at 2 mm depth in the hippocampus, providing an assistant method for monitoring cell movement, migration, and residency in the cerebrovascular wall and brain regions.

6.2 Fluorescent technologies for brain functional imaging

In addition to various fluorescent probes for brain imaging, the rapid development of fluorescent technology also promotes *in vivo* brain fluorescence imaging dramatically. Advanced fluorescence imaging techniques can even further facilitate the study of specific structures or functions in the brain regions at the subcellular or cellular level. Fluorescent technologies used for brain imaging mainly include wide-field fluorescence imaging, confocal laser scanning microscope imaging, fiber photometry and other fluorescent technologies.

6.2.1 Wide-field fluorescence imaging

Wide-field fluorescence imaging technology is one of the most important and commonly used methods in life science microscopy. It can illuminate the entire brain at once and possess the advantages of fast detection, low cost, and convenience to use. However, owing to the strong light-scattering effects of the skin and skull, the low imaging resolution, low SNR and shallow imaging depth restrict the applications of wide-field fluorescence imaging greatly. With the development of fluorescence microscopy imaging technology, fluorescence imaging in the NIR-II region has a higher definition and deeper tissue penetration ability, which broadens the *in vivo* brain imaging extremely, showing great potential in both basic research and clinical applications. NIR wide-field fluorescence imaging can be used for microangiography, local tumor imaging, trauma detection, and imaging of functional structure/molecules in brain regions.

Liu *et al*. [396] developed a series of polymethine-based Pots with emission and absorption in the NIR-II region to extend *in vivo* wide-field fluorescence imaging. Pttc-SeBTa-NIR 1125 and Pttc-SeBTA-NIR 1380 Pots with excellent water stability were synthesized by bonding the bulky semiconducting polymer Pttc-SeBTa-PFCOOH with the polymethine dyes NIR 1125 and NIR 1380 *via* a click reaction. The QYs of Pttc-SeBTa-NIR 1125 and Pttc-SeBTA-NIR 1380 Pots were 0.18% and 0.05%, respectively. In addition, their fluorescence intensity was ~1–2 orders of magnitude higher than that of traditional NIR dyes. Due to high fluorescence quantum yield and fluorescence intensity, Pttc-SeBTa-NIR 1125 and Pttc-SeBTA-NIR 1380 Pots could be used for *in vivo* fluorescence imaging with nearly zero autofluorescence, high spatial resolution and high SNR value. As a trade-off between fluorescence brightness and spatial resolution, 1,100 and 1,250 nm long-pass filters were selected during the *in vivo* imaging. Both Pots enable the visualization of cerebral blood vessels through intact scalp and skull under non-invasive wide-field fluorescence imaging. Furthermore, taking advantage of the reduced photon absorption/scattering, malignant brain tumors could also be diagnosed in the NIR-II window, providing a promising technique for early diagnosis of brain. Tang *et al*. [397] also developed novel bright AIE dots with NIR-II emission for *in vivo* brain imaging of large-size animals such as rats. The stronger light scattering in rats' brain caused by larger blood vessels and thicker vascular walls makes brain imaging more difficult to achieve than that in mice. The obtained AIE dots possess the photoluminescence quantum yield of 5.07%, 2.42%, 0.76% and 0.22% at the emission beyond 900, 1,000, 1,100, and 1,200 nm, which was sufficient for brain imaging. By further adjusting the LP filters during imaging process, the small cerebrovascular structure of the rat was visualized clearly with a high SNR of 2.82 and a high resolution of 18.9 μm. In addition, the blood vasculature of the rat brain could also be imaged at depths up to 700 μm. Furthermore, the blockage of single blood vasculature in rats' brain was also detected, providing a useful technology for monitoring and understanding the brain diseases.

6.2.2 Confocal laser scanning microscope

Although wide-field fluorescence imaging technology can image the brain rapidly, the restricted spatial resolution hinders their further developments and applications [398].

The cluttered background of the defocused signal also overlay on the image, blurring the entire imaging greatly and resulting in poor imaging quality. In order to overcome this deficiency, the confocal laser scanning microscope containing a pinhole is developed and applied to provide *in vivo* imaging with high spatial resolution and optical sectioning capabilities. The pinhole is located at the conjugate position corresponding to the focus. Owing to the existence of the pinhole, only a small part of the signal at the focus point could be eventually collected by microscopy, and the out-of-focus signal is rejected by the pinhole, thus obtaining a higher imaging spatial resolution.

To obtain high spatial resolution imaging at different depths *in vivo*, Qian *et al*. [399] established a confocal laser scanning microscopy system for brain imaging (Figure 15a). In this system, an optical fiber with a diameter of ~300 μm was applied as a pinhole. During the imaging process, the scan speed was set to 10 μs pixel^{-1}, and the scan area was 512 pixels × 512 pixels. In addition, highly fluorescent AIE dots named TB1 were developed as the NIR-II fluorescent probes. TB1 possessed a high quantum yield of 6.2%, which was sufficient to support *in vivo* confocal fluorescence imaging. A 793 nm laser with low tissue absorption was applied to excite the fluorescent probes. As a result, the cerebrovascular structure of mice at different depths through the skull was observed clearly. Imaging depths could reach more than 800 μm. Moreover, tiny capillaries with small diameters of 5.77 and 8.78 μm at depths of 350 and 700 μm could also be distinguished easily. Furthermore, the 3D structure of cerebral blood vessels was further reconstructed by using this homemade confocal microscopy system. Li *et al*. [400] developed ICG-assisted NIR-II fluorescent probes and applied them to brain imaging by using NIR-II fluorescence confocal microscopy. The FDA-approved ICG with a high quantum yield of ~4.2% was intramuscularly injected into the mice with craniotomy. A scanning speed of 20 μs pixel^{-1} and the scanning areas of 512 pixels × 512 pixels were set during imaging. Owing to the high spatial resolution, low SNR, and optical sectioning capability of NIR-II fluorescence confocal microscopy, cerebral vessels at various depths beyond 300 μm could be visualized clearly. tiny capillaries with a small diameter of 2.66 μm could be identified at a depth of 300 μm, showing a much higher spatial resolution than that of wide-field fluorescence imaging.

6.2.3 *Fiber photometry*

Fiber photometry uses optical fibers to deliver and collect fluorescent signals, enabling the recording and studying of complex neuronal behaviors in deep regions of the brain. Fluorescent sensors are usually pre-injected into brain

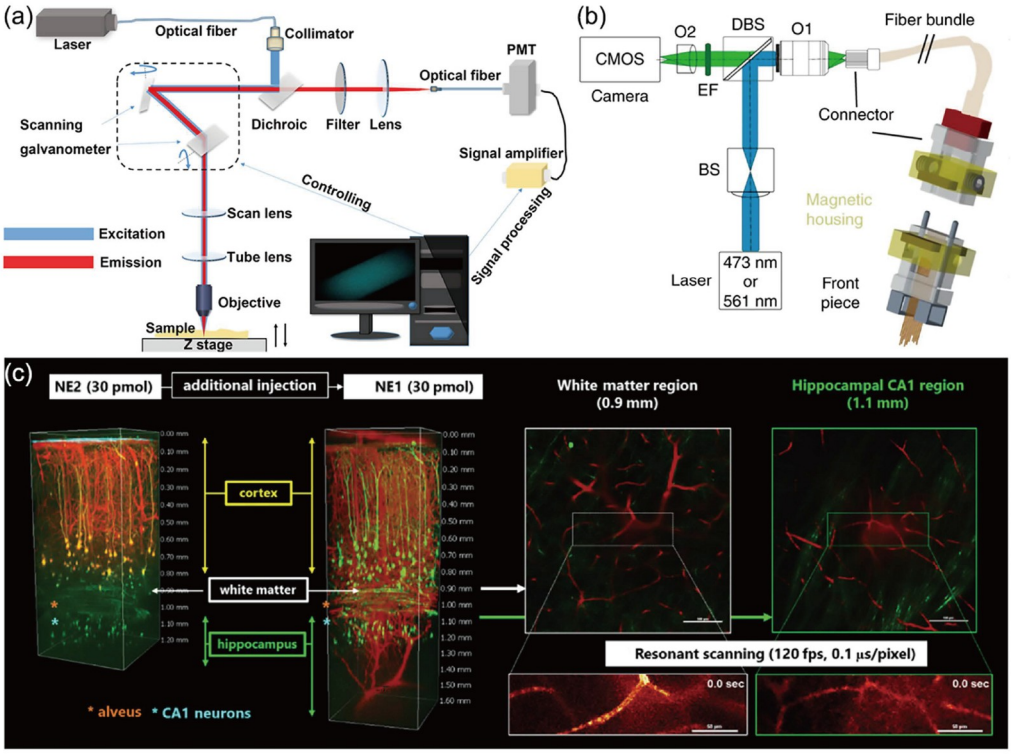

Figure 15 The brain imaging by using different fluorescent technologies. (a) Setup of confocal laser scanning microscopy system. Adapted with permission from Ref. [399], copyright by Science China Press (2019). (b) Setup of multi-fiber photometry system. Adapted with permission from Ref. [401], copyright by Nature Publishing Group (2019). (c) 3D reconstruction and 2D image of cerebral vasculature by using two-photon microscopy. Adapted with permission from Ref. [402], copyright by Wiley-VCH GmbH (2021) (color online).

regions. Changes in fluorescence emission during the simulated behavior are then collected through optical fibers. Fiber photometry offers a simple method for optical recordings from brain regions, which is versatile and shows the practical potential of implanting fibers into the brain.

However, the commonly used fiber photometry still has limitations, such as the inability to collect the fluorescence signals from multiple regions, tissue damage caused by long-term implantation of optical fibers, and limited multi-color measurements of brain regions.

To broaden the practical application of fiber photometry, Pisanello *et al*. [403] developed a novel tapered optical fiber to monitor neural activity in brain regions. Unlike flat-cleaved fibers that can only achieve fluorescence signals in the shallow tissue surrounding the fiber, tapered optical fiber enables the deep light collection of up to 2 mm due to the geometry of the probe. In addition, the multi-spot photometry along the taper could also be realized by adjusting the numerical apertures, taper angle and laser input angle of the fiber. By utilizing tapered optical fiber, differential dopamine transients in the dorsal and ventral striatum were measured. The results showed that dopamine transients in both dorsal and ventral striatum were responsive to locomotion, and only dopamine transients in the ventral striatum were strongly associated with reward. Furthermore, optical signal acquisition in brain regions at arbitrary depth *in vivo* was realized by injecting a laser beam at different input angles. By combining multiple optical fibers together, Helmchen *et al*. [401] developed a high-density multi-fiber array to support simultaneously multi-fiber photometric measurements of entire brain regions (Figure 15b). By chronically implanting multi-fibers into the mouse brain, behavior-related neuronal dynamics in 12–48 brain regions could be measured simultaneously, enabling the recording of calcium signals from large mesoscale networks, including the striatum, thalamus, hippocampus and cortical areas. Furthermore, the combination of targeted optogenetic perturbations with multi-fiber photometry provided a feasible method for manipulating perturbations and studying how these perturbations affect animal behavior. Finally, multi-fiber photometry of freely moving mice during social interaction was demonstrated.

6.2.4 *Functional near-infrared spectroscopy (fNIRS)*

Functional near-infrared spectroscopy (fNIRS) is a critical method for functional brain imaging, which can be used to identify brain functional connectivity in the absence of radiation. Compared with other techniques, such as functional magnetic resonance imaging (fMRI), fNIRS is inexpensive, portable, accessible to a wider population, and can be used in flexible and complicated conditions. Moreover, it can measure oxyhemoglobin (HbO) and deoxyhemoglobin (HbR) simultaneously, showing great potential in studying brain functional connectivity in neurodegenerative diseases.

The brain provides necessary oxygen for neuronal activities through metabolism, and the consumption of oxygen stimulates local vasodilation in the brain, which is manifested as a rapid increase in the oxygen content of the cerebral blood. During the cognitive activity of the brain, the oxygen content carried by the cerebral blood flow in the neural activity area of the brain exceeds the oxygen content required by the brain activity. Oxygen is transmitted through the hemoglobin in the blood. Therefore, the content of HbO in the blood increases in the active area of the brain, while HbR decreases during the cognitive activities of the brain. Oxygen, hemoglobin and deoxyhemoglobin have different absorption spectra under the near-infrared window. The concentration changes of oxyhemoglobin and deoxyhemoglobin can be inferred from changes in light intensity passing through this brain region, enabling monitoring of brain functional activities. Under this mechanism, Kim *et al*. [404] used fNIRS technology to investigate the brain functional connectivity in patients with mild cognitive impairment. Compared with healthy adults, different brain functional connectivity in patients was observed during resting-state and verbal fluency tasks. The results suggest that interhemispheric connectivity can be used to indicate patients with mild cognitive impairment. By using fNIRS technology, Ho *et al*. [405] also found that patients with the major depressive disorder had reduced changes in hemodynamic responses during the English alphabet fluency task, which can serve as an objective and quantitative assessment of depressive psychotic patients.

6.2.5 *Other fluorescent technologies*

In addition to these fluorescence imaging techniques, multi-photon microscopies are being developed for fine and accurate imaging of the brain. Niko *et al*. [402] developed high-speed two-photon microscopy to noninvasively visualize and analyze vascular dynamics in the cerebral cortex and CA1 region of the hippocampal in mouse brain. The biocompatible nanoemulsions consisting of Labrafac WL inner core and Cremophor ELP shell were prepared *via* spontaneous nanoemulsification to carry the LipoPYF5 fluorescent dye. A Ti:sapphire excitation laser in the wavelength range of 700–1,040 nm was used as the excitation source, and a high-sensitivity gallium arsenide phosphide (GaAsP) non-descanning detector was applied to record fluorescence signal. By injecting LipoPYF5 loaded nanoemulsions through the fundus vein, the cerebrovascular system could be visualized clearly at a depth of 1.5 mm. The 3D reconstruction of cerebral vasculature was further established with a long excitation dwell time of 57.2 μs pixel^{-1} (Figure 15c). In addition, a shorter excitation dwells time of 0.1 μs pixel^{-1} was set for high-speed *in vivo* two-photon microscopy imaging. As a result, blood flow in multiple blood vessels in the hippocampal CA1 region could be detected simultaneously,

providing a powerful tool for visualization and study of deep cerebral vasculature.

Out-of-focus fluorescence near the surface greatly limits the depth of two-photon microscopic imaging of brain regions. Tissue heterogeneity, refractive index mismatches, and subtle motion artifacts in the deep brain cause optical aberrations, resulting in limited observation of subcellular information. To overcome these limitations, Prevedel *et al.* [50] developed an adaptive optics three-photon microscopy for deep-brain imaging with cellular resolution. The three-photon excitation microscopy (3P) used a longer wavelength excitation of 1,300 nm, which substantially increased the SNR for deep brain imaging. Additionally, the indirect, modality-based adaptive optics (AO) method was used to measure and compensate for optical aberrations, which helps push the depth limits of deep brain imaging. Moreover, an active electrocardiogram gating method was also incorporated to reduce the duty cycle of the image acquisition, enabling the visualization of individual spines in deep tissue of hippocampus regions. By exploiting this self-regulating 3P-AO scope, hippocampus CA1 neurons and dendrites could be observed clearly at the depth of 1.45 mm in the dorsal hippocampus. Furthermore, Ca^{2+} transients in astrocytes that located in the scattering corpus callosum were recorded successfully.

6.3 Raman spectroscopy for imaging and biosensing in the live brain

6.3.1 Raman probes for brain functional imaging

Surface-enhanced Raman spectroscopy (SERS) provides an effective strategy for simultaneously monitoring multiple substances due to the high spectral resolution of molecular fingerprint information, with resistance to photobleaching and autofluorescence [406–408]. Based on the enhancement mechanism, SERS probes for brain functional imaging have been designed typically with two types: metallic and non-metallic substrates-based Raman probe.

As for metallic substrate-based Raman probe, the Raman reporter molecules are attached to a metal nanoparticle or a layer of the rough gold film. Tian *et al.* [52] established a ratiometric optophysiological SERS microarray of eight microprobes with tip sizes of 5 μm to map in real-time and quantify CO_3^{2-} and pH simultaneously in a live brain (Figure 16a). In this work, quartz tapers (QTs) with different tip sizes from 50 nm to 5 μm were sputtered with a layer of rough gold film. Then, 1-(4-aminophenyl)-2,2,2-trifluoroethanone (AT) and 4-mercaptobenzoic acid (MBA) were optimized as the specific recognition elements for CO_3^{2-} and pH, respectively, and co-modified onto the Au-QTs for imaging and biosensing both the CO_3^{2-} concentration and the pH

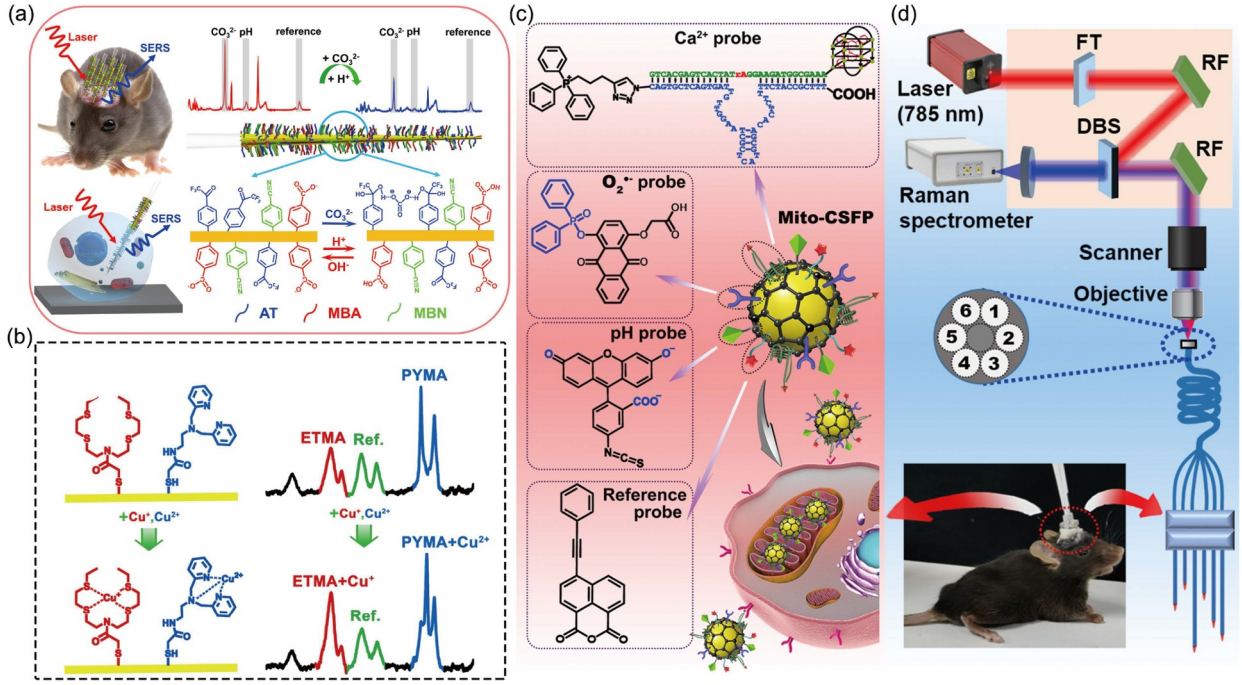

Figure 16 Raman spectroscopy for imaging and biosensing in the live brain. (a) The principle of the developed SERS probe for the simultaneous biosensing of CO_3^{2-} concentration and pH value in live brains and single neurons. Adapted with permission from Ref. [52], copyright by Wiley-VCH GmbH (2019). (b) The principle of the dual-recognition mode of the developed CuSP probe for simultaneous recognition of Cu^{+} and Cu^{2+}. Adapted with permission from Ref. [51], copyright by Wiley-VCH GmbH (2021). (c) Schematic diagram of the designed Raman Mito-CSFP probe for simultaneous determination of $O_2^{\cdot-}$, Ca^{2+} and pH. Adapted with permission from Ref. [53], copyright by Wiley-VCH GmbH (2021). (d) Optical setup of 6-channel Raman fiber photometry. FT, RF and DBS represent filter, reflector and dichroic beam splitter, respectively. Adapted with permission from Ref. [53], copyright by Wiley-VCH GmbH (2021) (color online).

value while 4-mercaptobenzonitrile (MBN) with a C≡N group was employed as an inner reference for providing a built-in correction. It was found that both the CO_3^{2-} concentration and the pH value dramatically decreased under ischemic conditions. This work has not only provided a novel method for the development of biosensors to determine simultaneously multiple biological species in live animal models, but also opened up a way to understand the roles of chemical species in brain [60]. To further expand the applications of SERS in brain imaging, Tian *et al*. [51] further developed a SERS probe for real-time monitoring and accurately quantifying the concentrations of Cu^+ and Cu^{2+} in the live mouse brain. Two molecules *N*,*N*-bis(2-((2-(ethylthio) ethyl) thio) ethyl)-2-mercaptoacetamide (ETMA) and *N*-(2-(bis(pyridin-2-ylmethyl) amino) ethyl)-2-mercaptoacetamide (PYMA) for specific recognition of Cu^+ and Cu^{2+} were self-assembled onto an Au-QT (denoted as CuSP), demonstrating specific ability for simultaneously recognizing Cu^+ and Cu^{2+} (Figure 16b). By using the developed SERS probe, it was found for the first time that the concentrations of Cu^+ and Cu^{2+} were increased by about 4.26 and 1.80 times upon ischemia respectively. There were three mechanisms of the increased concentrations of Cu^+ and Cu^{2+} during ischemia: Cu^+ and Cu^{2+} are released from copper-containing proteins destroyed during ischemia; the more decrease in the concentration of Cu^{2+} are possibly ascribed to the conversion from Cu^+ to Cu^{2+} both inside and outside the neurons upon ischemia.

As for nonmetallic substrate-based Raman probe, the Raman enhancement was realized based on the charge transfer between semiconductor material and Raman reporter molecules. Tian *et al*. [53] created a highly selective non-metallic Raman probe based on graphene oxide-titanium dioxide (GO-TiO_2) nanocomposites, for simultaneously monitoring of O_2^-, Ca^{2+} and pH with high selectivity (Figure 16c). A specific O_2^- Raman probe (SOP) was designed consisting of two parts: one was phosphinate as a specific recognition group of O_2^-, and the other was 1-carboxy-4-hydroxyanthraquinone (CHQ) as a Raman reporter. Then, Ca^{2+} Raman probe (CaP) was synthesized containing three parts: DNAzyme played as specific recognition domain for Ca^{2+}, G-quadruplex was designed for binding copper phthalocyanine (CuPC) as Raman reporter, and triphenylphosphine (TPP) was employed as mitochondria-targeting molecule. Meanwhile, fluorescein isothiocyanate isomer (FITC) was used to specifically identify pH. In addition, 6-(phenylethynyl)-1H,3H-benzo[de] isochromene-1,3-dione (PBI) was selected as reference probe to provide reference Raman signal for built-in corrections with high quantitative accuracy and indicate the transport of intracellular probe. Finally, the designed CaP, SOP, FITC and PBI recognition molecules were assembled onto GO-TiO_2 nanocomposites to construct a mitochondria-targeted Raman probe, named as Mito-CSFP. The developed Raman probe displayed high selectivity and accuracy, as well as good stability and biosafety.

6.3.2 Raman fiber photometry

Although Raman probes have already been used for biosensing of chemical species in the brain, the relatively limited penetration of excitation light prevents current Raman probe from being applied to deep brain. Fiber photometry techniques for brain functional imaging employ an optical fiber implanted into the brain to study the function of multiple brain regions. Tian *et al*. [53] built up a Raman fiber photometry to simultaneously record mitochondrial Raman signals from six brain regions across a whole network of freely moving animals, which was successfully applied for studying the relationship of multiple molecules in the mitochondria of the live brain (Figure 16d). The Raman fiber photometry consisted of six multimode fibers (200 μm core/25 μm cladding) bundled together tightly at one end and separated independently at the other end. The excitation light (785 nm) was first delivered into the confocal scanner, and then coupled to the bundled end of optical fiber by an objective (10×), further to excite the Raman probes at another end of fiber. Subsequently, Raman signals of the probes were collected with the same optical fiber and then detected by a Raman spectrometer. The excitation light was coupled into different fibers individually through the confocal scanner, and the end of each separated fiber was tapered with the optimized vertebral angle of 10.6° to improve the signal collection efficiency and reduce invasive. With the assistance of the developed Raman probe and Raman fiber photometry, it was firstly found that mitochondrial O_2^-, Ca^{2+} and pH values change from superficial brain areas to deep brain areas, accompanied with the decreasing in the concentrations and rates during acute hypoxia. This indicates that the developed fiber Raman system is a useful and powerful tool for not only real-time tracking and quantitation of multiple molecules in mitochondria across multiple brain regions but also understanding the molecular mechanisms of functional networks related to brain diseases, and further exploring the potential drugs for prevention and treatment of diseases, such as hypoxia, ischemia, stroke and epilepsy.

7 Summary and outlook

As summarized in this review, a variety of techniques for brain structure imaging were overviewed, including MRI, CT, positron emission tomography (PET), ssEM, LM and synchrotron-based XRM. These imaging techniques provided abundant information for brain structure with multiple scales, from single cells to tissues, from cortex to deep brain areas across the whole brain. On the other hand, new technologies of electrophysiology for recording electrical signals

at the single-neuron level and in the brain were introduced. Moreover, frontier methods including probes and instruments for biosensing of chemical signals in the brain were highlighted, covering electrochemical techniques, MRI, fluorescence and Raman methods. These probes and instruments provided powerful tools to obtain the concentration changes, spatial distribution and interactions of intracellular or extracellular chemical species, thereby discovering and analyzing neural activities and neural signal transductions in the brain.

Due to the complexity of brain structure, current methods for *in vivo* brain structure imaging are limited by low resolution, while high-resolution brain structure imaging techniques are difficult to be applied to *in vivo* imaging analysis. It is desirable to develop new techniques for *in vivo* brain structure imaging with high spatial and temporal resolutions. Moreover, considering that the complex brain environment involves a variety of chemical species, it is necessary to explore new sensing strategies with high selectivity, sensitivity and accuracy, to achieve real-time high-throughput analysis of more chemical signals (>10) both in extracellular and intracellular, for eventually realizing large-scale dynamically recording of neuronal signaling with chemical expression across the whole brain of freely moving mouse. Furthermore, in view of the complex mechanism of the brain, it is essential to build new instruments and create multifunctional probes that can simultaneously image brain structure and function in the future, to understand the molecular mechanisms of functional networks related to brain diseases, and further to explore potential drugs for prevention and treatment of diseases.

Acknowledgements This work was supported by the National Natural Science Foundation of China (22004037 for Liu Z; 22022410 and 82050005 for Zhu Y; 22022402 and 21974051 for Zhang L; 21635003 and 21811540027 for Tian Y; 22125701 and 21834007 for Liu K; 22020102003 for Zhang H; 91859206 and 21921004 for Zhou X), the Innovation Program of Shanghai Municipal Education Commission (201701070005E00020 for Tian Y), the Research Funds of Happiness Flower ECNU (2020JK2103 for Tian Y), the Shanghai Municipal Science and Technology Commission (19JC1410300 for Fan C), the Youth Innovation Promotion Association of CAS (2016236 for Zhu Y), and the National Key Research and Development Project of China (2018YFA0704000 for Zhou X).

Conflict of interest The authors declare no conflict of interest.

1 Wang Y, Tan H, Hui X. *Biomed Res Int*, 2018, 2018: 7848901
2 Uddin MJ, Zidorn C. *Nat Prod Bioprosp*, 2020, 10: 377–410
3 Cabrera DeBuc D, Somfai GM, Arthur E, Kostic M, Oropesa S, Mendoza Santiesteban C. *Front Physiol*, 2018, 9: 1721
4 Shipp S. *Curr Biol*, 2007, 17: R443–R449
5 Wang Q, Ding SL, Li Y, Royall J, Feng D, Lesnar P, Graddis N, Naeemi M, Facer B, Ho A, Dolbeare T, Blanchard B, Dee N, Wakeman W, Hirokawa KE, Szafer A, Sunkin SM, Oh SW, Bernard A, Phillips JW, Hawrylycz M, Koch C, Zeng H, Harris JA, Ng L. *Cell*, 2020, 181: 936–953
6 Carlén M. *Science*, 2017, 358: 478–482
7 Rasman BG, Forbes PA, Peters RM, Ortiz O, Franks I, Inglis JT, Chua R, Blouin JS. *eLife*, 2021, 10: e65085
8 Chang RB, Strochlic DE, Williams EK, Umans BD, Liberles SD. *Cell*, 2015, 161: 622–633
9 Denoth-Lippuner A, Jessberger S. *Nat Rev Neurosci*, 2021, 22: 223–236
10 Hudetz AG, Humphries CJ, Binder JR. *Front Syst Neurosci*, 2014, 8: 234
11 Rings T, Mazarei M, Akhshi A, Geier C, Tabar MRR, Lehnertz K. *Sci Rep*, 2019, 9: 1744
12 Osmanlıoğlu Y, Tunç B, Parker D, Elliott MA, Baum GL, Ciric R, Satterthwaite TD, Gur RE, Gur RC, Verma R. *NeuroImage*, 2019, 199: 93–104
13 Fu Z, Sui J, Turner JA, Du Y, Assaf M, Pearlson GD, Calhoun VD. *Hum Brain Mapp*, 2021, 42: 80–94
14 Zhao L, Wang E, Zhang X, Karama S, Khundrakpam B, Zhang H, Guan M, Wang M, Cheng J, Shi D, Evans AC, Li Y. *Biomed Res Int*, 2015, 2015: 1–23
15 Tang Q, Li J, Zhu Y, Wang L, Tian Y, Fan C, Hu J. *Chem J Chinese U*, 2022, 43: 20220379
16 Konkel L. *Environ Health Perspect*, 2018, 126: 112001
17 Pugh JR, Raman IM. *Trends Neuroscis*, 2009, 32: 170–177
18 van Veenendaal TM, Backes WH, Tse DHY, Scheenen TWJ, Klomp DW, Hofman PAM, Rouhl RPW, Vlooswijk MCG, Aldenkamp AP, Jansen JFA. *NeuroImage-Clin*, 2018, 19: 47–55
19 Onakomaiya MM, Porter DM, Oberlander JG, Henderson LP. *Hormones Behav*, 2014, 66: 283–297
20 Petushkova AI, Zamyatnin Jr. AA. *Biomolecules*, 2020, 10: 650
21 Wang H, Jordan VC, Ramsay IA, Sojoodi M, Fuchs BC, Tanabe KK, Caravan P, Gale EM. *J Am Chem Soc*, 2019, 141: 5916–5925
22 Kavalali ET. *Nat Rev Neurosci*, 2015, 16: 5–16
23 Reiner A, Levitz J. *Neuron*, 2018, 98: 1080–1098
24 Grace AA. *Nat Rev Neurosci*, 2016, 17: 524–532
25 Mumtaz F, Khan MI, Zubair M, Dehpour AR. *Biomed Pharmacother*, 2018, 105: 1205–1222
26 Barnham KJ, Bush AI. *Curr Opin Chem Biol*, 2008, 12: 222–228
27 Zhang X, Liang M, Qin W, Wan B, Yu C, Ming D. *Front Hum Neurosci*, 2020, 14: 244
28 Tereshchenko S, Kasparov E. *Behaval Sci*, 2019, 9: 62
29 Shahbazi A, Kinnison J, Vescovi R, Du M, Hill R, Joesch M, Takeno M, Zeng H, da Costa NM, Grutzendler J, Kasthuri N, Scheirer WJ. *Sci Rep*, 2018, 8: 14247
30 Lee TJ, Lewallen CF, Bumbarger DJ, Yunker PJ, Reid RC, Forest CR. *J Colloid Interface Sci*, 2018, 531: 352–359
31 Bourne JN, Harris KM. *Curr Opin Neurobiol*, 2012, 22: 372–382
32 Chen Y, Akin O, Nern A, Tsui CYK, Pecot MY, Zipursky SL. *Neuron*, 2014, 81: 280–293
33 Beyene AG, Yang SJ, Landry MP. *J Vacuum Sci Tech A*, 2019, 37: 040802
34 Tsai D, Yuste R, Shepard KL. *IEEE Trans Biomed Circuits Syst*, 2018, 12: 13–23
35 Wang B, Wen X, Cao Y, Huang S, Lam HA, Liu T, Chung PS, Monbouquette HG, Chiou PY, Maidment NT. *Lab Chip*, 2020, 20: 1390–1397
36 Steinmetz NA, Koch C, Harris KD, Carandini M. *Curr Opin Neurobiol*, 2018, 50: 92–100
37 Eftekhari M, Assadi M, Kazemi M, Saghari M, Esfahani AF, Sichani BF, Gholamrezanezhad A, Beiki D. *BMC Med Phys*, 2005, 5: 6
38 Mullins RJ, Diehl TC, Chia CW, Kapogiannis D. *Front Aging Neurosci*, 2017, 9: 118
39 Joshi VS, Sheet PS, Cullin N, Kreth J, Koley D. *Anal Chem*, 2017, 89: 11044–11052
40 Wang R, Zhang H, Liu Q, Liu F, Han X, Liu X, Li K, Xiao G, Albert J, Lu X, Guo T. *Nat Commun*, 2022, 13: 547
41 Liu YL, Wang XY, Xu JQ, Xiao C, Liu YH, Zhang XW, Liu JT, Huang WH. *Chem Sci*, 2015, 6: 1853–1858
42 Dai Y, Liu Z, Bai Y, Chen Z, Qin J, Feng F. *RSC Adv*, 2018, 8:

42246–42252
43 Mamede AP, Santos IP, Batista de Carvalho ALM, Figueiredo P, Silva MC, Tavares MV, Marques MPM, Batista de Carvalho LAE. *Cancers*, 2021, 13: 5336
44 Jeong S, Widengren J, Lee JC. *Nanomaterials*, 2022, 12: 21
45 Braunschweig AB, Schmucker AL, Wei WD, Mirkin CA. *Chem Phys Lett*, 2010, 486: 89–98
46 Jia HR, Zhu YX, Xu KF, Pan GY, Liu X, Qiao Y, Wu FG. *Chem Sci*, 2019, 10: 4062–4068
47 Chen Y, Li X. *Biomacromolecules*, 2011, 12: 4367–4372
48 Ahrens MB, Orger MB, Robson DN, Li JM, Keller PJ. *Nat Methods*, 2013, 10: 413–420
49 Mahou P, Vermot J, Beaurepaire E, Supatto W. *Nat Methods*, 2014, 11: 600–601
50 Streich L, Boffi JC, Wang L, Alhalaseh K, Barbieri M, Rehm R, Deivasigamani S, Gross CT, Agarwal A, Prevedel R. *Nat Methods*, 2021, 18: 1253–1258
51 Liu J, Liu Z, Wang W, Tian Y. *Angew Chem Int Ed*, 2021, 60: 21351–21359
52 Wang W, Zhao F, Li M, Zhang C, Shao Y, Tian Y. *Angew Chem Int Ed*, 2019, 58: 5256–5260
53 Liu Z, Zhang Z, Liu Y, Mei Y, Feng E, Liu Y, Zheng T, Chen J, Zhang S, Tian Y. *Angew Chem Int Ed*, 2022, 61: e2111630
54 Zhu Y, Zhang J, Li A, Zhang Y, Fan C. *Curr Opin Chem Biol*, 2017, 39: 11–16
55 Zhu Y, Earnest T, Huang Q, Cai X, Wang Z, Wu Z, Fan C. *Adv Mater*, 2014, 26: 7889–7895
56 Fan C, Zhao Z. *Synchrotron Radiation in Materials Science: Light Sources, Techniques, and Applications*. Weinheim: John Wiley & Sons, 2018
57 Qiang Y, Artoni P, Seo KJ, Culaclii S, Hogan V, Zhao X, Zhong Y, Han X, Wang PM, Lo YK, Li Y, Patel HA, Huang Y, Sambangi A, Chu JSV, Liu W, Fagiolini M, Fang H. *Sci Adv*, 2018, 4: eaat0626
58 Lin ZC, Xie C, Osakada Y, Cui Y, Cui B. *Nat Commun*, 2014, 5: 3206
59 Zhang L, Tian Y. *Acc Chem Res*, 2018, 51: 688–696
60 Liu Z, Tian Y. *Sci China Chem*, 2021, 64: 915–931
61 Abbott J, Ye T, Krenek K, Gertner RS, Ban S, Kim Y, Qin L, Wu W, Park H, Ham D. *Nat Biomed Eng*, 2020, 4: 232–241
62 Zhao Y, You SS, Zhang A, Lee JH, Huang J, Lieber CM. *Nat Nanotechnol*, 2019, 14: 783–790
63 Chai X, Zhou X, Zhu A, Zhang L, Qin Y, Shi G, Tian Y. *Angew Chem Int Ed*, 2013, 52: 8129–8133
64 Dong H, Zhou Q, Zhang L, Tian Y. *Angew Chem Int Ed*, 2019, 58: 13948–13953
65 Liu L, Zhao F, Liu W, Zhu T, Zhang JZH, Chen C, Dai Z, Peng H, Huang JL, Hu Q, Bu W, Tian Y. *Angew Chem Int Ed*, 2017, 56: 10471–10475
66 Liu W, Dong H, Zhang L, Tian Y. *Angew Chem Int Ed*, 2017, 56: 16328–16332
67 Luo Y, Zhang L, Liu W, Yu Y, Tian Y. *Angew Chem Int Ed*, 2015, 54: 14053–14056
68 Zhang C, Liu Z, Zhang L, Zhu A, Liao F, Wan J, Zhou J, Tian Y. *Angew Chem Int Ed*, 2020, 59: 20499–20507
69 Huang S, Zhang L, Dai L, Wang Y, Tian Y. *Anal Chem*, 2021, 93: 5570–5576
70 Li S, Zhu A, Zhu T, Zhang JZH, Tian Y. *Anal Chem*, 2017, 89: 6656–6662
71 Zhang L, Han Y, Zhao F, Shi G, Tian Y. *Anal Chem*, 2015, 87: 2931–2936
72 Zhou J, Zhang L, Tian Y. *Anal Chem*, 2016, 88: 2113–2118
73 Zhao F, Shi GY, Tian Y. *Chin J Anal Chem*, 2019, 47: 347–354
74 Liu Y, Liu Z, Zhao F, Tian Y. *Angew Chem Int Ed*, 2021, 60: 14429–14437
75 Zhao F, Liu Y, Dong H, Feng S, Shi G, Lin L, Tian Y. *Angew Chem Int Ed*, 2020, 59: 10426–10430
76 Li H, Zhang Z, Zhong J, Ruan W, Han Y, Sun X, Ye C, Zhou X. *NMR Biomed*, 2016, 29: 220–225
77 Zhou X, Sun Y, Mazzanti M, Henninger N, Mansour J, Fisher M, Albert M. *NMR Biomed*, 2011, 24: 170–175
78 Zhou X, Mazzanti ML, Chen JJ, Tzeng YS, Mansour JK, Gereige JD, Venkatesh AK, Sun Y, Mulkern RV, Albert MS. *NMR Biomed*, 2008, 21: 217–225
79 Zhou YP, Mei MJ, Wang XZ, Huang SN, Chen L, Zhang M, Li XY, Qin HB, Dong X, Cheng S, Wen L, Yang B, An XF, He AD, Zhang B, Zeng WB, Li XJ, Lu Y, Li HC, Li H, Zou WG, Redwood AJ, Rayner S, Cheng H, McVoy MA, Tang Q, Britt WJ, Zhou X, Jiang X, Luo MH. *JCI Insight*, 2022, 7: e152551
80 Lauterbur PC. *Nature*, 1973, 242: 190–191
81 Gonçalves FG, Serai SD, Zuccoli G. *Top Magn Reson Imag*, 2018, 27: 387–393
82 Hashemi RH, Bradley WG, Lisanti CJ. *Mri: The Basics*. Philadelphia: Lippincott Williams & Wilkins, 2012
83 Nitz WR, Reimer P. *Eur Radiol*, 1999, 9: 1032–1046
84 Stanisz GJ, Odrobina EE, Pun J, Escaravage M, Graham SJ, Bronskill MJ, Henkelman RM. *Magn Reson Med*, 2005, 54: 507–512
85 Spijkerman JM, Petersen ET, Hendrikse J, Luijten P, Zwanenburg JJM. *Magn Reson Mater Phy*, 2018, 31: 415–424
86 De Coene B, Hajnal JV, Gatehouse P, Longmore DB, White SJ, Oatridge A, Pennock J, Young I, Bydder G. *Am J Neuroradiol*, 1992, 13: 1555–1564
87 Hagiwara A, Warntjes M, Hori M, Andica C, Nakazawa M, Kumamaru KK, Abe O, Aoki S. *Investig Radiol*, 2017, 52: 647–657
88 Ji S, Yang D, Lee J, Choi SH, Kim H, Kang KM. *Magn Reson Imag*, 2022, 55: 1013–1025
89 Blystad I, Warntjes JBM, Smedby O, Landtblom AM, Lundberg P, Larsson EM. *Acta Radiol*, 2012, 53: 1158–1163
90 Tanenbaum LN, Tsiouris AJ, Johnson AN, Naidich TP, DeLano MC, Melhem ER, Quarterman P, Parameswaran SX, Shankaranarayanan A, Goyen M, Field AS. *AJNR Am J Neuroradiol*, 2017, 38: 1103–1110
91 Bobman SA, Riederer SJ, Lee JN, Suddarth SA, Wang HZ, Drayer BP, MacFall JR. *Am J Neuroradiol*, 1985, 6: 265–269
92 Scheffler K, Hennig J. *Magn Reson Med*, 2001, 45: 720–723
93 Gulani V, Schmitt P, Griswold MA, Webb AG, Jakob PM. *Investig Radiol*, 2004, 39: 767–774
94 Ehses P, Seiberlich N, Ma D, Breuer FA, Jakob PM, Griswold MA, Gulani V. *Magn Reson Med*, 2013, 69: 71–81
95 Pfister J, Blaimer M, Kullmann WH, Bartsch AJ, Jakob PM, Breuer FA. *Magn Reson Med*, 2019, 81: 3488–3502
96 Warntjes JBM, Leinhard OD, West J, Lundberg P. *Magn Reson Med*, 2008, 60: 320–329
97 Schmidbauer V, Geisl G, Diogo M, Weber M, Goeral K, Klebermass-Schrehof K, Berger A, Prayer D, Kasprian G. *Eur Radiol*, 2019, 29: 7063–7072
98 Di Giuliano F, Minosse S, Picchi E, Marfia GA, Da Ros V, Muto M, Muto M, Pistolese CA, Laghi A, Garaci F, Floris R. *Magn Reson Mater Phy*, 2020, 33: 549–557
99 Cheng CC, Preiswerk F, Hoge WS, Kuo TH, Madore B. *Magn Reson Med*, 2019, 81: 1699–1713
100 Cheng CC, Preiswerk F, Madore B. *Magn Reson Med*, 2020, 83: 2310–2321
101 Ma D, Gulani V, Seiberlich N, Liu K, Sunshine JL, Duerk JL, Griswold MA. *Nature*, 2013, 495: 187–192
102 Panda A, Mehta BB, Coppo S, Jiang Y, Ma D, Seiberlich N, Griswold MA, Gulani V. *Curr Opin Biomed Eng*, 2017, 3: 56–66
103 Hsieh JJL, Svalbe I. *J Med Radiat Sci*, 2020, 67: 333–344
104 Mazor G, Weizman L, Tal A, Eldar YC. *Med Phys*, 2018, 45: 4066–4084
105 Zhao B, Setsompop K, Ye H, Cauley SF, Wald LL. *IEEE Trans Med Imag*, 2016, 35: 1812–1823
106 Buonincontri G, Biagi L, Retico A, Cecchi P, Cosottini M, Gallagher FA, Gómez PA, Graves MJ, McLean MA, Riemer F, Schulte RF, Tosetti M, Zaccagna F, Kaggie JD. *NeuroImage*, 2019, 195: 362–372

107 Tang BL. *Biochem Biophysl Res Commun*, 2006, 345: 911–916
108 Vollmer T, Signorovitch J, Huynh L, Galebach P, Kelley C, Di-Bernardo A, Sasane R. *J Neurol Sci*, 2015, 357: 8–18
109 Sanai SA, Saini V, Benedict RH, Zivadinov R, Teter BE, Ramanathan M, Weinstock-Guttman B. *Mult Scler*, 2016, 22: 717–725
110 Giorgio A, De Stefano N. *J Magn Reson Imag*, 2013, 37: 1–14
111 Reiter K, Nielson KA, Durgerian S, Woodard JL, Smith JC, Seidenberg M, Kelly DA, Rao SM. *J Alzheimer Dis*, 2017, 55: 1363–1377
112 Ashburner J, Friston KJ. *Neuroimage*, 2000, 11: 805–821
113 Wetzel SG, Johnson G, Tan AGS, Cha S, Knopp EA, Lee VS, Thomasson D, Rofsky NM. *Am J Neuroradiol*, 1962, 23: 995–1002
114 Whitwell JL. *J Neurosci*, 2009, 29: 9661–9664
115 Ashburner J. *NeuroImage*, 2012, 62: 791–800
116 Ashburner J. *Magn Reson Imag*, 2009, 27: 1163–1174
117 Jenkinson M, Beckmann CF, Behrens TEJ, Woolrich MW, Smith SM. *NeuroImage*, 2012, 62: 782–790
118 Avants BB, Tustison N, Song G. *Insight J*, 2009, 2: 1–35
119 Fischl B. *Neuroimage*, 2012, 62: 774–781
120 Manjón JV, Coupé P. *Front Neuroinf*, 2016, 10: 30
121 Ramzan F, Khan MUG, Iqbal S, Saba T, Rehman A. *IEEE Access*, 2020, 8: 103697–103709
122 Wang L, Xie C, Zeng N. *IEEE Access*, 2019, 7: 39670–39679
123 Bernal J, Kushibar K, Asfaw DS, Valverde S, Oliver A, Martí R, Lladó X. *Artif Intell Med*, 2019, 95: 64–81
124 Risacher SL, Anderson WH, Charil A, Castelluccio PF, Shcherbinin S, Saykin AJ, Schwarz AJ. *Neurology*, 2017, 89: 2176–2186
125 Tsagkas C, Magon S, Gaetano L, Pezold S, Naegelin Y, Amann M, Stippich C, Cattin P, Wuerfel J, Bieri O, Sprenger T, Kappos L, Parmar K. *Neurology*, 2018, 91: e349–e358
126 Qin Y, Wu J, Chen T, Li J, Zhang G, Wu D, Zhou Y, Zheng N, Cai A, Ning Q, Manyande A, Xu F, Wang J, Zhu W. *J Clin Investigation*, 2021, 131: 147329
127 Chen S, Lan Y, Li H, Xia L, Ye C, Lou X, Zhou X. *Biomedicines*, 2022, 10: 781
128 Xue D, Liu Y, Jin L, Wang Y, Cui F, Liu J, Li X, Zhang S, Zhao Y, Yin N, Niu R, Wang D, Zhang H. *Sci China Chem*, 2021, 64: 558–564
129 He W, Ai K, Lu L. *Sci China Chem*, 2015, 58: 753–760
130 Peng XJ, He HP, Liu Q, She K, Zhang BQ, Wang HS, Tang HT, Pan YM. *Sci China Chem*, 2021, 64: 753–760
131 Regenhardt RW, González RG, He J, Lev MH, Singhal AB. *Radiology*, 2022, 302: 400–407
132 Rava RA, Snyder KV, Mokin M, Waqas M, Allman AB, Senko JL, Podgorsak AR, Shiraz Bhurwani MM, Hoi Y, Siddiqui AH, Davies JM, Levy EI, Ionita CN. *AJNR Am J Neuroradiol*, 2020, 41: 206–212
133 Konno Y, Hiraka T, Kanoto M, Sato T, Tsunoda M, Ishizawa T, Matsuda A, Makino N. *Pancreatology*, 2020, 20: 1406–1412
134 He J, Yang Y, Wang Y, Zeng D, Bian Z, Zhang H, Sun J, Xu Z, Ma J. *IEEE Trans Med Imag*, 2018, 38: 371–382
135 Siegler JE, Rosenberg J, Cristancho D, Olsen A, Pulst-Korenberg J, Raab L, Cucchiara B, Messé SR. *Int J Stroke*, 2020, 15: 299–307
136 Li Y. *Sci China Chem*, 2013, 56: 1682–1692
137 Liu CY, Jiang SD. *Sci China Ser B-Chem*, 2009, 52: 2195–2199
138 Maurer GD, Brucker DP, Stoffels G, Filipski K, Filss CP, Mottaghy FM, Galldiks N, Steinbach JP, Hattingen E, Langen KJ. *J Nucl Med*, 2020, 61: 505–511
139 Kim D, Chun JH, Yi JH, Ko HY, Chung JI, Lee M, Park YM, Nam MH, Kim J, Kim SY, Park Y, Moon JH, Kang SG, Chang JH, Lee CJ, Kim SH, Yun M. *Clin Nucl Med*, 2022, 47: 863–868
140 Li A, Gong H, Zhang B, Wang Q, Yan C, Wu J, Liu Q, Zeng S, Luo Q. *Science*, 2010, 330: 1404–1408
141 Ding W, Li A, Wu J, Yang Z, Meng Y, Wang S, Gong H. *J Microsc*, 2013, 251: 168–177
142 Wu J, He Y, Yang Z, Guo C, Luo Q, Zhou W, Chen S, Li A, Xiong B, Jiang T, Gong H. *NeuroImage*, 2014, 87: 199–208
143 Zhang X, Yin X, Zhang J, Li A, Gong H, Luo Q, Zhang H, Gao Z, Jiang H. *Natl Sci Rev*, 2019, 6: 1223–1238
144 Xiong B, Li A, Lou Y, Chen S, Long B, Peng J, Yang Z, Xu T, Yang X, Li X, Jiang T, Luo Q, Gong H. *Front Neuroanat*, 2017, 11: 128
145 Yin X, Zhang X, Zhang J, Yang W, Sun X, Zhang H, Gao Z, Jiang H. *Front Neurosci*, 2022, 16: 870520
146 Xue S, Gong H, Jiang T, Luo W, Meng Y, Liu Q, Chen S, Li A. *PLoS ONE*, 2014, 9: e88067
147 Li Y, Li N, Yu X, Huang K, Zheng T, Cheng X, Zeng S, Liu X. *Sci Rep*, 2018, 8: 1086
148 Huisken J, Swoger J, Del Bene F, Wittbrodt J, Stelzer EHK. *Science*, 2004, 305: 1007–1009
149 Keller PJ, Schmidt AD, Wittbrodt J, Stelzer EHK. *Science*, 2008, 322: 1065–1069
150 Stelzer EHK. *Nat Methods*, 2015, 12: 23–26
151 Power RM, Huisken J. *Nat Methods*, 2017, 14: 360–373
152 Planchon TA, Gao L, Milkie DE, Davidson MW, Galbraith JA, Galbraith CG, Betzig E. *Nat Methods*, 2011, 8: 417–423
153 Chen BC, Legant WR, Wang K, Shao L, Milkie DE, Davidson MW, Janetopoulos C, Wu XS, Hammer Iii JA, Liu Z, English BP, Mimori-Kiyosue Y, Romero DP, Ritter AT, Lippincott-Schwartz J, Fritz-Laylin L, Mullins RD, Mitchell DM, Bembenek JN, Reymann AC, Böhme R, Grill SW, Wang JT, Seydoux G, Tulu US, Kiehart DP, Betzig E. *Science*, 2014, 346: 1257998
154 Vaadia RD, Li W, Voleti V, Singhania A, Hillman EMC, Grueber WB. *Curr Biol*, 2019, 29: 935–944.e4
155 Ueda HR, Ertürk A, Chung K, Gradinaru V, Chédotal A, Tomancak P, Keller PJ. *Nat Rev Neurosci*, 2020, 21: 298
156 Zhao S, Todorov MI, Cai R, -Maskari RA, Steinke H, Kemter E, Mai H, Rong Z, Warmer M, Stanic K, Schoppe O, Paetzold JC, Gesierich B, Wong MN, Huber TB, Duering M, Bruns OT, Menze B, Lipfert J, Puelles VG, Wolf E, Bechmann I, Ertürk A. *Cell*, 2020, 180: 796–812.e19
157 Dodt HU, Leischner U, Schierloh A, Jährling N, Mauch CP, Deininger K, Deussing JM, Eder M, Zieglgänsberger W, Becker K. *Nat Methods*, 2007, 4: 331–336
158 Murakami TC, Mano T, Saikawa S, Horiguchi SA, Shigeta D, Baba K, Sekiya H, Shimizu Y, Tanaka KF, Kiyonari H, Iino M, Mochizuki H, Tainaka K, Ueda HR. *Nat Neurosci*, 2018, 21: 625–637
159 Renier N, Adams EL, Kirst C, Wu Z, Azevedo R, Kohl J, Autry AE, Kadiri L, Umadevi Venkataraju K, Zhou Y, Wang VX, Tang CY, Olsen O, Dulac C, Osten P, Tessier-Lavigne M. *Cell*, 2016, 165: 1789–1802
160 Park YG, Sohn CH, Chen R, McCue M, Yun DH, Drummond GT, Ku T, Evans NB, Oak HC, Trieu W, Choi H, Jin X, Lilascharoen V, Wang J, Truttmann MC, Qi HW, Ploegh HL, Golub TR, Chen SC, Frosch MP, Kulik HJ, Lim BK, Chung K. *Nat Biotechnol*, 2019, 37: 73–83
161 Chen F, Tillberg PW, Boyden ES. *Science*, 2015, 347: 543–548
162 Ku T, Swaney J, Park JY, Albanese A, Murray E, Cho JH, Park YG, Mangena V, Chen J, Chung K. *Nat Biotechnol*, 2016, 34: 973–981
163 Gao R, Asano SM, Upadhyayula S, Pisarev I, Milkie DE, Liu TL, Singh V, Graves A, Huynh GH, Zhao Y, Bogovic J, Colonell J, Ott CM, Zugates C, Tappan S, Rodriguez A, Mosaliganti KR, Sheu SH, Pasolli HA, Pang S, Xu CS, Megason SG, Hess H, Lippincott-Schwartz J, Hantman A, Rubin GM, Kirchhausen T, Saalfeld S, Aso Y, Boyden ES, Betzig E. *Science*, 2019, 363: eaau8302
164 Voigt FF, Kirschenbaum D, Platonova E, Pagès S, Campbell RAA, Kastli R, Schaettin M, Egolf L, van der Bourg A, Bethge P, Haenraets K, Frézel N, Topilko T, Perin P, Hillier D, Hildebrand S, Schueth A, Roebroeck A, Roska B, Stoeckli ET, Pizzala R, Renier N, Zeilhofer HU, Karayannis T, Ziegler U, Batti L, Holtmaat A, Lüscher C, Aguzzi A, Helmchen F. *Nat Methods*, 2019, 16: 1105–1108
165 Todorov MI, Paetzold JC, Schoppe O, Tetteh G, Shit S, Efremov V, Todorov-Völgyi K, Düring M, Dichgans M, Piraud M, Menze B, Ertürk A. *Nat Methods*, 2020, 17: 442–449
166 Hillman EMC, Voleti V, Li W, Yu H. *Annu Rev Neurosci*, 2019, 42: 295–313

167 Mostany R, Miquelajauregui A, Shtrahman M, Portera-Cailliau C. Two-photon excitation microscopy and its applications in neuroscience. In: Verveer P. Ed. *Advanced Fluorescence Microscopy*. *Methods in Molecular Biology*. Vol 1251. New York: Humana Press, 1975
168 Truong TV, Supatto W, Koos DS, Choi JM, Fraser SE. *Nat Methods*, 2011, 8: 757–760
169 Wolf S, Supatto W, Debrégeas G, Mahou P, Kruglik SG, Sintes JM, Beaurepaire E, Candelier R. *Nat Methods*, 2015, 12: 379–380
170 Zong W, Zhao J, Chen X, Lin Y, Ren H, Zhang Y, Fan M, Zhou Z, Cheng H, Sun Y, Chen L. *Cell Res*, 2015, 25: 254–257
171 Lin PY, Hwang SPL, Lee CH, Chen BC. *J Biomed Opt*, 2021, 26: 116503
172 Takanezawa S, Saitou T, Imamura T. *Nat Commun*, 2021, 12: 1–5
173 de Vito G, Turrini L, Müllenbroich C, Ricci P, Sancataldo G, Mazzamuto G, Tiso N, Sacconi L, Fanelli D, Silvestri L, Vanzi F, Pavone FS. *Biomed Opt Express*, 2022, 13: 1516–1536
174 Gasparoli FM, Escobet-Montalbán A, Early J, Bruce GD, Dholakia K. *OSA Continuum*, 2020, 3: 2935–2942
175 Voleti V, Patel KB, Li W, Perez Campos C, Bharadwaj S, Yu H, Ford C, Casper MJ, Yan RW, Liang W, Wen C, Kimura KD, Targoff KL, Hillman EMC. *Nat Methods*, 2019, 16: 1054–1062
176 Yang B, Chen X, Wang Y, Feng S, Pessino V, Stuurman N, Cho NH, Cheng KW, Lord SJ, Xu L, Xie D, Mullins RD, Leonetti MD, Huang B. *Nat Methods*, 2019, 16: 501–504
177 Sapoznik E, Chang BJ, Huh J, Ju RJ, Azarova EV, Pohlkamp T, Welf ES, Broadbent D, Carisey AF, Stehbens SJ, Lee KM, Marín A, Hanker AB, Schmidt JC, Arteaga CL, Yang B, Kobayashi Y, Tata PR, Kruithoff R, Doubrovinski K, Shepherd DP, Millett-Sikking A, York AG, Dean KM, Fiolka RP. *eLife*, 2020, 9: e57681
178 Patel KB, Liang W, Casper MJ, Voleti V, Li W, Yagielski AJ, Zhao HT, Perez Campos C, Lee GS, Liu JM, Philipone E, Yoon AJ, Olive KP, Coley SM, Hillman EMC. *Nat Biomed Eng*, 2022, 6: 569–583
179 Yang B, Lange M, Millett-Sikking A, Zhao X, Bragantini J, Vijay-Kumar S, Kamb M, Gómez-Sjöberg R, Solak AC, Wang W, Kobayashi H, McCarroll MN, Whitehead LW, Fiolka RP, Kornberg TB, York AG, Royer LA. *Nat Methods*, 2022, 19: 461–469
180 Malkinson G, Mahou P, Chaudan É, Gacoin T, Sonay AY, Pantazis P, Beaurepaire E, Supatto W. *ACS Photonics*, 2020, 7: 1036–1049
181 Zhou B, Shi B, Jin D, Liu X. *Nat Nanotech*, 2015, 10: 924–936
182 Richardson DS, Lichtman JW. *Cell*, 2015, 162: 246–257
183 Royer LA, Lemon WC, Chhetri RK, Wan Y, Coleman M, Myers EW, Keller PJ. *Nat Biotechnol*, 2016, 34: 1267–1278
184 Ji N. *Nat Methods*, 2017, 14: 374–380
185 Li C, Moatti A, Zhang X, Troy Ghashghaei H, Greenabum A. *Biomed Opt Express*, 2021, 12: 5214–5226
186 Palay S. *Exp Cell Res (Suppl)*, 1958, 5: 275–293
187 Estable C, Reissig M, De Robertis E. *Exp Cell Res*, 1954, 6: 255–262
188 Robertson JD. *Exp Biol Med*, 1953, 82: 219–223
189 Liao M, Cao E, Julius D, Cheng Y. *Nature*, 2013, 504: 107–112
190 Zhang Y, Ye F, Zhang T, Lv S, Zhou L, Du D, Lin H, Guo F, Luo C, Zhu S. *Nature*, 2021, 596: 301–305
191 Liu YT, Tao CL, Lau PM, Zhou ZH, Bi GQ. *Curr Opin Struct Biol*, 2019, 54: 152–160
192 Liu YT, Tao CL, Zhang X, Xia W, Shi DQ, Qi L, Xu C, Sun R, Li XW, Lau PM, Zhou ZH, Bi GQ. *Nat Neurosci*, 2020, 23: 1589–1596
193 Huang S, Xu P, Tan Y, You C, Zhang Y, Jiang Y, Xu HE. *Cell Res*, 2021, 31: 1036–1038
194 Fitzpatrick AWP, Falcon B, He S, Murzin AG, Murshudov G, Garringer HJ, Crowther RA, Ghetti B, Goedert M, Scheres SHW. *Nature*, 2017, 547: 185–190
195 Nakane T, Kotecha A, Sente A, McMullan G, Masiulis S, Brown PMGE, Grigoras IT, Malinauskaite L, Malinauskas T, Miehling J, Uchański T, Yu L, Karia D, Pechnikova EV, de Jong E, Keizer J, Bischoff M, McCormack J, Tiemeijer P, Hardwick SW, Chirgadze DY, Murshudov G, Aricescu AR, Scheres SHW. *Nature*, 2020, 587: 152–156
196 Trinkaus VA, Riera-Tur I, Martínez-Sánchez A, Bäuerlein FJB, Guo Q, Arzberger T, Baumeister W, Dudanova I, Hipp MS, Hartl FU, Fernández-Busnadiego R. *Nat Commun*, 2021, 12: 1
197 Guo Q, Lehmer C, Martínez-Sánchez A, Rudack T, Beck F, Hartmann H, Pérez-Berlanga M, Frottin F, Hipp MS, Hartl FU, Edbauer D, Baumeister W, Fernández-Busnadiego R. *Cell*, 2018, 172: 696–705.e12
198 Tao CL, Liu YT, Zhou ZH, Lau PM, Bi GQ. *Front Neuroanat*, 2018, 12: 48
199 Tao CL, Liu YT, Sun R, Zhang B, Qi L, Shivakoti S, Tian CL, Zhang P, Lau PM, Zhou ZH, Bi GQ. *J Neurosci*, 2018, 38: 1493–1510
200 Radhakrishnan A, Li X, Grushin K, Krishnakumar SS, Liu J, Rothman JE. *Proc Natl Acad Sci USA*, 2021, 118: e2024029118
201 Sun R, Liu YT, Tao CL, Qi L, Lau PM, Zhou ZH, Bi GQ. *Biophys Rep*, 2019, 5: 111–122
202 Schaffer M, Mahamid J, Engel BD, Laugks T, Baumeister W, Plitzko JM. *J Struct Biol*, 2017, 197: 73–82
203 White JG, Southgate E, Thomson JN, Brenner S. *Phil Trans R Soc Lond B*, 1986, 314: 1–340
204 Shapson-Coe A, Januszewski M, Berger DR, Pope A, Wu Y, Blakely T, Schalek RL, Li PH, Wang S, Maitin-Shepard J. *BioRxiv*, 2021, doi: 10.1101/2021.05.29.446289
205 Scholl B, Thomas CI, Ryan MA, Kamasawa N, Fitzpatrick D. *Nature*, 2021, 590: 111–114
206 Henstridge M, Pfeiffer C, Wang D, Boltasseva A, Shalaev VM, Grbic A, Merlin R. *Science*, 2018, 362: 439–442
207 Hwu Y, Margaritondo G, Chiang A-S. *BMC Biol*, 2017, 15: 1–9
208 Töpperwien M, van der Meer F, Stadelmann C, Salditt T. *Proc Natl Acad Sci USA*, 2018, 115: 6940–6945
209 Foxley S, Sampathkumar V, De Andrade V, Trinkle S, Sorokina A, Norwood K, La Riviere P, Kasthuri N. *NeuroImage*, 2021, 238: 118250
210 Withers PJ, Bouman C, Carmignato S, Cnudde V, Grimaldi D, Hagen CK, Maire E, Manley M, Du Plessis A, Stock SR. *Nat Rev Methods Primers*, 2021, 1: 1–2
211 Sanchez-Cano C, Alvarez-Puebla RA, Abendroth JM, Beck T, Blick R, Cao Y, Caruso F, Chakraborty I, Chapman HN, Chen C, Cohen BE, Conceição ALC, Cormode DP, Cui D, Dawson KA, Falkenberg G, Fan C, Feliu N, Gao M, Gargioni E, Glüer CC, Grüner F, Hassan M, Hu Y, Huang Y, Huber S, Huse N, Kang Y, Khademhosseini A, Keller TF, Körnig C, Kotov NA, Koziej D, Liang XJ, Liu B, Liu S, Liu Y, Liu Z, Liz-Marzán LM, Ma X, Machicote A, Maison W, Mancuso AP, Megahed S, Nickel B, Otto F, Palencia C, Pascarelli S, Pearson A, Peñate-Medina O, Qi B, Rädler J, Richardson JJ, Rosenhahn A, Rothkamm K, Rübhausen M, Sanyal MK, Schaak RE, Schlemmer HP, Schmidt M, Schmutzler O, Schotten T, Schulz F, Sood AK, Spiers KM, Staufer T, Stemer DM, Stierle A, Sun X, Tsakanova G, Weiss PS, Weller H, Westermeier F, Xu M, Yan H, Zeng Y, Zhao Y, Zhao Y, Zhu D, Zhu Y, Parak WJ. *ACS Nano*, 2021, 15: 3754–3807
212 Andreasen NC. *Science*, 1988, 239: 1381–1388
213 Lv J, Di Biase M, Cash RFH, Cocchi L, Cropley VL, Klauser P, Tian Y, Bayer J, Schmaal L, Cetin-Karayumak S, Rathi Y, Pasternak O, Bousman C, Pantelis C, Calamante F, Zalesky A. *Mol Psychiatry*, 2021, 26: 3512–3523
214 Bosch C, Ackels T, Pacureanu A, Zhang Y, Peddie CJ, Berning M, Rzepka N, Zdora MC, Whiteley I, Storm M, Bonnin A, Rau C, Margrie T, Collinson L, Schaefer AT. *Nat Commun*, 2022, 13: 1–6
215 Kong H, Li M, Xu Q, Zhou H, Yu F, Wang Q. *Am J Nucl Med Mol Imaging*, 2021, 11: 529–536
216 Brooks J, Everett J, Lermyte F, Tjhin VT, Banerjee S, O'Connor PB, Morris CM, Sadler PJ, Telling ND, Collingwood JF. *Angew Chem Int Ed*, 2020, 59: 11984–11991
217 Kong H, Zhang J, Li J, Wang J, Shin HJ, Tai R, Yan Q, Xia K, Hu J, Wang L, Zhu Y, Fan C. *Natl Sci Rev*, 2020, 7: 1218–1227
218 Si-Mohamed S, Tatard-Leitman V, Laugerette A, Sigovan M, Pfeiffer D, Rummeny EJ, Coulon P, Yagil Y, Douek P, Boussel L,

Noël PB. *Sci Rep*, 2019, 9: 1–8
219 McCollough CH, Leng S, Yu L, Fletcher JG. *Radiology*, 2015, 276: 637–653
220 Fratini M, Bukreeva I, Campi G, Brun F, Tromba G, Modregger P, Bucci D, Battaglia G, Spanò R, Mastrogiacomo M, Requardt H, Giove F, Bravin A, Cedola A. *Sci Rep*, 2015, 5: 8514
221 Hu J, Li P, Yin X, Wu T, Cao Y, Yang Z, Jiang L, Hu S, Lu H. *J Synchrotron Rad*, 2017, 24: 482–489
222 Cedola A, Bravin A, Bukreeva I, Fratini M, Pacureanu A, Mittone A, Massimi L, Cloetens P, Coan P, Campi G, Spanò R, Brun F, Grigoryev V, Petrosino V, Venturi C, Mastrogiacomo M, Kerlero de Rosbo N, Uccelli A. *Sci Rep*, 2017, 7: 1
223 Bukreeva I, Campi G, Fratini M, Spanò R, Bucci D, Battaglia G, Giove F, Bravin A, Uccelli A, Venturi C, Mastrogiacomo M, Cedola A. *Sci Rep*, 2017, 7: 1
224 Böhm T, Joseph K, Kirsch M, Moroni R, Hilger A, Osenberg M, Manke I, Johnston M, Stieglitz T, Hofmann UG, Haas CA, Thiele S. *Sci Rep*, 2019, 9: 7646
225 Khimchenko A, Schulz G, Thalmann P, Müller B. *APL Bioeng*, 2018, 2: 016106
226 Bikis C, Rodgers G, Deyhle H, Thalmann P, Hipp A, Beckmann F, Weitkamp T, Theocharis S, Rau C, Schulz G, Müller B. *Appl Phys Lett*, 2019, 114: 083702
227 Hubert M, Pacureanu A, Guilloud C, Yang Y, da Silva JC, Laurencin J, Lefebvre-Joud F, Cloetens P. *Appl Phys Lett*, 2018, 112: 203704
228 Khimchenko A, Bikis C, Pacureanu A, Hieber SE, Thalmann P, Deyhle H, Schweighauser G, Hench J, Frank S, Müller-Gerbl M, Schulz G, Cloetens P, Müller B. *Adv Sci*, 2018, 5: 1700694
229 Khimchenko A, Pacureanu A, Bikis C, Hieber SE, Thalmann P, Deyhle H, Schweighauser G, Hench J, Frank S, Muller-Gerbl M, Schulz G, Cloetens P, Muller B. *Microsc Microanal*, 2018, 24: 354–355
230 Kuan AT, Phelps JS, Thomas LA, Nguyen TM, Han J, Chen CL, Azevedo AW, Tuthill JC, Funke J, Cloetens P, Pacureanu A, Lee WCA. *Nat Neurosci*, 2020, 23: 1637–1643
231 Hill AV. *Nature*, 1929, 123: 9–11
232 Hubel DH, Wiesel TN. *J Physiol*, 1959, 148: 574–591
233 Hamill OP, Marty A, Neher E, Sakmann B, Sigworth FJ. *Pflügers Archiv*, 1981, 391: 85–100
234 Zhang C, Liu JQ, Tian HC, Kang XY, Du JC, Rui YF, Yang B, Yang CS. *Microsyst Technol*, 2015, 21: 139–145
235 Wang K, Chung-Chiun Liu K, Durand DM. *IEEE Trans Biomed Eng*, 2009, 56: 6–14
236 Brüggemann D, Wolfrum B, Maybeck V, Mourzina Y, Jansen M, Offenhäusser A. *Nanotechnology*, 2011, 22: 265104
237 Kim JH, Kang G, Nam Y, Choi YK. *Nanotechnology*, 2010, 21: 085303
238 Khodagholy D, Doublet T, Gurfinkel M, Quilichini P, Ismailova E, Leleux P, Herve T, Sanaur S, Bernard C, Malliaras GG. *Adv Mater*, 2011, 23: H268–H272
239 Blau A, Murr A, Wolff S, Sernagor E, Medini P, Iurilli G, Ziegler C, Benfenati F. *Biomaterials*, 2011, 32: 1778–1786
240 Ansaldo A, Castagnola E, Maggiolini E, Fadiga L, Ricci D. *ACS Nano*, 2011, 5: 2206–2214
241 Keefer EW, Botterman BR, Romero MI, Rossi AF, Gross GW. *Nat Nanotech*, 2008, 3: 434–439
242 Chung JE, Joo HR, Fan JL, Liu DF, Barnett AH, Chen S, Geaghan-Breiner C, Karlsson MP, Karlsson M, Lee KY, Liang H, Magland JF, Pebbles JA, Tooker AC, Greengard LF, Tolosa VM, Frank LM. *Neuron*, 2019, 101: 21–31.e5
243 Dipalo M, Rastogi SK, Matino L, Garg R, Bliley J, Iachetta G, Melle G, Shrestha R, Shen S, Santoro F, Feinberg AW, Barbaglia A, Cohen-Karni T, De Angelis F. *Sci Adv*, 2021, 7: eabd5175
244 Khodagholy D, Doublet T, Quilichini P, Gurfinkel M, Leleux P, Ghestem A, Ismailova E, Hervé T, Sanaur S, Bernard C, Malliaras GG. *Nat Commun*, 2013, 4: 1575
245 Salatino JW, Ludwig KA, Kozai TDY, Purcell EK. *Nat Biomed Eng*, 2017, 1: 862–877
246 Feiner R, Dvir T. *Nat Rev Mater*, 2018, 3: 17076
247 Musk E. *J Med Internet Res*, 2019, 21: e16194
248 Khodagholy D, Gelinas JN, Thesen T, Doyle W, Devinsky O, Malliaras GG, Buzsáki G. *Nat Neurosci*, 2015, 18: 310–315
249 Fu TM, Hong G, Zhou T, Schuhmann TG, Viveros RD, Lieber CM. *Nat Methods*, 2016, 13: 875–882
250 Lee W, Kim D, Matsuhisa N, Nagase M, Sekino M, Malliaras GG, Yokota T, Someya T. *Proc Natl Acad Sci USA*, 2017, 114: 10554–10559
251 Lee J, Ozden I, Song YK, Nurmikko AV. *Nat Methods*, 2015, 12: 1157–1162
252 Park S, Guo Y, Jia X, Choe HK, Grena B, Kang J, Park J, Lu C, Canales A, Chen R, Yim YS, Choi GB, Fink Y, Anikeeva P. *Nat Neurosci*, 2017, 20: 612–619
253 Zhang Y, Zheng N, Cao Y, Wang F, Wang P, Ma Y, Lu B, Hou G, Fang Z, Liang Z, Yue M, Li Y, Chen Y, Fu J, Wu J, Xie T, Feng X. *Sci Adv*, 2019, 5: eaaw1066
254 Wu F, Stark E, Ku PC, Wise KD, Buzsáki G, Yoon E. *Neuron*, 2015, 88: 1136–1148
255 Minev IR, Musienko P, Hirsch A, Barraud Q, Wenger N, Moraud EM, Gandar J, Capogrosso M, Milekovic T, Asboth L, Torres RF, Vachicouras N, Liu Q, Pavlova N, Duis S, Larmagnac A, Vörös J, Micera S, Suo Z, Courtine G, Lacour SP. *Science*, 2015, 347: 159–163
256 Shin H, Son Y, Chae U, Kim J, Choi N, Lee HJ, Woo J, Cho Y, Yang SH, Lee CJ, Cho IJ. *Nat Commun*, 2019, 10: 3777
257 Hodgkin AL, Huxley AF. *Nature*, 1939, 144: 710–711
258 Cole KS, Curtis HJ. *J Gen Physiol*, 1939, 22: 649–670
259 Cole K. *Arch Sci Physiol*, 1949, 3: 253–258
260 Marmont G. *J Cell Comp Physiol*, 1949, 34: 351–382
261 Hodgkin AL, Huxley AF. *J Physiol*, 1952, 116: 449–472
262 Neher E, Sakmann B. *Nature*, 1976, 260: 799–802
263 Peier AM, Moqrich A, Hergarden AC, Reeve AJ, Andersson DA, Story GM, Earley TJ, Dragoni I, McIntyre P, Bevan S, Patapoutian A. *Cell*, 2002, 108: 705–715
264 Noma A. *Nature*, 1983, 305: 147–148
265 Nowak L, Bregestovski P, Ascher P, Herbet A, Prochiantz A. *Nature*, 1984, 307: 462–465
266 Song E, Lee YK, Li R, Li J, Jin X, Yu KJ, Xie Z, Fang H, Zhong Y, Du H, Zhang J, Fang G, Kim Y, Yoon Y, Alam MA, Mei Y, Huang Y, Rogers JA. *Adv Funct Mater*, 2018, 28: 1702284
267 Buzsáki G, Anastassiou CA, Koch C. *Nat Rev Neurosci*, 2012, 13: 407–420
268 Cohen MX. *Trends Neuroscis*, 2017, 40: 208–218
269 Pravdich-Neminsky V. *Zbl Physiol*, 1913, 27: 951–960
270 Berger H. *Archiv für Psychiatrie und Nervenkrankheiten*, 1929, 87: 527–570
271 Adrian ED, Matthews BHC. *Brain*, 1934, 57: 355–385
272 Adrian ED, Yamagiwa K. *Brain*, 1935, 58: 323–351
273 Jasper H. *Electroen Clin Neuro*, 1958, 10: 370–375
274 Petrov Y, Nador J, Hughes C, Tran S, Yavuzcetin O, Sridhar S. *Neuroimage*, 2014, 90: 140–145
275 Tucker DM. *Electroencephalogr Clin Neurophysiol*, 1993, 87: 154–163
276 Hämäläinen M, Hari R, Ilmoniemi RJ, Knuutila J, Lounasmaa OV. *Rev Mod Phys*, 1993, 65: 413–497
277 He B, Sohrabpour A, Brown E, Liu Z. *Annu Rev Biomed Eng*, 2018, 20: 171–196
278 Dehghani N, Bédard C, Cash SS, Halgren E, Destexhe A. *J Comput Neurosci*, 2010, 29: 405–421
279 Ahlfors SP. *Magnetoencephalography: From Signals to Dynamic Cortical Networks*. 2nd Ed. Cham: Springer, 2019. 259–278
280 Stefan H, Nakasato N, Papanicolaou AC. *Handb Clin Neurol*, 2012, 107: 347–358
281 Palmini ALF. *Epileptic Disorders*, 2006, 8: S10–S15
282 Kuruvilla A, Flink R. *Seizure*, 2003, 12: 577–584

283 Bazhenov M, Lonjers P, Skorheim S, Bedard C, Destexhe A. *Phil Trans R Soc A*, 2011, 369: 3802–3819
284 Hong G, Lieber CM. *Nat Rev Neurosci*, 2019, 20: 330–345
285 Rossant C, Kadir SN, Goodman DFM, Schulman J, Hunter MLD, Saleem AB, Grosmark A, Belluscio M, Denfield GH, Ecker AS, Tolias AS, Solomon S, Buzsaki G, Carandini M, Harris KD. *Nat Neurosci*, 2016, 19: 634–641
286 Mishanina TV, Libiad M, Banerjee R. *Nat Chem Biol*, 2015, 11: 457–464
287 Kimura H. *Proc Jpn Acad Ser B-Phys Biol Sci*, 2015, 91: 131–159
288 Greiner R, Pálinkás Z, Bäsell K, Becher D, Antelmann H, Nagy P, Dick TP. *Antioxid Redox Signal*, 2013, 19: 1749–1765
289 Yadav PK, Martinov M, Vitvitsky V, Seravalli J, Wedmann R, Filipovic MR, Banerjee R. *J Am Chem Soc*, 2016, 138: 289–299
290 Tan BH, Wong PTH, Bian JS. *Neurochem Int*, 2010, 56: 3–10
291 Elrod JW, Calvert JW, Morrison J, Doeller JE, Kraus DW, Tao L, Jiao X, Scalia R, Kiss L, Szabo C, Kimura H, Chow CW, Lefer DJ. *Proc Natl Acad Sci USA*, 2007, 104: 15560–15565
292 Hu B, Kong F, Gao X, Jiang L, Li X, Gao W, Xu K, Tang B. *Angew Chem Int Ed*, 2018, 57: 5306–5309
293 Gao P, Wang M, Wan X, Liu X, Pan W, Li N, Tang B. *Chem Commun*, 2020, 56: 14267–14270
294 Soto RJ, Hall JR, Brown MD, Taylor JB, Schoenfisch MH. *Anal Chem*, 2017, 89: 276–299
295 Liu X, Zhang M, Xiao T, Hao J, Li R, Mao L. *Anal Chem*, 2016, 88: 7238–7244
296 Liu X, Xiao T, Wu F, Shen MY, Zhang M, Yu HH, Mao L. *Angew Chem Int Ed*, 2017, 56: 11802–11806
297 Li X, Ren L, Dunevall J, Ye D, White HS, Edwards MA, Ewing AG. *ACS Nano*, 2018, 12: 3010–3019
298 Wang X, Chan HN, Desbois N, Gros CP, Bolze F, Li Y, Li HW, Wong MS. *ACS Appl Mater Interfaces*, 2021, 13: 18525–18532
299 Robert P, Vives V, Grindel AL, Kremer S, Bierry G, Louin G, Ballet S, Corot C. *Radiology*, 2020, 294: 117–126
300 Wahsner J, Gale EM, Rodríguez-Rodríguez A, Caravan P. *Chem Rev*, 2018, 119: 957–1057
301 D′Arceuil H, Coimbra A, Triano P, Dougherty M, Mello J, Moseley M, Glover G, Lansberg M, Blankenberg F. *NeuroImage*, 2013, 83: 200–209
302 Iv M, Ng NN, Nair S, Zhang Y, Lavezo J, Cheshier SH, Holdsworth SJ, Moseley ME, Rosenberg J, Grant GA, Yeom KW. *Radiology*, 2020, 297: 438–446
303 Calvete MJF, Pinto SMA, Pereira MM, Geraldes CFGC. *Coord Chem Rev*, 2017, 333: 82–107
304 Lenora CU, Carniato F, Shen Y, Latif Z, Haacke EM, Martin PD, Botta M, Allen MJ. *Chem Eur J*, 2017, 23: 15404–15414
305 Morelli JN, Runge VM, Williams JM, Beissner RS, Tweedle M. *Investig Radiol*, 2011, 46: 169–177
306 Sillerud LO, Solberg NO, Chamberlain R, Orlando RA, Heidrich JE, Brown DC, Brady CI, Vander Jagt TA, Garwood M, Vander Jagt DL. *J Alzheimer Dis*, 2013, 34: 349–365
307 Cheng Y, Cheng A, Jia Y, Yang L, Ning Y, Xu L, Zhong Y, Zhuang Z, Guan J, Zhang X, Lin Y, Zhou T, Fan X, Li J, Liu P, Yan G, Wu R. *ACS Appl Mater Interfaces*, 2021, 13: 56909–56922
308 Barandov A, Bartelle BB, Williamson CG, Loucks ES, Lippard SJ, Jasanoff A. *Nat Commun*, 2019, 10: 1–9
309 Novotna B, Herynek V, Rossner P, Turnovcova K, Jendelova P. *Int J Nanomed*, 2017, Volume 12: 4519–4526
310 Lee T, Cai LX, Lelyveld VS, Hai A, Jasanoff A. *Science*, 2014, 344: 533–535
311 Grist JT, McLean MA, Riemer F, Schulte RF, Deen SS, Zaccagna F, Woitek R, Daniels CJ, Kaggie JD, Matys T, Patterson I, Slough R, Gill AB, Chhabra A, Eichenberger R, Laurent MC, Comment A, Gillard JH, Coles AJ, Tyler DJ, Wilkinson I, Basu B, Lomas DJ, Graves MJ, Brindle KM, Gallagher FA. *NeuroImage*, 2019, 189: 171–179
312 Lee CY, Soliman H, Geraghty BJ, Chen AP, Connelly KA, Endre R, Perks WJ, Heyn C, Black SE, Cunningham CH. *Neuroimage*, 2020, 204: 116202
313 Yuan Y, Guo Q, Zhang X, Jiang W, Ye C, Zhou X. *J Mater Chem B*, 2020, 8: 5014–5018
314 Li H, Zhao X, Wang Y, Lou X, Chen S, Deng H, Shi L, Xie J, Tang D, Zhao J, Bouchard LS, Xia L, Zhou X. *Sci Adv*, 2021, 7: eabc8180
315 Witte C, Martos V, Rose HM, Reinke S, Klippel S, Schröder L, Hackenberger CPR. *Angew Chem Int Ed*, 2015, 54: 2806–2810
316 Yanagisawa D, Ibrahim NF, Taguchi H, Morikawa S, Tomiyama T, Tooyama I. *Molecules*, 2021, 26: 1362
317 Li S, Jiang W, Yuan Y, Sui M, Yang Y, Huang L, Jiang L, Liu M, Chen S, Zhou X. *ACS Appl Mater Interfaces*, 2020, 12: 57290–57301
318 Walker-Samuel S, Ramasawmy R, Torrealdea F, Rega M, Rajkumar V, Johnson SP, Richardson S, Gonçalves M, Parkes HG, Arstad E, Thomas DL, Pedley RB, Lythgoe MF, Golay X. *Nat Med*, 2013, 19: 1067–1072
319 Longo DL, Sun PZ, Consolino L, Michelotti FC, Uggeri F, Aime S. *J Am Chem Soc*, 2014, 136: 14333–14336
320 Branzoli F, Pontoizeau C, Tchara L, Di Stefano AL, Kamoun A, Deelchand DK, Valabrègue R, Lehéricy S, Sanson M, Ottolenghi C, Marjańska M. *Neuro-Oncology*, 2019, 21: 765–774
321 Okada S, Bartelle BB, Li N, Breton-Provencher V, Lee JJ, Rodriguez E, Melican J, Sur M, Jasanoff A. *Nat Nanotech*, 2018, 13: 473–477
322 Choi C, Ganji SK, DeBerardinis RJ, Hatanpaa KJ, Rakheja D, Kovacs Z, Yang XL, Mashimo T, Raisanen JM, Marin-Valencia I, Pascual JM, Madden CJ, Mickey BE, Malloy CR, Bachoo RM, Maher EA. *Nat Med*, 2012, 18: 624–629
323 Andronesi OC, Kim GS, Gerstner E, Batchelor T, Tzika AA, Fantin VR, Vander Heiden MG, Sorensen AG. *Sci Transl Med*, 2012, 4: 116ra114
324 Branzoli F, Deelchand DK, Sanson M, Lehéricy S, Marjańska M. *Magn Reson Med*, 2019, 82: 1259–1265
325 Cuccarini V, Antelmi L, Pollo B, Paterra R, Calatozzolo C, Nigri A, DiMeco F, Eoli M, Finocchiaro G, Brenna G, Tramacere I, Bruzzone MG, Anghileri E. *Neurol Sci*, 2020, 41: 347–355
326 Lei H, Ugurbil K, Chen W. *Proc Natl Acad Sci USA*, 2003, 100: 14409–14414
327 Rijpma A, van der Graaf M, Meulenbroek O, Olde Rikkert MGM, Heerschap A. *Neuroimage-Clin*, 2018, 18: 254–261
328 Rango M, Bonifati C, Bresolin N. *J Cereb Blood Flow Metab*, 2006, 26: 283–290
329 Levine SR, Helpern JA, Welch KM, Vande Linde AM, Sawaya KL, Brown EE, Ramadan NM, Deveshwar RK, Ordidge RJ. *Radiology*, 1992, 185: 537–544
330 Le Page LM, Guglielmetti C, Taglang C, Chaumeil MM. *Trends Neuroscis*, 2020, 43: 343–354
331 Hesketh RL, Brindle KM. *Curr Opin Chem Biol*, 2018, 45: 187–194
332 Miloushev VZ, Granlund KL, Boltyanskiy R, Lyashchenko SK, DeAngelis LM, Mellinghoff IK, Brennan CW, Tabar V, Yang TJ, Holodny AI, Sosa RE, Guo YWW, Chen AP, Tropp J, Robb F, Keshari KR. *Cancer Res*, 2018, 78: 3755–3760
333 Park I, Larson PEZ, Gordon JW, Carvajal L, Chen HY, Bok R, Van Criekinge M, Ferrone M, Slater JB, Xu D, Kurhanewicz J, Vigneron DB, Chang S, Nelson SJ. *Magn Reson Med*, 2018, 80: 864–873
334 Mammoli D, Gordon J, Autry A, Larson PEZ, Li Y, Chen HY, Chung B, Shin P, Van Criekinge M, Carvajal L, Slater JB, Bok R, Crane J, Xu D, Chang S, Vigneron DB. *IEEE Trans Med Imag*, 2019, 39: 320–327
335 Autry AW, Gordon JW, Chen HY, LaFontaine M, Bok R, Van Criekinge M, Slater JB, Carvajal L, Villanueva-Meyer JE, Chang SM, Clarke JL, Lupo JM, Xu D, Larson PEZ, Vigneron DB, Li Y. *Neuroimage-Clin*, 2020, 27: 102323
336 Flogel U, Ding Z, Hardung H, Jander S, Reichmann G, Jacoby C, Schubert R, Schrader J. *Circulation*, 2008, 118: 140–148
337 Chirizzi C, De Battista D, Tirotta I, Metrangolo P, Comi G, Bombelli FB, Chaabane L. *Radiology*, 2019, 291: 351–357
338 Strauss WL, Unis AS, Cowan C, Dawson G, Dager SR. *Am J Psy-*

chiat,, 2002, 159: 755–760
339 Wenger KJ, Richter C, Burger MC, Urban H, Kaulfuss S, Harter PN, Sreeramulu S, Schwalbe H, Steinbach JP, Hattingen E, Bähr O, Pilatus U. *Cancers*, 2020, 12: 3175
340 Prinz C, Starke L, Millward JM, Fillmer A, Delgado PR, Waiczies H, Pohlmann A, Rothe M, Nazaré M, Paul F, Niendorf T, Waiczies S. *Theranostics*, 2021, 11: 2490–2504
341 Kwong KK, Belliveau JW, Chesler DA, Goldberg IE, Weisskoff RM, Poncelet BP, Kennedy DN, Hoppel BE, Cohen MS, Turner R, Cheng HM, Brady TJ, Rosen BR. *Proc Natl Acad Sci USA*, 1992, 89: 5675–5679
342 Ogawa S, Tank DW, Menon R, Ellermann JM, Kim SG, Merkle H, Ugurbil K. *Proc Natl Acad Sci USA*, 1992, 89: 5951–5955
343 Bandettini PA, Wong EC, Hinks RS, Tikofsky RS, Hyde JS. *Magn Reson Med*, 1992, 25: 390–397
344 Qiu D, Zaharchuk G, Christen T, Ni WW, Moseley ME. *Neuroimage*, 2012, 62: 1726–1731
345 Baumgartner R, Cho W, Coimbra A, Chen C, Wang Z, Struyk A, Venketasubramanian N, Low M, Gargano C, Zhao F, Williams D, Reese T, Seah S, Feng D, Apreleva S, Petersen E, Evelhoch JL. *J Magn Reson Imag*, 2017, 46: 124–133
346 Li N, Jasanoff A. *Nature*, 2020, 580: 239–244
347 Bednařík P, Tkáč I, Giove F, DiNuzzo M, Deelchand DK, Emir UE, Eberly LE, Mangia S. *J Cereb Blood Flow Metab*, 2015, 35: 601–610
348 Luo Y, Kim EH, Flask CA, Clark HA. *ACS Nano*, 2018, 12: 5761–5773
349 Savić T, Gambino G, Bokharaie VS, Noori HR, Logothetis NK, Angelovski G. *Proc Natl Acad Sci USA*, 2019, 116: 20666–20671
350 Lee T, Zhang X, Dhar S, Faas H, Lippard SJ, Jasanoff A. *Chem Biol*, 2010, 17: 665–673
351 Ghosh S, Li N, Schwalm M, Bartelle BB, Xie T, Daher JI, Singh UD, Xie K, DiNapoli N, Evans NB, Chung K, Jasanoff A. *Nat Neurosci*, 2022, 25: 390–398
352 Li M, Liu Z, Wu Y, Zheng N, Liu X, Cai A, Zheng D, Zhu J, Wu J, Xu L. *Mol Psychiatry*, 2022, doi: 10.1038/s41380-022-01540-0
353 Davis KA, Nanga RPR, Das S, Chen SH, Hadar PN, Pollard JR, Lucas TH, Shinohara RT, Litt B, Hariharan H, Elliott MA, Detre JA, Reddy R. *Sci Transl Med*, 2015, 7: 309ra161
354 Sun PZ, Cheung JS, Wang E, Lo EH. *J Cereb Blood Flow Metab*, 2011, 31: 1743–1750
355 Zhang X, Yuan Y, Li S, Zeng Q, Guo Q, Liu N, Yang M, Yang Y, Liu M, McMahon MT, Zhou X. *Magn Reson Med*, 2019, 82: 577–585
356 Tiwari V, Daoud EV, Hatanpaa KJ, Gao A, Zhang S, An Z, Ganji SK, Raisanen JM, Lewis CM, Askari P, Baxter J, Levy M, Dimitrov I, Thomas BP, Pinho MC, Madden CJ, Pan E, Patel TR, DeBerardinis RJ, Sherry AD, Mickey BE, Malloy CR, Maher EA, Choi C. *Neuro-Oncology*, 2020, 22: 1018–1029
357 Rao MR, Stewart NJ, Griffiths PD, Norquay G, Wild JM. *Radiology*, 2018, 286: 659–665
358 Zeng Q, Guo Q, Yuan Y, Yang Y, Zhang B, Ren L, Zhang X, Luo Q, Liu M, Bouchard LS, Zhou X. *Anal Chem*, 2017, 89: 2288–2295
359 Zhang B, Guo Q, Luo Q, Zhang X, Zeng QB, Zhao L, Yuan Y, Jiang W, Yang Y, Liu M, Ye C, Zhou X. *Chem Commun*, 2018, 54: 13654–13657
360 Fernando PUAI, Shepelytskyi Y, Cesana PT, Wade A, Grynko V, Mendieta AM, Seveney LE, Brown JD, Hane FT, Albert MS, DeBoef B. *ACS Omega*, 2020, 5: 27783–27788
361 Shapiro MG, Ramirez RM, Sperling LJ, Sun G, Sun J, Pines A, Schaffer DV, Bajaj VS. *Nat Chem*, 2014, 6: 629–634
362 Yang Y, Zhang Y, Wang B, Guo Q, Yuan Y, Jiang W, Shi L, Yang M, Chen S, Lou X, Zhou X. *Chem Sci*, 2021, 12: 4300–4308
363 Zeng Q, Bie B, Guo Q, Yuan Y, Han Q, Han X, Chen M, Zhang X, Yang Y, Liu M, Liu P, Deng H, Zhou X. *Proc Natl Acad Sci USA*, 2020, 117: 17558–17563
364 Jayapaul J, Komulainen S, Zhivonitko VV, Mareš J, Giri C, Rissanen K, Lantto P, Telkki VV, Schröder L. *Nat Commun*, 2022, 13: 1–10
365 Liu Z, Pei H, Zhang L, Tian Y. *ACS Nano*, 2018, 12: 12357–12368
366 Zhang Z, Liu Z, Tian Y. *iScience*, 2020, 23: 101344
367 Zhu A, Qu Q, Shao X, Kong B, Tian Y. *Angew Chem Int Ed*, 2012, 51: 7185–7189
368 Liu Z, Jing X, Zhang S, Tian Y. *Anal Chem*, 2019, 91: 2488–2497
369 Liu Z, Wang S, Li W, Tian Y. *Anal Chem*, 2018, 90: 2816–2825
370 Liang M, Liu Z, Zhang Z, Mei Y, Tian Y. *Chem Sci*, 2022, 13: 4303–4312
371 Wu Z, Liu M, Liu Z, Tian Y. *J Am Chem Soc*, 2020, 142: 7532–7541
372 Mei Y, Zhang QW, Gu Q, Liu Z, He X, Tian Y. *J Am Chem Soc*, 2022, 144: 2351–2359
373 Gong Z, Liu Z, Zhang Z, Mei Y, Tian Y. *CCS Chem*, 2022, 4: 2020–2030
374 Kong B, Zhu A, Ding C, Zhao X, Li B, Tian Y. *Adv Mater*, 2012, 24: 5844–5848
375 Lavis LD, Raines RT. *ACS Chem Biol*, 2008, 3: 142–155
376 Li B, Zhao M, Feng L, Dou C, Ding S, Zhou G, Lu L, Zhang H, Chen F, Li X, Li G, Zhao S, Jiang C, Wang Y, Zhao D, Cheng Y, Zhang F. *Nat Commun*, 2020, 11: 3102
377 Wu J, Shao C, Ye X, Di X, Li D, Zhao H, Zhang B, Chen G, Liu HK, Qian Y. *ACS Sens*, 2021, 6: 863–870
378 Liu S, Chen C, Li Y, Zhang H, Liu J, Wang R, Wong STH, Lam JWY, Ding D, Tang BZ. *Adv Funct Mater*, 2020, 30: 1908125
379 Samanta S, Huang M, Li S, Yang Z, He Y, Gu Z, Zhang J, Zhang D, Liu L, Qu J. *Theranostics*, 2021, 11: 2137–2148
380 Liu Y, Liu J, Chen D, Wang X, Zhang Z, Yang Y, Jiang L, Qi W, Ye Z, He S, Liu Q, Xi L, Zou Y, Wu C. *Angew Chem Int Ed*, 2020, 59: 21049–21057
381 Zhang Z, Fang X, Liu Z, Liu H, Chen D, He S, Zheng J, Yang B, Qin W, Zhang X, Wu C. *Angew Chem Int Ed*, 2020, 59: 3691–3698
382 Liu Y, Lu Y, Chen G, Wang Q. *Biotechnol J*, 2020, 15: 2000086
383 Yan P, Acker CD, Zhou WL, Lee P, Bollensdorff C, Negrean A, Lotti J, Sacconi L, Antic SD, Kohl P, Mansvelder HD, Pavone FS, Loew LM. *Proc Natl Acad Sci USA*, 2012, 109: 20443–20448
384 Treger JS, Priest MF, Iezzi R, Bezanilla F. *Biophysl J*, 2014, 107: L09–L12
385 Zebibula A, Alifu N, Xia L, Sun C, Yu X, Xue D, Liu L, Li G, Qian J. *Adv Funct Mater*, 2018, 28: 1703451
386 Li C, Li W, Liu H, Zhang Y, Chen G, Li Z, Wang Q. *Angew Chem Int Ed*, 2020, 59: 247–252
387 Chen G, Zhang Y, Peng Z, Huang D, Li C, Wang Q. *Nano Res*, 2019, 12: 1321–1326
388 Ast J, Arvaniti A, Fine NHF, Nasteska D, Ashford FB, Stamataki Z, Koszegi Z, Bacon A, Jones BJ, Lucey MA, Sasaki S, Brierley DI, Hastoy B, Tomas A, D'Agostino G, Reimann F, Lynn FC, Reissaus CA, Linnemann AK, D'Este E, Calebiro D, Trapp S, Johnsson K, Podewin T, Broichhagen J, Hodson DJ. *Nat Commun*, 2020, 11: 467
389 Campbell BC, Nabel EM, Murdock MH, Lao-Peregrin C, Tsoulfas P, Blackmore MG, Lee FS, Liston C, Morishita H, Petsko GA. *Proc Natl Acad Sci USA*, 2020, 117: 30710–30721
390 Qian Y, Piatkevich KD, Mc Larney B, Abdelfattah AS, Mehta S, Murdock MH, Gottschalk S, Molina RS, Zhang W, Chen Y, Wu J, Drobizhev M, Hughes TE, Zhang J, Schreiter ER, Shoham S, Razansky D, Boyden ES, Campbell RE. *Nat Methods*, 2019, 16: 171–174
391 Akemann W, Mutoh H, Perron A, Rossier J, Knöpfel T. *Nat Methods*, 2010, 7: 643–649
392 Jin L, Han Z, Platisa J, Wooltorton JRA, Cohen LB, Pieribone VA. *Neuron*, 2012, 75: 779–785
393 Liang T, Wang Q, Li Z, Wang P, Wu J, Zuo M, Liu Z. *Adv Funct Mater*, 2020, 30: 1910765
394 Zhong Y, Ma Z, Zhu S, Yue J, Zhang M, Antaris AL, Yuan J, Cui R, Wan H, Zhou Y, Wang W, Huang NF, Luo J, Hu Z, Dai H. *Nat Commun*, 2017, 8: 737
395 Wang T, Wang S, Liu Z, He Z, Yu P, Zhao M, Zhang H, Lu L, Wang Z, Wang Z, Zhang W, Fan Y, Sun C, Zhao D, Liu W, Bünzli JCG, Zhang F. *Nat Mater*, 2021, 20: 1571–1578
396 Liu MH, Zhang Z, Yang YC, Chan YH. *Angew Chem Int Ed*, 2021,

60: 983–989
397 Qi J, Alifu N, Zebibula A, Wei P, Lam JWY, Peng HQ, Kwok RTK, Qian J, Tang BZ. *Nano Today*, 2020, 34: 100893
398 Scott BB, Thiberge SY, Guo C, Tervo DGR, Brody CD, Karpova AY, Tank DW. *Neuron*, 2018, 100: 1045–1058.e5
399 Yu W, Guo B, Zhang H, Zhou J, Yu X, Zhu L, Xue D, Liu W, Sun X, Qian J. *Sci Bull*, 2019, 64: 410–416
400 Yu X, Feng Z, Cai Z, Jiang M, Xue D, Zhu L, Zhang Y, Liu J, Que B, Yang W, Xi W, Zhang D, Qian J, Li G. *J Mater Chem B*, 2019, 7: 6623–6629
401 Sych Y, Chernysheva M, Sumanovski LT, Helmchen F. *Nat Methods*, 2019, 16: 553–560
402 Takezaki M, Kawakami R, Onishi S, Suzuki Y, Kawamata J, Imamura T, Hadano S, Watanabe S, Niko Y. *Adv Funct Mater*, 2021, 31: 2010698
403 Pisano F, Pisanello M, Lee SJ, Lee J, Maglie E, Balena A, Sileo L, Spagnolo B, Bianco M, Hyun M, De Vittorio M, Sabatini BL, Pisanello F. *Nat Methods*, 2019, 16: 1185–1192
404 Nguyen T, Kim M, Gwak J, Lee JJ, Choi KY, Lee KH, Kim JG. *J Biophotonics*, 2019, 12: e201800298
405 Husain SF, Yu R, Tang TB, Tam WW, Tran B, Quek TT, Hwang SH, Chang CW, Ho CS, Ho RC. *Sci Rep*, 2020, 10: 1–9
406 Feng E, Zheng T, He X, Chen J, Tian Y. *Sci Adv*, 2018, 4: eaau3494
407 Zhou Y, Gu Q, Qiu T, He X, Chen J, Qi R, Huang R, Zheng T, Tian Y. *Angew Chem Int Ed*, 2021, 60: 26260–26267
408 Feng E, Tian Y. *Chem Res Chin Univ*, 2021, 37: 989–1007